Genome scale CRISPR screens identify actin capping proteins as key modulators of therapeutic responses to radiation and immunotherapy

Nipun Verma [1-3],
Paul A. Renauer [1-2], Chuanpeng Dong [1-2], Shan Xin [1-2], Qianqian Lin [1-2], Feifei Zhang [1-2],
Peter M. Glazer [3,6], and Sidi Chen [1-2, 4-8,#]

Affiliations

1. Department of Genetics, Yale University School of Medicine, New Haven, Connecticut, USA
2. System Biology Institute, Yale University, West Haven, Connecticut, USA
3. Department of Therapeutic Radiology, Yale University, New Haven, Connecticut, USA
4. Immunobiology Program, Yale University, New Haven, Connecticut, USA
5. Molecular Cell Biology, Genetics, and Development Program, Yale University, New Haven, Connecticut, USA
6. Yale Comprehensive Cancer Center, Yale University School of Medicine, New Haven, Connecticut, USA
7. Yale Stem Cell Center, Yale University School of Medicine, New Haven, Connecticut, USA
8. Yale Center for Biomedical Data Science, Yale University School of Medicine, New Haven, Connecticut, USA

Correspondence:

SC (sidi.chen@yale.edu)
+1-203-737-3825 (office)
+1-203-737-4952 (lab)

Abstract

Radiotherapy (RT), is a fundamental treatment for malignant tumors and is used in over half of cancer patients. As radiation can promote anti-tumor immune effects, a promising therapeutic strategy is to combine radiation with immune checkpoint inhibitors (ICIs). However, the genetic determinants that impact therapeutic response in the context of combination therapy with radiation and ICI have not been systematically investigated. To unbiasedly identify the tumor intrinsic genetic factors governing such responses, we perform a set of genome-scale CRISPR screens in melanoma cells for cancer survival in response to low-dose genotoxic radiation treatment, in the context of CD8 T cell co-culture and with anti-PD1 checkpoint blockade antibody. Two actin capping proteins, *Capza3* and *Capg*, emerge as top hits that upon inactivation promote the survival of melanoma cells in such settings. *Capza3* and *Capg* knockouts (KOs) in mouse and human cancer cells display persistent DNA damage due to impaired homology directed repair (HDR); along with increased radiation, chemotherapy, and DNA repair inhibitor sensitivity. However, when cancer cells with these genes inactivated were exposed to sublethal radiation, inactivation of such actin capping protein promotes activation of the STING pathway, induction of inhibitory *CEACAM1* ligand expression and resistance to CD8 T cell killing. Patient cancer genomics analysis reveals an increased mutational burden in patients with inactivating mutations in *CAPG* and/or *CAPZA3*, at levels comparable to other HDR associated genes. There is also a positive correlation between *CAPG* expression and activation of immune related pathways and CD8 T cell tumor infiltration. Our results unveil the critical roles of actin binding proteins for efficient HDR within cancer cells and demonstrate a previously unrecognized regulatory mechanism of therapeutic response to radiation and immunotherapy.

Introduction

Radiotherapy (RT), is a fundamental treatment for malignant tumors and is used for curative and palliative purposes in over half of cancer patients [1,2]. The primary mechanism of action for radiation is the production of DNA double strand breaks (DSBs). As a response to DSBs, a robust DNA damage response is elicited that coordinates DNA damage detection and DNA repair, which is primarily through non-homologous end-joining (NHEJ) or homology-directed repair (HDR)[3-5]. The dramatic increase in DSBs within cancer cells following genotoxic therapy like radiation can overwhelm this repair machinery and induce cell cycle arrest and cell death[6].

Over the past decade immune checkpoint inhibitors (ICI) have shown remarkable efficacy against a variety of cancers; however, many patients are unresponsive, fail to achieve a complete response or suffer frequent relapses[7,8]. One promising strategy to increase the efficacy of ICI is to combine them with conventional therapies such as radiation. Prior studies have shown that radiation can trigger the immunogenic cell death of cancer cells and lead to the release of tumor-associated antigens[9,10], remodeling of the tumor microenvironment and activation of local immune cells[11-14], and the triggering of a systemic anti-tumor response[15-18]. Although these studies suggest a possible synergism between radiation and ICI the global landscape of genetic determinants underlying the responses to the combination of radiation and immunotherapy has not been systematically explored before.

Here, we conducted a set of genome-scale CRISPR screens in the context of radiation plus immunotherapy. Our screen in B16F10 mouse melanoma cells identified actin capping proteins, *Capza3* and *Capg*, as important regulators that modulate cancer cell survival in the setting of low-dose genotoxic radiation, CD8 T cell co-culture and anti-PD1 antibody. We also unexpectedly found that inactivation of CAPZA3 and CAPG proteins led to increased DNA damage after radiation treatment due to impaired HDR. Further investigation revealed the link between these actin capping proteins to the induction of the STING pathway and expression of T-cell inhibitory ligands and illustrated how HDR deficiency and chronic STING activation promote immune escape.

Results

Genome-scale CRISPR screen identified genetic regulators of cancer cell survival following radiation in combination with CD8 T cell co-culture and anti-PD1 antibody.

To systematically identify genes that regulate cancer cell response to radiation in combination with immunotherapy, we set out to perform a set of genome-scale CRISPR screens (**Figure 1a**). We used the classical B16F10 mouse melanoma cells and transduced these cells with lentiviral vectors to constitutively express Cas9 and a model antigen ovalbumin (OVA) (**Figure S1a**). We then created a pool of mutagenized B16F10-OVA-Cas9 cells (or B16F10 cells for short, hereafter) with a genome-scale guide RNA (gRNA) lentiviral library (Brie) [19]. We use CD8 T-cells isolated from OT-I mice, which contain an engineered T-cell receptor (TCR) that recognizes the OVA antigen. To identify factors that influence CD8 T cell killing of B16F10 cells following radiation and/or anti-PD1 antibody treatment, we performed co-culture of the Cas9/Brie mutagenized B16F10 cell pools with CD8 OT-I T-cells with or without anti-PD1 antibody treatment. After 3 days in culture, the OT-I CD8 T cells showed expression of activation and exhaustion markers (**Figure S1b**).

Prior to performing the screen, we tested the editing efficiency and effect of gene knockout (KO) on survival of these B16F10-Cas9-OVA cells by targeting the *Pdl1* locus (encoding the mouse PD-L1) (**Figure S1c**). Notably the B16F10 cells transduced with gRNA that targeted *Pdl1* (*Pdl1* KO) showed increased apoptosis following co-culture with OT-I CD8 T cells. Upon mixing *Pdl1* KO and *Pdl1* WT cells at a 1:1 ratio, we found that following co-culture and Annexin V purification, *Pdl1* WT cells were enriched among Annexin V negative cells and *Pdl1* KO cells were enriched among the Annexin V positive cells, suggesting that *Pdl1* KO influenced the differential survival of B16F10 cells co-culture with OT-I CD8 T cells (**Figure S1d-g**).

We set up four treatment conditions in this set of screens: (1) no treatment, (2) low dose radiation (1 Gray (Gy)) prior to co-culture, (3) anti-PD1 antibody during co-culture, and (4) the combination of low dose radiation (1 Gy) prior to co-culture and anti-PD1 antibody during co-culture (**Figure S3a**). We then collected surviving B16F10 mutant cell populations following 1 day of co-culture along with the baseline control of B16F10 cells following Brie library transduction but prior to any treatment (radiation, co-culture, or anti-PD1). We used Annexin V column purification for enrichment of non-apoptotic cells (negative selection) (**Figure 1a**). After Annexin V column purification of our screen samples we verified that Annexin V was depleted in the negative fraction and enriched in the positive fraction (**Figure S2a-b**). To read-out the sgRNA library representation of the samples in this set of screens, we then performed genomic DNA isolation of the isolated surviving cells, followed by library preparation (**Figure S3b**), and

next-generation sequencing (NGS) of the gRNA cassette.

Screen data processing and quality metrics showed robust data quality (**Dataset S1**): (1) the screen replicates clustered with each other and away from the baseline controls (**Figure S3c**); (2) full coverage (near 100%) of the library was detected in all samples (**Figure S3d**); and (3) principal component analysis (PCA) showed the divergence of RT, PD-1, and combination treatment groups from the control groups in the PCA map (**Figure S3e**). We then performed gRNA enrichment and depletion analyses for each treatment condition using a generalized linear model based statistical analysis (SAMBA), as well as a classical MAGECK analysis (**Methods**) [20]. SAMBA analysis identified a set of enriched gRNAs and genes under each condition, including 35, 27, and 28 genes in RT, PD-1, and RT+PD1 treated cells, respectively. (**Dataset S1**). The screen analysis revealed that *Capz3* was the top most enriched gene in the RT screen group; followed by *Brd7,* a gene encoding a key component of the SWI-SNF complex and an epigenetic regulator (**Figure 1b**) [21,22]. Interestingly, *Capza3* was also an enriched gene in the RT plus PD1 screen condition (**Figure 1c**. Other interesting genes enriched in RT+PD1 included *Dipk2a* (encoding Divergent Protein Kinase Domain 2A), *March4* (encoding a member of the MARCH family of membrane-bound E3 ubiquitin ligases), and *Lag3* (encoding a canonical immune checkpoint protein) (**Figure 1c)**. The PD1 screen condition's top enriched gene was *Lpar3* (encoding Lysophosphatidic Acid Receptor 3, a G protein-coupled receptor family member). (**Figure 1d)**. Analysis using an independent MAGeCK analysis algorithm also confirmed that *Capza3* was the top enriched gene in both RT alone as well as RT plus PD-1 screen conditions (**Figure S3f; Dataset S1**).

The actin capping proteins encoding genes *Capza3* and *Capg* were significantly enriched in the RT or RT+PD-1 condition, but not in the PD1 alone condition (**Figure 1c**), hinting that these two targets may modulate the effect of radiation response in B16F10 cells (expressing OVA) in co-culture with cognate T cells (OT-I), with or without PD1. We decided to further investigate *Capza3* with individual gene studies. We used 2 independent *Capza3* gRNAs enriched in the screen to perform individual gene KO by lentiviral transduction into B16F10 cells and found that both can result in high efficiency editing of the *Capza3* gene (**Figure S3g**), and cause reduction of *Capza3* mRNA level (**Figure S3h**). To test the effect on cell survival we generated *Capza3* KO cells by transducing the B16F10 cells with lentivirus that encodes either *Capza3* gRNA 2 or *Capza3* gRNA 3, as well as a GFP marker. We then mixed WT (not transduced by lentivirus) and Capza3 KO cells in a 1:1 ratio and either immediately placed them into co-culture with CD8 OT-I T cells, or exposed to them RT first followed by CD8 T cell co-culture with PD1 antibody

treatment. We observed that there was significant survival benefit of *Capza3* KO cells as compared to WT cells only in the condition of RT + PD1 (**Figure 1e**).

B16F10 *Capza3* KO cells show increased DNA damage due to impaired homology-directed repair

As the *Capza3* gRNA was only enriched in treatment conditions that included radiation (RT, or RT + PD1), we decided to investigate further whether inactivation of *Capza3* impacted DNA damage repair. We confirmed that *Capza3* KO B16F10 cells transduced with either *Capza3* gRNA 2 or gRNA 3 had similar expression and presentation of the OVA antigen and the PDL1 ligand as WT cells transduced with a non-targeting gRNA (**Figure S4a**). We also analyzed the sequences present (modified and unmodified) at the targeting loci of gRNA 2 and gRNA 3 in WT and *Capza3* KO cells (**Figure S4b-d**). Interestingly, although they were enriched in the surviving tumor cells following co-culture, we found that *Capza3* KO B16F10 cells showed persistence of DNA damage markers (53BP1, γH2AX and pRPA) following radiation treatment compared to WT cells (**Figure 2a-d**, **Figure S5a-c**) [23-25]. This effect was most pronounced at low dose radiation (1 Gy) but was also present at higher radiation doses (**Figure 2d**, **Figure S5c**). In line with this persistent DNA damage, *Capza3* KO cells showed reduced colony forming ability (CFA) and increased apoptosis following radiation treatment (**Figure 2e-f**, **Figure S5d**).

Capza3 KO cells also showed increased DNA damage and reduced CFA following treatment with DNA repair inhibitors Olaparib (a poly-ADP-ribose polymerase (Parp) inhibitor) and AZD7648 (a DNA-dependent protein kinase inhibitor) (**Figure 2g**, **Figure S5e-f**). Notably, there were no significant differences in the cell cycle composition between B16F10 WT and *Capza3* KO cells (**Figure 2h**). To investigate the mechanism of this reduced DNA repair ability, we used HDR and NHEJ extrachromosomal luciferase reporters [26] (**Figure 3a**) and found that *Capza3* KO cells showed reduced HDR rates (**Figure 3b**). We used laser micro-irradiation to observe the movement of DNA damage γH2AX foci following subnuclear-targeted radiation (**Figure 3c**) and observed that *Capza3* KO cells showed reduced movement of yH2AX foci away from the area of targeted radiation than WT cells (**Figure 3d-f**, **Figure S6a-b**). To test whether this persistent DNA damage could promote micronuclei formation, we used both Hoechst staining as well as an H2B fluorescent reporter to monitor micronuclei formation (cells that showed at least one micronuclei with both Hoechst and H2B mCherry were identified as positive cells). 24 hour live cell imaging of WT and *Capza*3 KO cells showed a trend towards increased micronuclei formation (although not statistically significant) in the KO cells following radiation treatment (**Figure 3g**).

CAPZA3 and _CAPG_ KO show increased DNA damage following radiation treatment due to impaired HDR in independent human cancer cell lines.

To determine if the KO effect also holds in human cancer, we utilized human breast (MDA-MB-231), pancreatic (PANC1) and skin (SK-MEL-28) cancer cell lines. For the human cell experiments we targeted both *CAPZA3* and *CAPG*. Consistent with the results in B16F10 cells, both MDA-MB-231 and PANCI *CAPG* and *CAPZA3* KO mutants showed increased DNA damage following radiation treatment (**Figure 4a-c**) and reduced HDR repair rates using the extrachromosomal HDR and NHEJ luciferase reporters (**Figure 4d**). For the SK-MEL-28 line the *CAPG* KO line had increased DNA damage and reduced HDR, but the 2 *CAPZA3* KO lines did not except at a high radiation dose of 10 Gy (**Figure S7a**). None of the MDA-MB-231, PANC1 and SK-MEL-28 *CAPG* or *CAPZA3* KO lines showed a significant difference in NHEJ compared to WT cells (**Figure S7b-c**). To investigate why SK-MEL-28 *CAPZA3* KOs did not show the same phenotype as PANC1 and MDA-MB-231 KOs we looked at the expression of *CAPZA3* within these cell lines. Like PANC1 and MDA-MB-231, *CAPZA3* is expressed in SK-MEL-28 cells (**Figure S7d**); however, SK-MEL-28 *CAPZA3* KO lines showed greater CAPZA3 expression than MDA-MB-231 and PANCI *CAPZA3* KO lines, suggesting that the SK-MEL-28 lines may not be complete functional KOs (**Figure S7e**).

Consequently, we decided to focus on the MDA-MB-231 and PANC1 lines for future experiments. The MDA-MB-231 and PANC1 KO cells, both *CAPZA3* and *CAPG,* showed reduced CFA after radiation treatment (**Figure 4e**); and the PANC1 KO cell lines showed reduced CFA with cisplatin treatment (**Figure 4f**). Although there appeared to be a trend for reduced CFA for PANC1 KO lines after treatment with Olaparib, the comparisons between KO and WT were not significant (**Figure S7f**). To further verify the HDR defect seen in these KO cells, we generated a PANC1 intra-chromosomal HDR and NHEJ reporter line by integrating the DNA repair traffic light reporter (TLR) construct [27] into the *AAVS1* locus (PANC1-TLR). This TLR reporter includes a *Rosa26* gRNA sequence within the sequence that is inserted into the *AAVS1* locus and when a plasmid containing a *Rosa26* gRNA is transfected into these cells it generates a cut at this site; If this cut is repaired by HDR then GFP is expressed; in contrast if it is repaired by NHEJ then RFP is expressed. Using this line, we once again generated *CAPG* and *CAPZA3* KO clones. Following transfection with the *Rosa26* targeting gRNA we found that *CAPG* and *CAPZA3* KO lines showed lower HDR rates compared to WT cells (**Figure 4g-h**, **Figure S8d**).

CAPZA3/Capz3 and _CAPG_ KO cells show increased activation of the _STING_ pathway and increased expression of _CEACAM1_.

Our data above showed that inactivation of *CAPG* and *CAPZA3* leads to reduced HDR efficiency and persistent DNA damage following radiation treatment. However, it was still to this point unclear how this DNA repair defect could lead to increased resistance to CD8 T cell killing. To further investigate this, we performed transcriptome profiling using RNA-seq in WT and *Capza3* KO B16F10 cells, with 2 independent clones from each genotype/group (WT, *Capza3* KO gRNA 2, and *Capza3* KO gRNA 3), with biological duplicates for each clone (2 x 2 = 4, quadruplicates for each genotype) (**Methods**). The cells were analyzed before and after radiation treatment (**Methods**). We thus produced an RNA-seq dataset of 24 samples with robust quality metrics (**Figure S9a-b; Dataset S2**). We verified that replicates of the same genotype showed higher correlation as compared to between genotypes/groups, and clustered together on PCA (**Figure S9a-b**).

Differential expression (DE) analysis of RNA-seq data (**Methods**) revealed transcriptomic differences between WT and *Capza3* KO cells, and between RT and control samples (**Figure 5a-b**). Genes encoding transcription factors associated with the *Sting* pathway (*Irf1, Irf3, Irf9,* and *Stat2*) showed increased activity in *Capza3* KOs compared to WT cells both before and after radiation treatment (**Figure 5c-d**, **Figure S9c**). We also saw increased *STING* and *IRF3* expression in MDA-MB-231 and PANC1 KO cells at the protein level using western plot (**Figure 5e, Figure S9d**). Analysis of the IRF1 targets showing greatest change in expression between WT and *Capza3* KOs revealed increased expression of *Ceacam1*, a CD8 T cell inhibitor ligand, in *Capza3* KO cells. We also confirmed the increased *Ceacam1*/*CEACAM1* gene expression at mRNA level using qPCR (in B16F10, MDA-MB-231 and PANC1 lines) (**Figure 5f**), and CEACAM1 at the protein level using flow cytometry (in PANC1 cell line) (**Figure 5g**).

CEACAM1 inactivation or anti-TIM3 antibody blockade reversed the phenotype of survival benefit of _CAPG_/_CAPZA3_ KO human cancer cells with radiation in co-culture with EGFR CAR-T.

To investigate whether increased expression of *CEACAM1* directly contributes to the survival advantage of *CAPZA3*/*CAPG* KO human cancer cells, we performed co-culture experiments using the MDA-MB-231 and PANC1 lines (both of which express EGFR) and EGFR targeting CAR-T (**Methods**). We observed a survival advantage for MDA-MB-231 and PANC1 *CAPZA3*/*CAPG* KO lines compared to WT cells following co-culture with EGFR CAR-T (**Figure 6a-c**). Notably the survival advantage of PANC1 *CAPZA3*/*CAPG* KO cells was only detected at low dose radiation (1 Gy) or no radiation treatment prior

to co-culture (**Figure 6d**). At higher radiation doses there was no observed survival advantage, perhaps due to greater sensitivity of the KOs to DNA damage. CEACAM1 on cancer cells can bind to both CEACAM1 and TIM3 on CD8 T cells and the EGFR CAR-T express both CEACAM1 (**Figure 6e**) and TIM3, but not PD1 or LAG3 (**Figure 6f**) during maintenance culture. We found that the survival advantage of *CAPZA3*/*CAPG* KO PANC1 lines was lost if anti-TIM3 antibody was added during co-culture (**Figure 6g**). Knocking out *CEACAM1* in *CAPZA3*/*CAPG* KO PANC1 lines also negated their survival advantage following co-culture with EGFR CAR-T (**Figure 6h**), suggesting that CEACAM1 is a direct mediator of such effects. Analysis of activation and exhaustion markers of EGFR CAR-T cells following co-culture with *CEACAM1*, *CAPG* or *CAPZA3* single and double KO lines showed minor differences (**Figure S11a-e**). Given these findings, we investigated whether combining radiation treatment with anti-TIM3 antibody may lead to enhanced killing of *CAPZA3*/*CAPG* KO cells compared to radiation with anti-PD-1 Ab. We did observe that both PANC1 and MDA-MB-231 *CAPG*/*CAPZA*3 KO lines showed increased expression of PDL1 following 1 Gy radiation treatment compared to WT cells (**Figure 6i**, **Figure S12a**). Importantly, both anti-TIM3 and anti-PD1 antibody blockade reduced survival significantly for *CAPZA3* and *CAPG* KOs compared to the no treatment and radiation treatment alone conditions (**Figure 6i**, **Figure S12b**).

Discussion

Through genome-scale CRISPR screens we discovered two actin capping proteins *Capza3*/*CAPZA3* and *CAPG* in cancer cells that mediate differential responses to RT and/or immunotherapy. Validation studies showed that inactivation of these genes induces an HDR defect that leads to persistence of DNA damage and promotes chronic STING activation and the expression of an immune inhibitory ligand, *CEACAM1*. The HDR defect was confirmed using DNA damage foci immunofluorescence, radiation and genotoxic chemotherapy sensitivity, DNA repair inhibitor sensitivity, extrachromosomal DNA repair reporters as well as the Traffic Light Reporter[27] stably integrated into the *AAVS1* safe harbor locus of PANC1 cells.

To evaluate the human cancer relevance of such findings, we analyzed the TCGA dataset for *CAPG* and *CAPZA3* associated prognostic signatures of clinical outcome. Interestingly, we found that in-activating mutations for *CAPZA3* or *CAPG* frequently co-occur with mutations for other HDR associated genes (**Figure 7a**). Although we may expect that mutations of genes that function in the same pathway would be mutually exclusive, prior studies have shown that mutations in DNA repair genes frequently co-occur in numerous cancer types [28]. Since there was co-occurrence of mutations in *CAPZA3*, *CAPG* and genes

known to be associated with HDR, for the rest of our analyses we excluded any TCGA data samples that had a mutation in more than one HDR associated gene. Importantly the expression patterns for *CAPG* and *CAPZA3* differ significantly: *CAPG* is expressed widely in somatic tissues and shows increased expression in tumor samples. In contrast, *CAPZA3* is normally only expressed within the testis, but shows sporadic expression in several cancers (**Figure 7b, Figure S13a**). Despite these differences in expression, inactivating mutations in both *CAPG* and *CAPZA3* led to increased tumor mutational burden and mutation counts, which was comparable to other HDR associated genes, and significantly increased compared to the unaltered control group of patients in a pan-cancer analysis (**Figure 7c, Figure S13b**). *CAPG* expression also showed a significant correlation with CD8 T cell infiltration and increased activation of immune related pathways (**Figure 7d-e**, **Figure S14a-c**). *CAPZA3* did not show this effect, due to the fact that over 50% of tumor samples in the TCGA dataset had a 0 expression value for *CAPZA3*, which limited the power of this analysis (**Figure 7d-e**, **Figure S14a-c**).

Finally, we observed that for multiple types of cancers there was a significant difference in overall survival (OS) based on the expression of *CAPG*, *CAPZA3* and other HDR associated genes (**Figure 7f-g**). Of the 33 cancer types within the TCGA dataset, 11 showed a significant difference in OS based on *CAPG* or *CAPZA3* expression, as benchmarked with 12 cancer types that showed a significant survival difference based on *BRCA1* or *BRCA2* expression (**Figure S13b, S15**, **S16, Dataset S4**). For most cancers low expression of an HDR associated gene (including *CAPG* and *CAPZA3*) was favorable and was associated with improved OS and the HDR gene had an HR > 1(**Figure S13c-d**). However, in colorectal cancer (COAD), renal clear cell cancer (KIRC), esophageal cancer (ESCA), stomach cancer (STAD), thyroid cancer (THCA) and thymoma (THYM), the HDR gene had a HR < 1 and low expression was unfavorable and associated with poorer survival, as would be predicted by our screen result (**Figure S13d**). This divergence in patient survival outcomes may reflect the contrasting effects that reduced HDR ability has on cancer cell survival. Low expression of an HDR associated gene may render cancer cells more vulnerable to standard genotoxic therapies such as radiation and chemotherapy; however, it may also enhance cancer cell survival by promoting immunosuppression (**Figure 7h**). Notably ICI use has been approved for COAD, KIRC, ESCA and STAD cancers suggesting that perhaps immunosuppression has greater functional importance for clinical outcomes among patients with these cancers. In this case low expression of the HDR gene is associated with increased immunosuppression, which outweighs the genotoxic vulnerability, and thus is associated with poorer OS. Overall, we found that expression of *CAPG* and *CAPZA3* showed a similar effect on patient OS as other HDR genes; however, the consequence of

HDR inhibition will need to be investigated further and will likely differ between cancer types based on tumor specific sensitivity to DNA damage and the mechanisms for immunosuppression.

Our study identified a previously un-appreciated role of actin capping proteins for efficient HDR in cancer cells. Prior studies have found that DSBs undergoing HDR are very dynamic, clustering into subnuclear compartments that facilitate homology detection and increase HDR efficiency [29-36]. Formation of these functional domains is believed to involve actin mediated mechanical forces, as nuclear actin forms polymers following exposure to genotoxic agents [37] and the expression of a polymerization deficient NLS-R62D actin has been found to reduce HDR rates [30]. Furthermore, the proteins necessary for actin remodeling in the cytoplasm, Wiskott-Aldrich Syndrome protein (WASP), Arp2/3, formin and actin capping proteins, have also been found within the nucleus [38,39] and the reorganization of heterochromatin breaks and efficient HDR is promoted by the formation of actin filaments through Arp2/3 dependent [34] and formin dependent mechanisms [30,37,40]. Actin (β-actin) and actin binding proteins (CAPZβ, APRC4) have also been found to bind to damaged chromatin, and chromatin immunoprecipitation experiments of a specific endonuclease-generated DSB site recovered WASP and ARP2 [35], suggesting the interaction of actin-regulating proteins with damaged DNA, either by direct binding or indirectly through other repair factors. Actin and actin binding proteins are not frequently mutated in cancer cells; however, the deregulation of WASP protein, an Arp2/3 activator, leads to HDR deficiency in lymphocytes [34] as well as an increased risk for the development of non-Hodgkin's lymphoma and leukemia [41]. A recent study also found that RHOJ regulation of formin-dependent nuclear actin polymerization enhanced DNA repair in cancer cells undergoing EMT and promoted their chemoresistance [42]. These studies, as well as our results here, suggest that profiling and targeting of actin regulating proteins may provide clinically relevant information on HDR deficiency and offer therapeutic insights on the resistance to genotoxic treatments such as chemotherapy and radiation.

An interesting finding of our study was the implication that DNA damage associated with HDR deficiency may have unique immunosuppressive downstream effects. It has consistently been shown that tumors with mutations or epigenetic silencing of genes involved in mismatch repair (dMMR) are vulnerable to ICI [43-45]. However, ICI use for HDR deficient breast and ovarian tumors has not shown a similar clinical benefit [46-49]. A possible explanation is that HDR deficiencies may lead to unique immune-suppressive consequences that might impact ICI effectiveness. Activation of cGAS-STING pathway has been previously described in DNA repair deficient cancers following genotoxic stress and shown to induce

expression of *PDL1*, a T cell inhibitory ligand [50-54]. Notably in our CRISPR screen we found that *Capza3* and *Capg* targeting gRNAs were enriched in the Radiation and anti-PD1 antibody condition, suggesting a survival mechanism independent of *PDL1*. Our RNA-Seq analysis identified that *CEACAM1* is induced in *Capza3* KO cells. Moreover, our *Capza3*/*CAPZA3* and *CAPG* KOs showed greater induction of *CEACAM1* expression following low dose radiation treatment. CEACAM1 is an inhibitory ligand expressed on cancer cells that can impair T cell function through either homophilic interactions or interactions with TIM3 [55-58]. In addition to PDL1, our study suggests that CEACAM1 may also be a promising immunotherapeutic target, particularly for HDR deficient cancers, and may lead to more efficacious combination with radiation treatment than has been seen in prior immunotherapy and radiation trials [59-62].

Acknowledgments

We thank the Glazer lab members for reagent sharing and technical assistance. We thank all members of the Chen laboratory, as well as various colleagues at Yale for assistance and/or discussion. We thank the Yale Center for Genome Analysis, High Performance Computing Center, Yale Center for Molecular Discovery, Microscopy Core, and Keck Biotechnology Resource Laboratory at Yale, for technical support.

SC is supported by Cancer Research Institute Lloyd J. Old STAR Award (CRI4964), NIH/NCI (DP2CA238295, R01CA231112, R33CA281702), DoD (W81XWH-20-1-0072, W81XWH-21-1-0514, HT94252310472), Alliance for Cancer Gene Therapy (ACGT), Pershing Square Sohn Cancer Research Alliance, and YCC Team Science Award. PG is supported by NIH grants (R35CA197574 and R01ES005775). NV is supported by American Board of Radiology's B. Leonard Holman Research Pathway Fellowship. PR is supported by Yale PhD training grant from NIH (T32GM007499), Lo Fellowship of Excellence of Stem Cell Research, and YCC T32 fellowship program. CPD is supported by Boehringer Ingelheim Biomedical Data Science Fellowship.

Methods

Institutional approval

This study has received institutional regulatory approval. All recombinant DNA and biosafety work were performed under the guidelines of Yale Environment, Health and Safety (EHS) Committee with an approved protocol (Chen-rDNA 15-45; 18-45; 21-45). All animal work was performed under the guidelines of Yale University Institutional Animal Care and Use Committee (IACUC) with approved protocols (Chen 2018-20068; 2021-20068). All human sample work was performed under the guidelines of Yale University Institutional Review Board (IRB) with an approved protocol (HIC#2000020784).

Mouse CD8 T cell culture

Spleens were isolated from OT-I mouse strain and placed in ice-cold wash buffer (2% FBS in PBS). Spleens were dissociated mechanically, passed through a 100 µm filter, and incubated with ACK Lysis Buffer (Lonza) for 2 minutes at room temperature to lyse RBCs. The resulting cell suspension was washed with wash buffer, filtered through a 40 µm filter and then resuspended in MACS Buffer (0.5% BSA and 2 µM EDTA in PBS). Naive $CD8^+$ T cells were isolated using naïve mouse CD8 T cell isolation kit from Miltenyi (130-104-075). Naive $CD8^+$ T cells were counted and then resuspended in cRPMI (RPMI-1640 with 10% FBS, 2mM L-Glutamine, 1% HEPES, 1% 100 nM NaPyruvate, 1% NEAA, 100U Pen/Strep and .05 µM β-mercaptoethanol) to a final concentration of 1×10^6 cells/ml. The cells were then plated into a 12 well plate at a concentration of 1×10^6 cells per well. These CD8 T cells were expanded *in-vitro* using a previously published protocol [63]. In brief, cells were expanded for 3 days in cRPMI media supplemented with 10 ng/mL OVA (Anaspec AS-60193-1), 5 ng/mL IL7 and 5 ng/mL IL15. Cytokines were purchased from Peprotech. After 3 days of *in-vitro* expansion CD8 T cells were used for co-culture experiments.

Generation of B16F10 cells that express Cas9 and OVA antigen

We generated a B16F10 cell line that expresses Cas9 protein and OVA antigen to be used in our screen. For all experiments B16F10 cells were maintained in complete DMEM media (DMEM with 10% FBS, 2mM L-Glutamine and 100U Pen/Strep). Cells were passaged when they reached confluence, which was typically 2-3 days after splitting depending on the splitting ratio. Cells were passaged using TrypLE and cell lines were frozen using DMSO-containing media.

To generate a Cas9 expressing B16F10 line (B16F10-Cas9) a lentiviral Cas9-Blast vector (Addgene Plasmid # 52962) was co-transfected with packaging plasmids PAX2 and pMD2.G into HEK293T. Transfection was performed using LipoD293T (Signagen # SL100668) per the manufacturer's protocol. Virus was harvested at 48 hours post-transfection, tittered, and stored at -80°C. B16F10 cells were transduced with Cas9-Blast lentivirus overnight. Two days later, infected cells were selected with 5µg/ml of blasticidin for at least 3 days. Clonal lines of B16F10-Cas9 were established and their cutting efficiency was verified using *Pdl1* targeting gRNA and flow cytometry analysis of PDL1.

Next, to overexpress OVA antigen within the B16F10-Cas9 line, lentivirus that contain an OVA-mCherry vector (Sidi Chen lab) were generated using the procedure described above. The B16F10-Cas9 clonal lines were then transduced with this lentivirus and 2 days after transduction mCherry positive cells were sorted, expanded and frozen down. OVA expression was verified using OVA-MHCII (Biolegend 141605) flow analysis. The B16F10-Cas9-OVA cell line (referred to as B16F10 within the manuscript) was confirmed negative for mycoplasma by quantitative RT-PCR.

Human cell culture

MDA-231 (ATCC HTB-26), PANC1 (ATCC CRL-1469) and SK-MEL-28 (ATCC HTB-72) cell lines were cultured in complete DMEM media (DMEM with 10% FBS, 2mM L-Glutamine, and 100U Pen/Strep). Cells were passaged when they reached confluence, typically 2-3 days after splitting, depending on the splitting ratio. Cells were passaged using TrypLE and cell lines were frozen using DMSO-containing media. All human cell lines were confirmed negative for mycoplasma by quantitative RT-PCR.

Genome scale CRIPSR screen in B16F10 cells

gRNA pool library production: Mouse CRISPR Brie lentiviral pooled library (Addgene Plasmid # 170511) consisting of 79,637 gRNAs was co-transfected with packaging plasmids (psPAX2 and pMD2.G) into HEK293T cells using LipoD 293T transfection reagent (Signagen # SL100668) following the manufacture's protocol. 24 hours after transfection the media was replaced. Virus supernatant was collected at 48 and 72 hours after transfection. Virus was concentrated using PEG virus precipitation (Promega # V3011). In brief, the collected supernatant was pooled and spun down at 3000g for 15 minutes to remove cell debris. Supernatant was carefully collected and 8 mL of 40% PEG8000 solution was added to 32 mL of viral supernatant for a final concentration of 8% PEG8000. After mixing well with vortexing

the virus supernatant was incubated overnight at 4C. The next day the viral supernatant was centrifuged at 3000g for 30 minutes at 4C. The supernatant was aspirated carefully to avoid disturbing the virus pellet which was then resuspended in cRPMI, divided into small aliquots and stored at -80°C. To determine virus titer $1x10^6$ B16F10-Cas9 cells were plated per well of a 6-well plate. B16F10 cells were transduced with different amounts of the aliquoted lentivirus in the presence of 8 µg/ml of polybrene. The next day, transduced B16F10 cells from each condition were seeded at a density of 10,000 to 100,000 cells per well of a 6-well plate (in triplicates). Twenty-four hours following infection, puromycin (2µg/ml) was added. After 3 days of puromycin selection infected cells in each well were counted.

Screen: B16F10-Cas9-OVA cells (hereafter referred to as B16F10) were transduced with the Brie library lentivirus at a MOI of 0.3 and cells were selected with puromycin (2 µg/mL) for 3 days prior to use in co-culture with CD8 T cells. Mouse CD8 T cell isolation was performed as described above. Prior to co-culture approximately 120 million B16F10 cells were isolated as a baseline control. There were four treatment conditions tested in our screen: No treatment, anti-PD1 antibody during co-culture, 1 Gy radiation before co-culture, and 1 Gy radiation before co-culture followed by co-culture with anti-PD1 antibody. To maintain at least a 1000x fold coverage, approximately 100 million B16F10 cells were used for each condition. B16F10 cells were plated into 24 well plates (1 million cells per well) and pretreated with 10 ng/ml of IFN-γ for 24 hours prior to co-culture with OT-I CD8 T cells to increase MHC class II expression. For treatment conditions that included radiation the plated B16F10 cells were exposed to 1 Gy radiation (using MultiRad350 irradiator per the manufacturer's protocol) 1 hour before the addition of OT-I CD8 T cells. For conditions that included anti-PD1 antibody treatment we used anti-mouse PD-1 inVivo mAB # BE0146 (clone: RMPI-14, Lot#806321A2B) at a concentration of 10 µg/mL. With the addition of the CD8 T cells to B16F10 the media was changed to cRPMI with IL7 (5 ng/mL) and IL15 (5 ng/mL). Co-culture was done at a 1:1 T:E ratio. 1 day after co-culture we performed Annexin V bead purification (Miltenyi # 130-090-201) per the manufacturer's protocol. Cells were passed through the column twice to increase purification of Annexin V negative cells. 2 replicates of the screen, starting with lentiviral infection of B16F10 cells with the Brie library, were done.

Library preparation and sequencing: Genomic DNA was isolated from Annexin V negative cells using the DNeasy Blood and Tissue kit (Qiagen # 51192) following the manufacturer's protocol. PCR amplification of the gRNA cassette for Illumina sequencing of gRNA representation was done using the Broad protocol available online (https://media.addgene.org/cms/filer_public/56/71/5671c68a-1463-4ec8-9db5-761fae99265d/broadgpp-pdna-library-amplification.pdf). NGS Illumina sequencing was done by the YCGA core to a depth of 200x.

Screen data analysis: Raw sequencing fastq data had adapter sequences trimmed via Cutadapt v3.41 [64] using a 10% error rate and the following sequences: forward, 5'-tcttgtggaaaggacgaaacaccg; reverse, 5'-gttttagagctagaaatagcaagt. Trimmed sequences were then filtered to remove those with <15 nt length. The remaining sequences were aligned to a reference, comprised of the CRISPR sgRNA-spacer sequences. Alignment was performed using Bowtie v1.3.02 with the following settings: -v0, -m1 –best. The sgRNA counts for each sample were processed and analyzed using SAMBA R package v1.3.0 (https://github.com/Prenauer/SAMBA) (detailed below) [65]. Specifically, sgRNAs were filtered to include those with >10 counts across screened samples (non-control). A two-step data analysis was performed, first with an sgRNA-level analysis by the edgeR R package v3.38.43 pipeline with TMM-wsp size factors, feature-wise dispersion, quasilikelihood (QL) generalized linear model fitting, and QL F tests. In the second analysis step, sgRNA scores were aggregated into a gene score, calculated as a weighted sum of the sgRNA log2 fold-changes (log2-FC). Gene level p values were assessed based on a null distribution of gene scores, which were scored from randomly grouped sgRNAs of non-targeting controls. P values were adjusted using the method by Benjamini and Hochberg. An additional metric to assess gene enrichment was the number of sgRNA / gene with a log2-FC > the 90th percentile of the randomized null data log2-FC, representing a 10% FDR. Screen data was also analyzed with the commonly used MAGeCK RRA algorithm for robust comparison [20].

The screen analyses included all samples in a statistical model that incorporated cocultured B16F10 that were treated with anti-PD-1 and / or radiation therapy (RT) (~ Coculture + anti-PD-1 + RT + anti-PD-1:RT). From this statistical model, we separately assessed the effects of anti-PD-1, RT, and the combined treatment coefficients with SAMBA. We verified that there was high gRNA detection for all treatment conditions in both screen replicates and that the treatment conditions for the two replicates showed high correlation and clustered together on PCA component analysis.

Western blot

PANC1 and MDA-MB-231 cells were lysed for 10 min in 1X RIPA buffer (Cell Signaling Technology, #9806) supplemented with 1X Protease Inhibitor Cocktail (Roche) and then centrifuged for 10 min at 13,200 rpm to remove cell debris.

Equal amounts of proteins were loaded for separation on 12% SDS-PAGE gels (Bio-Rad) and were subsequently transferred to 0.2µm nitrocellulose membranes. After blocking with 2.5% BSA for 1 h at room temperature, the membranes were incubated in specific primary antibodies diluted in 2.5% BSA at 4 °C overnight. The next day, membranes were incubated with secondary antibodies for 2 h at room

temperature. ECL prime western blotting detection reagents (Bio-Rad) were used at a ratio of 1:1 for chemiluminescence detection. Quantification was done using ImageJ.

Primary antibodies used for western blot were: Sting (Cell Signaling # 13647, 1:1000), TBK1 (Cell Signaling # 3504, 1:1000), IRF3 (Cell Signaling # 11904, 1:1000), GAPDH (ThermoFisher # MA1-16757, 1:2000). Secondary antibodies used were: Anti-rabbit IgG (Cell Signaling # 7074, 1:5000), Anti-mouse IgG (Cell Signaling # 7076, 1:5000).

Generation of B16F10 *Capza3* KO cell lines

To generate the B16F10 *Capza3* KO lines the 2 CRISPR gRNAs enriched in the radiation alone and radiation and anti-PD1 antibody screen treatment conditions were cloned into the LRG vector (Addgene Plasmid # 65656). For WT controls a NTC gRNA from the CRISPR screen was cloned into the LRG vector. Lentivirus was made by co-transfecting these vectors with packaging plasmids (PAX2 and pMD2.G) into HEK293T cells using LipoD 293T transfection reagent (Signagen # SL100668) following the manufacturer's protocol. B16F10 cells were transduced with lentivirus using the protocols described above. 2 days after transduction, GFP positive B16F10 cells were sorted into a 96 well plate at a density of 10 cells per well and allowed to expand. Each well thus contained a mixture of clonal lines. To enrich B16F10 cells that had mutations at the *Capza3* loci we sequenced each of the wells to identify those that had depleted WT sequences by sanger sequencing. These wells were expanded and then the cells sorted again (into a 96 well plate at a density of 10 cells per well) with a second round of sequencing to identify wells which had absence or a low proportion of WT cells. Using this process, we generated 2 mixtures of clonal KO cells for *Capza3* gRNA 2 targeting (*Capza3* gRNA 2 #1 and *Capza3* gRNA 2 #2) and 2 mixtures of clonal KO cells using *Capza3* gRNA 3 targeting (*Capza3* gRNA 3 #1 and *Capza3* gRNA 3 #2). To maintain the same passage number, WT cells transduced with LRG containing a NTC gRNA went through the same procedure described above. Nextera library preparation and next generation sequencing was used to quantify the percent modified alleles in both Capza3 gRNA targeting loci in our KO mixtures and in WT cells and are shown in a supplemental figure. Oligonucleotide sequences are listed in Supplementary Tables.

Nextera library preparation and sequencing

The region around both *Capza3* gRNA targeting loci were amplified by PCR and then tagged, amplified, and barcoded using Nextera XT DNA Library Prep Kit (Illumina) per the manufacturer's protocol. The library for each sample was quality controlled and quantified separately using the 4150 TapeStation System (Agilent), followed by library pooling and PCR clean up using QIAquick PCR Purification Kit

(Qiagen). Libraries were denatured and diluted to 10 pM according before loading on MiSeq (Illumina) for next generation sequencing. FASTQ reads were quality controlled by running FastQC v0.11.9 [66] and contaminations by Nextera transposase sequence at 3' end of reads were trimmed using Cutadapt v3.2 [64]. Processed reads were aligned to amplicon sequence and quantified for insertions, deletions (indel), and substitution using CRISPResso2 v2.1.3 [67]. Specifically, we retrieved amplicon sequences, which were 150 ~ 250 bp (according to the length of reads) flanking crRNA target sites, from the mm10 genome. A 5-bp window, centered by predicted Cas9 cutting sites, was used to quantify genetic modification for each crRNA in both WT and *Capza3* KO cells. Percent modification and allele frequency plots were generated with CRISPResso2 v2.1.3.

Immunofluorescence of DNA damage markers and quantification

High-throughput immunofluorescence foci assays were performed at the Yale Center for Molecular Discovery (YCMD). Polystyrene flat bottom 384-well plates (CellVis # P384-1.5H-N) were coated with collagen O/N at 4C (10 ng/mL diluted in PBS). Collagen was aspirated and cells (B16F10, PANC1, MDA-MB-231, SKMEL28) were seeded at 10,000-50,000 cells/well and allowed to adhere overnight. Cells were irradiated (using MultiRad350 per manufacturer's protocol) and then fixed at different time points (1 hour, 3 hours, 6 hours and 24 hours) before staining for DNA damage markers: γH2AX (Cell Signaling Technology # 9718T), 53BP1 ((Novus Biologicals # NB100-904) and phospho-RPA2 (pRPA, Bethyl Laboratories # A300-246A). Cells were fixed with 4% paraformaldehyde in PBS for 15 min, washed twice with PBS, and then incubated in permeabilization buffer (0.3% Triton X-100 in PBS) for 15 min. Cells were washed twice with PBS and then incubated in blocking buffer (2% BSA in PBS) or 1 h. All primary antibodies were incubated O/N at 4°C at the appropriate dilution: γH2AX (1:200), 53BP1 (1:200), pRPA (1:250). After primary antibody staining the cells were washed three times with PBS and then incubated with Alexa Fluor dye conjugated secondary antibody (ThermoFisher # A-11012) and DAPI (Biolegend # 422801) for 1 hr at RT. After secondary antibody staining cells were washed 3 times with PBS and images were taken on either the InCell Analyzer 2200 Imaging System or the Leica SP8 confocal microscope. Quantification of DNA damage foci was performed by YCMD using the Incell Analyzer software.

Additional small-scale immunofluorescence experiments were performed using 8-well chamber slides (Ibidi # NC0704855). These slides were coated with collage O/N at 4C (10 ng/mL diluted in PBS). Collagen was aspirated and cells (B16F10, PANC1, MDA-MB-231, SKMEL28) were seeded at 100K - 200K cells/well and allowed to adhere overnight. Following irradiation (using MultiRad350 per

manufacturer's protocol), cells were fixed and stained for γH2AX, 53BP1, and pRPA as described above. Images were taken using the Leica SP8 confocal microscope at 63X magnification.

Colony forming assay (CFA)

B16F10 cells were plated 1 day before they were irradiated at varying doses of ionizing radiation (using MultiRad350 per manufacturer's protocol). Four to six hours after irradiation, cells were detached using TrypLE, washed with complete DMEM media, counted, and seeded in 6-well plates in triplicate at a density of 100 cells per well. These plates were kept in the incubator for 10 to 14 days. After incubation, colonies were washed in PBS, fixed with ice-cold 100% methanol for 10 minutes at -20C and then stained with crystal violet (0.5% crystal violet in 25% methanol). Colonies were counted using a brightfield microscope. Colonies needed to have at least 10 cells to be counted as a colony. For PANC1 and MDA-MB-231 cells lines irradiation was carried out in the same way as described above. However, to make sure the cell number was accurate we used FACS sorting to sort 50 cells per well into a 24 well dish. Staining with crystal violet and quantification was carried out as described above.

For colony forming assay after drug incubation, cells were cultured for 1 day with different concentrations of the drugs cisplatin (Selleckchem #S1166), AZD7648 (DNA PK inhibitor, Cayman # 28598) and Olaparib (Parp inhibitor, Cayman # 10621-25). 1 day after culture the cells were detached using TrypLE, washed with wash buffer (2% FBS in PBS) and then FACS sorted 50 cells per well into a 24 well dish. Staining with crystal violet and quantification was carried out as above.

Cell cycle analysis

Cell cycle analysis was performed using DAPI nucleic acid dye (Biolegend #422801). 1 day after passaging, B16F10 cells were detached using TrypLE, washed with wash buffer (2% FBS in PBS) and collected. The cells were counted and the concentration for each sample was adjusted to 1 x 10^6 cells/mL. Ice-cold 70% EtOH was added dropwise to the cell pellet while mixing gently with a vortexer. Cells were stored on ice for 2 hours. Cells were then washed 3x with wash buffer. 1 mL of DAPI working solution was added to the cells (15 ul of 1mg/ml DAPI was added to 15 mL of 0.1% Triton-X in PBS) and cells were incubated in the dark for 15-30 min at RT before FACS analysis.

Extra-chromosomal luciferase reporter assays

The NHEJ and HDR luciferase reporters has been previously reported [26] and were obtained from the Peter Glazer lab. For the HDR luciferase reporter, a DSB in the firefly luciferase gene was induced by I-SceI digestion and confirmed by electrophoresis. Linearized plasmid was then transfected into cells. HDR within the cells will restore the luciferase activity, which can then be used to measure HDR efficiency. To assay NHEJ, a HindIII-mediated DSB was generated within the NHEJ luciferase reporter and confirmed by electrophoresis. After transfection of the linearized NHEJ plasmid, repair of the DSB by NHEJ restores firefly luciferase activity.

All reporter assays were performed in a 96-well format by seeding 50,000- 100,000 cells per well, 24 hours before transfection. Lipofectamine 3000 (ThermoFisher # L3000008) was used for transfection per the manufacturer's protocol. As a control for transfection rates a plasmid with an intact luciferase was used for each cell line in a separate well. Luciferase following transfection with linearized HDR and NHEJ reporters was then normalized to this control for each sample. Luciferase activity was read using a bioluminescence plate reader.

Laser Micro-irradiation

Laser micro-irradiation experiments were done using 8-well chamber slides (Ibidi # NC0704855). These slides were coated with collage O/N at 4C (10 ng/mL diluted in PBS). Collagen was aspirated and B16F10 were seeded at 100K -200K cells/well and allowed to adhere overnight. Cells were mounted on a Leica TCS SP8 X microscope system (Leica Microsystems) with an incubator chamber at 37°C with 5% CO_2. For laser micro-irradiation cells were exposed to a 405 nm diode laser (95% with FRAP booster, 35 iterations, 150 µJ/pixel total power) and irradiation field of multiple 5-pixel wide stripes. At different time points after irradiation (1 minute, 5 minutes, 10 minutes, 15 minutes, and 20 minutes), cells were fixed with 4% PFA in PBS for 10 min at RT. γH2AX staining was done as described above. For analysis of micro-irradiation stripe intensity ImageJ was used.

Generation of B16F10 H2B mCherry cell lines and live cell imaging

To generate B16F10 cells with a H2B-mCherry reporter the H2B mCherry reporter plasmid (Addgene Plasmid # 20972) was co-transfected with packaging plasmids PAX2 and pMD2.G into HEK293T. Transfection was performed using LipoD293T per the manufacturer's protocol. Virus was harvested at 48 hours post-transfection and stored at -80°C. WT and *Capza3* KO B16F10 cells were transduced with lentivirus and two days later mCherry positive cells were sorted and expanded.

Live cell imaging was performed using 8-well chamber slides (Ibidi # NC0704855). These slides were coated with collagen O/N at 4C (10 ng/mL diluted in PBS). Collagen was aspirated and B16F10 were seeded at 100K -200K cells/well and allowed to adhere overnight. Cells were mounted on a Leica TCS SP8 X microscope system (Leica Microsystems) with an incubator chamber at 37°C with 5% CO_2. In addition to the H2B-mCherry reporter we also used Hoechst nucleic acid dye (ThermoFisher # H3570) to visualize micronuclei formation. Cells were incubated with 1 µg/mL Hoechst nucleic acid dye for 2 hours before the imaging experiment. Media was replaced with normal culture media prior to imaging. For the imaging, 10 fields of view were taken for each sample over a span of 24 hours. To quantify micronuclei formation, we used the Leica SP8 LasX software. We used both Hoechst and H2B mCherry to identify the nucleus and determine if there were any discrete DNA aggregates separate from the nucleus that may represent micronuclei. Identified micronuclei showed both Hoechst staining and H2B-mCherry signal. Cells with nuclei associated with at least 1 micronucleus were considered positive.

Generation of MDA-MB-231, PANC1 and SK-MEL-28 *CAPG* and *CAPZA3* KO cell lines.

CAPG and *CAPZA3* targeting gRNAs to generate the human KO lines were identified using CRISPick (https://portals.broadinstitute.org/gppx/crispick/public). These gRNAs were cloned into a plasmid containing Cas9 and a BFP reporter (Addgene Plasmid # 64216) and cutting efficiency was tested in 293T after transient transfection using lipoD293T and the T7E1 assay. The gRNA with the highest cutting efficiency was used for the targeting experiments. In brief, MDA-MB-231, PANC1 and SK-MEL-28 cell lines were dissociated into single cells and replated at a density of 1 million cells per well into a 12 well plate. The cells were then transfected with the BFP reporter plasmid containing *CAPG* and *CAPZA3* targeting gRNAs using Lipofectamine 3000 (ThermoFisher # L3000008). 2 days after transfection the cells were sorted and plated as individual cells into each well of 96 well plates. Cells were expanded and then divided into 1 plate for continued culture and 1 plate for colony PCR and sequencing. DNA Quick Extract (Lucigen # 76081-766) was used to isolate DNA. The *CAPG* and *CAPZA3* loci were then amplified by PCR and submitted for Sanger sequencing. Those clones that showed mutations at these loci were expanded and frozen down. For all targeting experiments we also isolated and froze down lines that had undergone the targeting procedure, but whose genomic sequence at *CAPG* and *CAPZA3* was not changed, these were used as our passage-matched WT controls. Oligonucleotide sequences and KO lines used for experiments are listed in Supplementary Tables.

Generation of *CEACAM1* KO cell lines: *CEACAM1* targeting gRNAs to generate the human KO lines were identified using CRISPick (https://portals.broadinstitute.org/gppx/crispick/public). These gRNAs were cloned into a plasmid containing Cas9 and a BFP reporter (Addgene Plasmid # 64216) and cutting efficiency was tested in 293T after transient transfection using lipoD293T and the T7E1 assay. The gRNA with the highest cutting efficiency was used for the targeting experiments. PANC1 WT, CAPG KO and CAPZA3 KO cell lines were used for targeting. Transfection, sorting, expansion, and sequencing were carried out as described above. To generate single *CEACAM1* KO, *CEACAM1*/*CAPG* DKO and *CEACAM1*/*CAPZA3* DKO cell lines. We also isolated and froze down WT, *CAPG* KO and *CAPZA3* KO cell lines that had undergone the *CEACAM1* targeting procedure, but whose genomic sequence at *CEACAM1* was not changed, these were used as our passage-matched controls.

Generation of PANC1 *AAVS1* TLR cell line and *CAPG*, *CAPZA3* KOs, and testing HDR/NHEJ efficiency

Traffic light reporter (TLR) constructs were ordered from Addgene (Plasmid #s 64323, 64322, 64216, and 64215) and transfected into PANC1 using Lipofectamine 3000 (ThermoFisher # L3000008) per the manufacturer's protocol. We decided to generate the TLR reporter in the PANC1 background as PANC1 cells showed higher transfection efficiencies than MDA-MB-231 or SK-MEL-28 lines. 1 day following transfection of a plasmid containing a BFP reporter and the *AAVS1* targeting gRNA and the pAAVS1-TLR targeting plasmid we sorted BFP positive cells into 1 cell per well of a 96 well plate. After the cells had expanded, genomic DNA was isolated for colony PCR. After identifying and expanding the targeted clones we performed allele specific PCR and found that both of our targeted PANC1 lines had homozygous insertions of the TLR construct into the *AAVS1* locus. We verified that after transfection with the pU6-sgRosa26-1_CBh-Cas9-T2A-BFP plasmid (Addgene Plasmid # 64216) which contains a *Rosa26* targeting gRNA, the cells expressed RFP and GFP. These lines (PANC1 *AAVS1* TLR) were expanded and frozen down. *CAPG* and *CAPZA3* KOs were generated in these lines using the protocols described above. As described above, passage-matched WT controls were those PANC1 *AAVS1* TLR cells that went through the same transfection with *CAPG* and *CAPZA3* gRNAs and clonal expansion procedure but did not show any mutations at the *CAPG* or *CAPZA3* locus.

To analyze HDR and NHEJ efficiency using the TLR reporter, we transfected the pU6-sgRosa26-1_CBh-Cas9-T2A-BFP plasmid (Addgene Plasmid # 64216) which contains a *Rosa26* targeting gRNA and the pTLR repair vector (Addgene Plasmid # 64322) into WT, *CAPG* KO and *CAPZA3* KO PANC1 *AAVS1*

TLR lines. Transfection was done using Lipofectamine 3000 (ThermoFisher # L3000008), based on the manufacturer's protocol. 1 day after transfection the media was replaced. We performed flow analysis by gating on BFP positive cells (which represented transfected cells) and then quantifying the precent GFP and RFP positive cells at 24, 48 and 72 hours after transfection.

RNA-seq

For RNA-seq, total RNA was isolated with the RNeasy Mini Kit (Qiagen # 74136) from B16F10 WT and *Capza3* KO cells, before and after radiation treatment (1 Gy). The *Capza3* KO cell lines were generated as described above. RNA was collected 1 day after radiation treatment. We performed transcriptome profiling using RNA-seq in WT and *Capza3* KO B16F10 cells, with 2 independent clones from each genotype/group (WT, *Capza3* KO gRNA 2, and *Capza3* KO gRNA 3), with biological duplicates for each clone (2 x 2 = 4, quadruplicates for each genotype). The cells were analyzed before and after radiation treatment, for a total of 24 samples. RNA samples were submitted to the YCGA core for library prep and sequencing.

Sequencing data were aligned to the mouse genome (GRCm39) using the STAR aligner v2.7.11 [68]. Briefly, an alignment reference panel was created from the Gencode vM32 primary genome assembly with a sjdbOverhang of 149 (read length – 1). Alignment was performed using the "TranscriptomeSAM" quantification mode from STAR, and transcript counts were estimated using RSEM v1.3.3 [69] with the "rsem-calculate-expression" function. The gene count data were filtered and analyzed using the edgeR R package pipeline [70] with a 2-step upper quartile normalization [71], and the full statistical model included the following covariates: gene-targeting guides (GT) and gRNA, given that two different gRNAs were used (~ GT + gRNA). A likelihood ratio test was used to compare B16F10 cells treated with gene-targeting and non-targeting gRNAs. Transcription factor activity prediction was performed using the decoupleR R package v2.2.2 [72] with the run_fgsea function, the DoRothEa database [73] for directional interactions between TF/target-genes from the (mouse data; A- C interaction confidence), and 1000 iterations.

Quantitative-PCR

Total RNA was isolated with the RNeasy Mini Kit (Qiagen # 74136). DNA was removed from RNA samples using genomic DNA eliminator spin columns. cDNA was produced from RNA using SuperScript III Reverse Transcriptase kit (Life Technologies # 18080051) or High-Capacity cDNA Reverse Transcriptase kit (Life Technologies # 4368813). Quantitative real-time PCR was performed in triplicate

using PowerTrack QPCR SYBR Green (ThermoFisher # A46109). Oligonucleotide sequences are listed in a Supplementary Table.

Flow cytometry analysis

Surface marker: Cells were disaggregated with TrypLE for 5 minutes and washed with cold wash buffer (2% FBS in PBS). Cells were pelleted by centrifugation and washed again with wash buffer. Each sample was resuspended in wash buffer with the appropriate conjugated antibody and LD APC-Cy7 (Thermo # L34976). Cells were incubated in wash buffer with the antibody for 30 minutes on ice. After staining cells were washed two times with wash buffer and resuspended in wash buffer with DAPI and analyzed by FACS. A complete listing of antibodies used is presented in the key reagents section below. Representative flow plots are shown where appropriate. Gating for human EGFR Car-T cell surface marker staining is shown in a supplemental figure.

Annexin V staining

Supernatant was collected and cells were detached following incubation with 1 mM EDTA for 5 min at RT. Cells were washed twice with wash buffer by centrifuging at 300g for 10 minutes. Cells were then resuspended in 90 µL of 1x Binding Buffer per 10^7 cells and 10 µL of Annexin V-APC antibody and DAPI was added. Cells were incubated for 15 minutes at 4C before washing twice with 1x Binding Buffer and centrifugation at 300g for 10 minutes. Cells were then analyzed by FACS.

EGFR-CAR-T cell generation

Cryopreserved PBMCs were obtained from StemCell Technologies (Catalog # 70025). PBMCs were thawed and CD3+ T cells were isolated immediately by Pan T Cell Isolation Kit (Miltenyi # 130-096-535). Then isolated T cells were incubated by CD3/CD28 Dynabeads (Thermofisher # 11131D) for T Cell expansion and activation for 48 hours. Following activation, the T cells were transduced with lentiviral generated using EFS-scFv-CD8TM-41BBL-CD3zeta-T2A-Puro-WPRE (Sidi Chen lab). The T cells were transduced by spin-infection, in which 50 µL of concentrated lentivirus was added to 1 million activated CD3+ T cells in 1 ml of complete media (X-VIVO with 5% AB Serum and IL2) with 8 µg/ml of polybrene. Cells with lentivirus were spun at 900g at 37C for 90 minutes, followed by incubation for 24 hours in 37C incubator. Following incubation, virus was removed and puromycin (1ug/ml) was add for 5 days to get successfully transduced CAR-T cells. Expression of the CAR receptor was confirmed using Flag flow cytometry.

PANC1/MDA-MB-231 Co-culture

PANC1 and MDA-MB-231 cells were plated in 48 well plates for 24 hours prior to the addition of EGFR CAR-T cells. PANC1 cells were plated at a density of 100K cells/well and MDA-MB-231 were plated at a density of 50K cells/well. 6 hours after plating the cells were irradiated and 24 hours after irradiation we added the EGFR CAR-T at a 1:1 T:E ratio. We observed significant cell death by 12 hours for the PANC1 co-culture and by 24 hours for the MDA-MB-231 co-culture. Thus, these were the time points we decided to halt the experiment and quantify the number of surviving cancer cells using FACS. In brief, all cells (attached and detached) were collected. The cells were washed 2x in cold wash buffer (2% FBS in PBS). Cells were stained with LD APC-Cy7 (Thermo # L34976) and CD3 FITC (Biolegend # 300406). For all experiments a sample of cancer cells alone and EGFR Car-T cells alone were used as gating controls. Using FACS we counted the total number of live cells within a sample and then analyzed the number of these live cells that were CD3 negative to obtain the number of surviving cancer cells. Representative FACs plots showing gating and CD3 staining are show in a supplemental figure. For some experiments anti-human TIM3 antibody (Biolegend # 345009, 10 µg/ml) or anti-human PD1 antibody (BioXCell # BE0188, 10 µg/ml) was added during co-culture with EGFR CAR-T for blocking/neutralization.

TCGA analysis

We obtained processed data from the TCGA GDC data portal (https://portal.gdc.cancer.gov/) and curated clinical and mutation information from UCSC Xena [74]. Proportions of tumor-infiltrated immune cells were estimated from gene expressions using the 'MCPcounter' package [75]. Differentially expressed genes between high and low *CAPG/CAPZA3* expression patients were identified using the 'limma' package. Pathway enrichments were conducted in R (v4.3.0) using the 'clusterProfiler' package [76].

Statistical Analysis

Data are presented as means ± SD, unless otherwise noted. Data was compared using Student's *t* test, or ANOVA with repeated measures when appropriate. The test used is indicated in the figure legends. All tests were two-sided. Statistical analyses were carried out using GraphPad Prism. A p value of less than 0.05 was considered statistically significant.

Illustrations

Illustration of schematics were performed using Affinity Designer and Biorender (https://www.biorender.com).

Inclusion & Ethics

We take diversity, inclusion and related ethics as part of our value. One or more author(s) self-identified as under-represented minority.

Reporting summaries

Statistics

For all statistical analyses, we confirmed that the items mentioned in NPG reporting summary are present in the figure legend, table legend, main text, or Methods section.

Software and code

Data collection

Flow cytometry data were collected by Attune NxT Flow Cytometer (Thermo), Four-laser Aria II (BD), Five-laser Symphony S6 (BD), Cytek Aurora (Cytek Biosciences); All the deep sequencing data were collected by Yale Center for Genome Analysis (YCGA).

Data analysis

Data analysis was performed using the following software / packages:

Prism 10.1.0; FlowJo v.10.9.0; Prism 9; CRISPResso2 v2.1.3; Bowtie 1.3.0; Cutadapt v3.4.0; EdgeR v3.38.4; stringr v1.5.0; dplyr v1.1.1; ggplot2 v3.4.1; ggrastr v1.0.1; ggrepel v0.9.3; patchwork v1.1.2; cowplot v1.1.1; reshape2 v1.4.4; factoextra v1.0.7; limma v3.52.4; cluster v2.1.4; DESeq2 v1.36.0; SAMBA v2.0

Standard statistical analysis

All statistical methods are described in figure legends and/or supplementary Excel tables. The *p* values and statistical significance were estimated for most analyses. One-way ANOVA, two-way ANOVA, Dunnett's multiple comparisons test, Tukey's multiple comparisons test was used to compare multiple groups. Data between two groups were analyzed using a two-tailed unpaired *t*-test. Different levels of statistical significance were accessed based on specific *p* values and type I error cutoffs (0.05, 0.01, 0.001, 0.0001). Data analysis was performed using GraphPad Prism v.10. and RStudio. Source data and statistics were provided in a supplemental excel table.

Data and resource availability

All data generated or analyzed during this study are included in this article and its supplementary information files. Specifically, source data and statistics for non-high-throughput experiments such as flow cytometry, protein experiments, and other molecular or cellular assays are provided in an excel file of Source data and statistics. Processed data for genomic sequencing (e.g. CRISPR, targeted amplicon

sequencing, and RNA sequencing) and other forms of high-throughput experiments are provided as processed quantifications in Supplementary Datasets. Genomic sequencing raw data are being deposited to NIH Sequence Read Archive (SRA) and/or Gene Expression Omnibus (GEO). All data and materials that support the findings of this research are available from the corresponding author upon reasonable request to the academic community.

Code availability

Analytic codes used to generate figures that support the findings of this study will be available from the corresponding author upon request.

Life sciences study design

Sample size determination

Sample size was determined according to the lab's prior work or similar approaches in the field.

Data exclusions

No samples were excluded from data analyses.

Replication

All experiments were done with at least three biological replicates or two infection replicates. Experimental replications were indicated in detail in methods section and in each figure panel's legend.

Blinding

Investigators were not blinded in *in vitro* experiments. In certain NGS data analysis, such as CRISPR screen and RNA sequencing, investigators were blinded for initial processing of the original data using key-coded metadata.

Reporting for specific materials, systems and methods

Antibodies

Mouse PD1	BioXCell	BE0146	Neturalization antibody
Human PD1	BioXCell	BE0188	Neturalization antibody
Human TIM3	Biolegend	345009	Neturalization antibody
yH2AX	Cell Signaling Technology	9718T	Immunofluorescence
53BP1	Novus Biologicals	NB100-904	Immunofluorescence
RPA32	Bethyl Laboratories	A300-246A	Immunofluorescence
Human STING	Cell Signaling Technology	13647	Western Blot
Human TBK	Cell Signaling Technology	3504	Western Blot
Human IRF3	Cell Signaling Technology	11904	Western Blot
Human GAPDH	Thermofisher	MA1-16757	Western Blot
Mouse PDL1-APC	Biolegend	124311	Flow cytometry
OVA-MHCII APC	Biolegend	141605	Flow cytometry
Human CEACAM1-PE	Fisher	53-0668-41	Flow cytometry
Human CEACAM1-488	Thermofisher	53-0668-41	Flow cytometry
Flag PE	Biolegend	637310	Flow cytometry
EGFR PE	Biolegend	352903	Flow cytometry
Human PDL1 APC	Biolegend	329707	Flow cytometry
Mouse PD1-APC	Biolegend	135210	Flow cytometry
Mouse LAG3-PE	Biolegend	125207	Flow cytometry
Mouse TIGIT-APC	Biolegend	142105	Flow cytometry
Mouse CD160-PE	Biolegend	143003	Flow cytometry
Annexin V APC	Biolegend	640932	Flow cytometry
Human CD3 FITC	Biolegend	300306	Flow cytometry
Human CD69 BV421	Biolegend	310930	Flow cytometry
Human CD25 PE	Biolegend	356103	Flow cytometry
Human LAG3 PerCp-5.5	Biolegend	125211	Flow cytometry
Human TIM3 PE-Cy7	Biolegend	119715	Flow cytometry
Human PD1-APC	Biolegend	329907	Flow cytometry

Plasmids

Brie genome-scale CRISPR library	Addgene	73633	CRISPR lentiviral library
lentiCas9-Blast	Addgene	52962	Generate B16F10-Cas9 line
OVA-mCherry	Chen lab	NA	Generate B16F10-Cas9-OVA line to be used in screen
LRG (Lenti_sgRNA_EFS_GFP)	Addgene	65656	Generage *Capza3* KO in B16F10
H2B-mCherry	Addgene	20972	Express H2B-mCherry in B16F10 *Capza3* KO
HR extra-chromosomal luciferase reporter	Glazer lab	NA	Assess to HR rate in B16F10, MDA231, PANC1, SKMEL28
NHEJ extra-chromosomal luciferase reporter	Glazer lab	NA	Assess to HR rate in B16F10, MDA231, PANC1, SKMEL28
Luciferase transfection control	Glazer lab	NA	Assess to HR rate in B16F10, MDA231, PANC1, SKMEL28
pU6-(BbsI)_CBh-Cas9-T2A-BFP-P2A-Ad4R1B	Addgene	64218	Generate PANCI AAVS1 TLR line
pU6-sgRosa26-1_CBh-Cas9-T2A-BFP	Addgene	64216	Generate PANCI AAVS1 TLR line
pAAVS1-TLR targeting vector	Addgene	64215	Generate PANCI AAVS1 TLR line

Antibody validation

Antibodies were validated based on manufacturing instructions.

Eukaryotic cell lines

Cell line source(s)

B16F10	ATCC	CRL-6475
MDA231	ATCC	CRM-HTB-26
PANC1	ATCC	CRL-1469
SKMEL28	ATCC	HTB-72
Human PBMC	StemCell Technologies	70025

Authentication

Cell lines were authenticated by the commercial vendor.

Mycoplasma contamination

All the cell lines used here tested negative for mycoplasma contamination.

Commonly misidentified lines (See ICLAC register)

No commonly misidentified line was used in the study.

Animals and other organisms

Laboratory animals

OT-I mice were purchased from the Jackson Laboratory and bred in-house. Both male and female OT-I mice between 6 to 12 weeks old were used.

Wild animals

N/A

Field-collected samples

N/A

Figure Legends

Figure 1. Genome-wide B16F10 CRISPR Screen identifies that inactivation of actin capping proteins, *Capg* and *Capza3*, promotes B16F10 survival following radiation and co-culture with anti-PD1 antibody and CD8 cytotoxic T cells.

a, Schematic of the B16F10 genome-scale CRISPR KO screen is shown on the left. Validation experiment of WT B16F10 and *Capza3* KO B16F10 cell survival following co-culture with OT-I CD8+ T cells is shown on the right.

b, Screen analysis plot (left) and top 6 gRNAs enriched (right) in surviving B16F10 cells after low-dose radiation (1 Gy) treatment and co-culture with CD8 cytotoxic T cells. Results shown are from 2 biologic repeats of the screen.

c, Screen analysis plot (left) and top 6 gRNAs enriched (right) in surviving B16F10 cells after low-dose radiation (1 Gy) treatment and anti-PD1 antibody treatment during co-culture with CD8 cytotoxic T cells. Results shown are from 2 biologic repeats of the screen.

d, Screen analysis plot (left) and top 6 gRNAs enriched (right) in surviving B16F10 cells after anti-PD1 antibody treatment during co-culture with CD8 cytotoxic T cells. Results shown are from 2 biologic repeats of the screen.

e, Validation experiment of WT B16F10 and *Capza3* KO B16F10 cell survival. *Capza3* KO B16F10 cells were transduced with lentivirus containing the *Capza3* targeting gRNA and a GFP reporter. Prior to transduction of B16F10 cells, some cells were isolated to be used as a WT control. Flow analysis of % GFP positive cells (B16F10 Cas9 cells transduced with lentivirus that contains the *Capza3*-targeting gRNA) following either: 1) co-culture with CD8 cytotoxic T cells or 2) treatment with low-dose radiation (1 Gy) and anti-PD1 antibody during co-culture with CD8 T cells. Representative plots are shown on the left and quantification is shown on the right. Significance testing was performed with two-way ANOVA. Validation experiments were performed using three biological replicates for each treatment condition. * $p < 0.05$, ** $p < 0.01$, *** $p < 0.001$, **** $p < 0.0001$.

Figure 2. B16F10 *Capza3* KO cells show increased DNA damage after exposure to radiation.

a, Representative immunofluorescence staining of γH2AX (left), 53BP1 (middle) and phospho-RPA2 (pRPA, right) foci in WT and *Capza3* KO cells at 6 hours and 24 hours after low-dose (1 Gy) radiation treatment.

b, Quantification of γH2AX (left), 53BP1 (middle) and pRPA (right) foci in WT and *Capza3* KO cells at different timepoints following low-dose (1 Gy) radiation treatment. Significance testing was performed with two-way ANOVA, three biological replicates were done for each sample and treatment condition.

c, Quantification of total γH2AX foci in individual WT and *Capza3* KO cells 24 hours after low-dose (1 Gy) radiation treatment. Significance testing was performed with one-way ANOVA, individual cell data from three biological replicates were pooled together for each sample.

d, Quantification of γH2AX foci in WT and *Capza3* KO cells 24 hours after exposure to different doses of radiation treatment. Significance testing was performed with two-way ANOVA, three biological replicates were done for every sample and treatment condition.

e, Colony forming ability (CFA) of WT and *Capza3* KO cells after exposure to different doses of radiation treatment. The survival fraction for each treatment was determined after normalization with the colony number seen in the no treatment control for each cell line. Significance testing was performed with two-way ANOVA, the p value for WT vs *Capza3* gRNA 2 is shown in blue and the p value for WT vs *Capza3* gRNA 3 is shown in red. Three biological replicates were done for each sample and treatment condition.

f, Percent of WT and *Capza3* KO cells that are Annexin V positive 24 hours after exposure to different doses of radiation. Significance testing was performed with two-way ANOVA, three biological replicates were done for each sample and treatment condition.

g, CFA of WT and *Capza3* KO cells after treatment with varying doses of Olaparib. The survival fraction for each treatment was determined after normalization with the colony number seen in no treatment control for each cell line. Significance testing was performed with two-way ANOVA, the p value for WT vs *Capza3* gRNA 2 is shown in blue and the p value for WT vs *Capza3* gRNA 3 is shown in red. Three biological replicates were done for each sample and treatment condition.

h, Cell cycle analysis of WT and *Capza3* KO cells during maintenance culture. Gating for G1, S and G2 are shown in the representative flow plots with quantification of proportion of cells in G1, S, and G2 phases in the graph below. Significance testing was performed with two-way ANOVA, the p value for WT vs *Capza3* gRNA 2 is shown in blue and the p value for WT vs *Capza3* gRNA 3 is shown in red. Three biological replicates were done for each sample.

For all experiments, WT cells were transduced with a lentiviral vector expressing a NTC gRNA. * $p < 0.05$, ** $p < 0.01$, *** $p < 0.001$, **** $p < 0.0001$.

Figure 3. B16F10 *Capza3* KO cells have impaired HDR compared to WT cells.

a, Schematic of extra-chromosomal reporters used to analyze efficiency of HDR and NHEJ in WT and *Capza3* KO B16F10 cells.

b, Quantification of luciferase activity, compared to WT cells, 48 hours after transfection with linearized HDR and NHEJ extrachromosomal reporters. Significance testing was performed with two-way ANOVA, Three biological replicates were done for each sample. P-values: WT vs. *Capza3* gRNA 2 KO #1: 0.0071, WT vs *Capza3* gRNA 2 KO #2: 0.0062, WT vs *Capza3* gRNA 3 KO #1: <0.0001, WT vs *Capza3* gRNA 3 KO #2: <0.0001.

c, Schematic of laser micro-irradiation to induce DNA damage followed by fixation and staining with γH2AX at different time points to monitor dispersion of DNA damage foci following laser micro-irradiation.

d, Representative immunofluorescence imaging of γH2AX DNA damage foci 1 minute and 20 minutes following laser micro-irradiation in WT and *Capza3* KO cells.

e, Quantification in individual cells of the ratio of intensity of γH2AX staining in the region of laser induced DNA damage versus outside this region, 1 minute and 20 minutes after laser micro-irradiation. Analysis was done using ImageJ. Significance testing was performed with two-way ANOVA, individual cell data from three biological replicates were pooled together for each sample. P-values: WT vs. *Capza3* gRNA 2 KO #1: <0.0001, WT vs *Capza3* gRNA 2 KO #2: 0.0024, WT vs *Capza3* gRNA 3 KO #1: <0.0001, WT vs *Capza3* gRNA 3 KO #2: 0.0087.

f, Average intensity of γH2AX stripe in the region of laser induced DNA damage in WT and *Capza3* KO cells at different time points after laser micro-irradiation. Significance testing was performed with two-way ANOVA, the average intensity from three biological replicates is shown. P-values: WT vs. *Capza3* gRNA 2 KO #1: ns, WT vs *Capza3* gRNA 2 KO #2: ns, WT vs *Capza3* gRNA 3 KO #1: 0.0082, WT vs *Capza3* gRNA 3 KO #2: 0.0157.

g, 24 hours live cell imaging of WT and *Capza3* KO cells with Hoechst staining and a H2B fluorescent reporter to monitor proportion of cells that show micronuclei formation following 1 Gy radiation treatment. Micronuclei formation was quantified in 10 representative fields of view. Cells with at least one micronuclei were considered positive. Significance testing was performed with one -way ANOVA, two replicates were done, with 10 fields quantified for each replicate.

For all experiments, WT cells were transduced with a lentiviral vector expressing a NTC gRNA. * $p < 0.05$, ** $p < 0.01$, *** $p < 0.001$, **** $p < 0.0001$.

Figure 4. PANC1 and MDA-MB-231 *CAPG* and *CAPZA3* KO cell lines show increased DNA damage following radiation treatment and impaired HDR.

a, Representative γH2AX immunofluorescence staining 24 hours after radiation treatment (5 Gy) in WT, *CAPG* and *CAPZA3* KO PANCI and MDA-MB-231 cell lines.

b, Quantification of γH2AX foci in WT, *CAPG* and *CAPZA3* KO MDA-MB-231 (left) and PANC1 (right) cell lines 24 hours after different doses of radiation treatment. Significance testing was performed with two-way ANOVA, three biological replicates were done for each sample and treatment condition.

c, Quantification of total γH2AX foci in individual cells in WT, *CAPG* and *CAPZA3* KO MDA-MB-231 (left) and PANC1 (right) cell lines 24 hours after exposure to 5 Gy radiation. Significance testing was performed with one-way ANOVA, individual cell data from three biological replicates were pooled together for each sample. P-values are shown for comparisons of the KO line (*CAPG* KO or *CAPZA3* KO) to WT.

d, Quantification of luciferase activity, compared to WT cells, 48 hours after transfection with a linearized HDR extrachromosomal reporter. Significance testing was performed with one-way ANOVA. 4 biological replicates were done for the MDA-MB-231 and 6 biological replicates were done for the PANC1. MDA-MB-231 p-values: WT vs. *CAPG* KO #1: <0.0001, WT vs *CAPG* KO #2: 0.0012, WT vs *CAPZA3* KO #1: <0.0001, WT vs *CAPZA3* KO #2: <0.0001. PANC1 p-values: WT vs. *CAPG* KO #1: 0.0003, WT vs *CAPG* KO #2: <0.0001, WT vs *CAPZA3* KO #1: 0.0011, WT vs *CAPZA3* KO #2: <0.0001.

e, CFA of WT, *CAPG* and *CAPZA3* KO MDA-MB-231 (left) and PANC1 (right) cell lines after different doses of radiation treatment. Surviving fraction for each treatment was determined after normalization with the colony number seen in no treatment control for each cell line. Significance testing was performed with two-way ANOVA, the p value for WT vs *CAPG* KO is shown in blue and the p value for WT vs *CAPZA3* KO is shown in red. Three biological replicates were done for each sample and treatment condition.

f, Colony forming ability of WT, *CAPG* and *CAPZA3* KO PANC1 cell lines after treatment with different doses of cisplatin. Surviving fraction for each treatment was determined after normalization with the colony number seen in no treatment control for each cell line. Significance testing was performed with two-way ANOVA, the p value for WT vs *CAPG* KO is shown in blue and the p value for WT vs *CAPZA3* KO is shown in red. Four biological replicates were done for each sample and treatment condition.

g, Representative flow plots of RFP positive and GFP positive cells 48 hours after transfection of Rosa26 gRNA into PANC1 AAVS1 traffic light reporter (TLR) cells: NT (WT not transfected), WT, *CAPG* and *CAPZA3* KO cell lines.

h, Quantification of GFP positive cells (left, % cells with successful HDR) and RFP positive cells (right, % cells with successful NHEJ) 24 and 48 hours after transfection of *Rosa26* gRNA in PANC1 *AAVS1* TLR WT, *CAPG* and *CAPZA3* KO cell lines. Significance testing was performed with two-way ANOVA, four biological replicates were done for each sample.

For all experiments, WT cells were passage-matched controls that underwent the procedure to generate KO cell lines (transfected with plasmid containing *CAPG* or *CAPZA3* targeting gRNA, sorted as single cells into a 96 well plate and expanded) but did not have a mutation at either the *CAPG* or *CAPZA3* locus. * $p < 0.05$, ** $p < 0.01$, *** $p < 0.001$, **** $p < 0.0001$.

Figure 5. B16F10 *Capza3* KO cells and PANC1 *CAPG*/*CAPZA3* KO cells show increased activation of the STING pathway and increased expression of *CEACAM1* compared to WT cells.

a, Heat map shows differentially expressed genes between WT and *Capza3* KO B16F10 cells before (left) and after (right) low-dose (1 Gy) radiation treatment from bulk RNA-Seq analysis of WT and *Capza3* KO B16F10 cells.

b, plot of genes differentially expressed between *Capza3* KO and WT cells before radiation treatment (top) and after radiation treatment (bottom) from bulk RNA-Seq analysis of WT and *Capza3* KO B16F10 cells.

c, Analysis of transcription factor pathways that are significantly upregulated in *Capza3* KO compared to WT B16F10 cells before (left) and after (right) low-dose (1 Gy) radiation treatment. Pathway activation confidence is depicted as a score from 0 to 1, representing the confidence of the relationship between the indicated gene and pathway. Analysis was done on bulk RNA-Seq data of WT and *Capza3* KO B16F10 cells.

d, Targets of the IRF1 transcription factor that showed the greatest upregulation in *Capza3* KO compared to WT B16F10 cells before (top) and after (bottom) low-dose (1 Gy) radiation treatment.

e, Western blot analysis of expression of STING pathway components in PANC1 (left) and MDA-MB-231 (right) WT, *CAPG* KO and *CAPZA3* KO cell lines before and after low-dose (1 Gy) radiation treatment.

f, qPCR analysis of *CEACAM1* expression in B16F10 (left), MDA-MB-231 (middle) and PANC1 (right) WT and KO cell lines before and after low-dose (1 Gy) radiation treatment. Significance testing was performed with two-way ANOVA, three biological replicates were done for each sample and treatment condition.

g, Representative flow plots of CEACAM1-488 staining in WT, *CAPG* KO and *CAPZA3* KO PANC1 cell lines before and after low-dose (1 Gy) radiation treatment. Quantification of CEACAM1 positive cells is shown on the bottom. Significance testing was performed with two-way ANOVA, four biological replicates were done for each sample and treatment condition.

For RNA-Seq analysis, n = 2 biologic replicates for each cell line (WT #1, WT #2, *Capza3* gRNA 2 KO #1, *Capza3* gRNA 2 KO #2, *Capza3* gRNA 3 KO #1, *Capza3* gRNA 3 KO #2) and each condition (no radiation or after 1 Gy radiation) for a total of 24 samples submitted for sequencing.

For B16F10, WT cells were transduced with a lentiviral vector expressing a NTC gRNA. For PANC1 and MDA-MB-231 For all experiments, WT cells were passage-matched controls that underwent the procedure to generate KO cell lines (transfected with plasmid containing *CAPG* or *CAPZA3* targeting gRNA, sorted as single cells into a 96 well plate and expanded) but did not have a mutation at either the *CAPG* or *CAPZA3* locus.

* $p < 0.05$, ** $p < 0.01$, *** $p < 0.001$, **** $p < 0.0001$.

Figure 6. PANC1 *CAPG*/*CAPZA3* KO cells lose their survival advantage following co-culture with EGFR CAR-T after inactivation of *CEACAM1* or with co-culture with anti-TIM3 antibody.

a, Schematic of co-culture experiments using MDA-MB-231 and PANC1 cell lines with EGFR CAR-T cells. Specific KO cell lines and different treatment conditions that were analyzed are shown.

b, Representative flow plots of EGFR chimeric antigen receptor (CAR) Flag tag on EGFR CAR-T cells.

c, Representative flow plots of EGFR expression in MDA-MB-231 and PANC1 cell lines.

d, Analysis of cell survival after exposure to radiation and co-culture with EGFR CAR-T for WT, *CAPG* KO and *CAPZA3* KO PANC1 (left) and MDA-MB-231 (right) cell lines. Significance testing was performed with two-way ANOVA, three biological replicates were done for each sample and treatment condition.

e, Representative flow plot of CEACAM1 flow analysis in EGFR CAR-T cells during regular maintenance culture.

f, Representative flow plots of inhibitory receptor expression on EGFR CAR-T during regular maintenance culture.

g, Cell survival of PANC1 *CAPG* and *CAPZA3* KO cell lines compared to WT cells following treatment with radiation and/or anti-TIM3 antibody and co-culture with EGFR CAR-T. Significance testing was performed with one-way ANOVA, three biological replicates were done for each sample.

h, Cell survival of PANC1 KO cell lines (*CEACAM1*, *CAPG* and *CAPZA3* single and double KO) compared to WT cells following treatment with radiation and/or anti-TIM3 antibody and co-culture with EGFR CAR-T. Significance testing was performed with two-way ANOVA, three biological replicates were done for each sample and treatment condition.

i, Expression of PDL1 inhibitory ligand in WT, *CAPG* and *CAPZA3* KO PANC1 cell lines following radiation treatment. Representative flow plots are shown on the left and quantification is shown on the right. Significance testing was performed with one-way ANOVA, four biological replicates were done for each sample.

j, Cell survival of PANC1 WT, *CAPG* and *CAPZA3* KO cell lines following treatment with radiation, anti-TIM3 antibody and anti-PD1 antibody and co-culture with EGFR CAR-T. Significance testing was performed with two-way ANOVA, all comparisons were made to the no radiation or antibody treatment control. WT p-values: No RT or Ab vs. RT: 0.1014, No RT or Ab vs. RT + TIM3 Ab: 0.1298, No RT or Ab vs. RT + PD1 Ab: 0.5644. *CAPG* KO p-values: No RT or Ab vs. RT: 0.9986, No RT or Ab vs. RT + TIM3 Ab: 0.0178, No RT or Ab vs. RT + PD1 Ab: 0.0279. *CAPZA3* KO p-values: No RT or Ab vs. RT: 0.6799, No RT or Ab vs. RT + TIM3 Ab: 0.0032, No RT or Ab vs. RT + PD1 Ab: 0.0027. Three biological replicates were done for each sample and treatment condition.

For all experiments, WT cells were passage-matched controls that underwent the procedure to generate KO cell lines (transfected with plasmid containing *CAPG* or *CAPZA3* targeting gRNA, sorted as single cells into a 96 well plate and expanded) but did not have a mutation at either the *CAPG* or *CAPZA3* locus. * $p < 0.05$, ** $p < 0.01$, *** $p < 0.001$, **** $p < 0.0001$.

Figure 7. TCGA data analysis of tumor mutational burden, CD8 T cell infiltration and overall survival in patients with inactivating mutations or low expression of *CAPG*, *CAPZA3* and known HDR associated genes.

a, The statistical significance of the co-occurrence of *CAPG*/*CAPZA3* mutations with other HDR genes mutations evaluated using Fisher's exact test.

b, Expression of *CAPG* (top) and *CAPZA3* (bottom) in different cancer types.

c, Analysis of tumor mutational burden in patients with an isolated inactivating mutation in *CAPG* or *CAPZA3* or a mutation in a single HDR associated gene. P-values are shown for selected comparisons. Significance testing was performed with one-way ANOVA.

d, Ranking of the correlation between CD8 T cell tumor infiltration and expression of genes within the genome are shown. Correlation was determined from the calculation of spearman correlation coefficient

and ranges from +1 (left) to -1 (right). *CAPG* (blue), *CAPZA3* (red) and other known HDR associated genes (black) are highlighted.

e, Pathway-level alterations between patients with high and low expression of *CAPG* (top) and *CAPZA3* (bottom) were estimated by comparing the gene expression profiles of patients in the top and bottom quantiles for *CAPG*. For *CAPZA3,* 50% of tumor samples in the TCGA dataset had a 0 expression value for *CAPZA3* and so we compared the gene expression profiles of patients showing any expression of *CAPZA3* compared to those that had a 0 expression value.

f, Heat map of relationship between HDR gene expression and patient survival for different cancer types. HR is shown by the color of the circle. A HR >1 reflects that increased expression of the HDR gene is associated with poorer survival. Size of the circle indicates the p-value from Cox univariate regression analysis.

g, Survival of patients stratified based on low versus high expression of *CAPG* or *CAPZA3* in different cancer types. Significance was determined using Log Rank Test.

h, Diagram of proposed mechanistic model.

Supplementary Figure Legend

Supplementary Figure 1. Validation of the screening method using co-culture of *Pdl1* KO B16F10 cells expressing Cas9 protein and OVA antigen (B16F10) with OT-I CD8 T cells.

a, Flow analysis of OVA antigen expression in Cas9 expressing B16F10 cells used for the CRISPR screen (hereafter referred to as B16F10).

b, Flow analysis of PD1, LAG3, TIGIT and CD160 of OT-I CD8 T cells. Prior to co-culture with B16F10-OVA cells, CD8 T cells isolated from OT-I mice and were cultured with OVA antigen for 3 days.

c, Flow cytometry analysis of PDL1 in B16F10 cells transduced with lentivirus containing either an empty LRG vector (WT control) or the LRG vector carrying either *Pdl1* targeting gRNA #1 (PDL1 KO #1) or *Pdl1* targeting gRNA #2 (PDL1 KO #2).

d, Annexin V and DAPI staining of control and *Pdl1* KO B16F10-OVA cells following co-culture with OT-I CD8 T cells.

e, Flow cytometry analysis of WT B16F10 cells following co-culture with OT-I CD8 T cells and Annexin V column purification.

f, WT and *Pdl1* KO cells were mixed at a 1:1 ratio before co-culture with OT-I CD8 T cells. 24 hours after co-culture cells underwent Annexin V column purification and Annexin V negative and Annexin V positive fractions were analyzed with Annexin V staining and flow cytometry analysis.

g, WT and *Pdl1* KO cells were mixed at a 1:1 ratio before co-culture with OT-I CD8 T cells. 24 hours after co-culture cells underwent Annexin V column purification and Annexin V negative and Annexin V positive fractions were analyzed with PDL1 staining and flow cytometry analysis.

Supplementary Figure 2. Flow cytometry verification of Annexin V column separation in B16F10 CRISPR screen.

a, Flow analysis from screen replicate #1 of Annexin V staining in the Annexin V negative fraction following column purification. The 4 screen treatment conditions are shown: co-culture with CD8 T cells without radiation or PD1 antibody, low-dose radiation (1 Gy) treatment and co-culture with CD8 cytotoxic T cells, anti-PD1 antibody treatment during coculture with CD8 cytotoxic T cells and low-dose radiation (1 Gy) treatment followed by anti-PD1 antibody treatment during co-culture with CD8 cytotoxic T cells.

b, Flow analysis from screen replicate #1 of Annexin V staining in the Annexin V positive fraction following column purification. The 4 screen treatment conditions are shown: co-culture with CD8 T cells without radiation or PD1 antibody, low-dose radiation (1 Gy) treatment and co-culture with CD8 cytotoxic

T cells, anti-PD1 antibody treatment during coculture with CD8 cytotoxic T cells and low-dose radiation (1 Gy) treatment followed by anti-PD1 antibody treatment during co-culture with CD8 cytotoxic T cells. For the screen, n = 2 biologic replicates were done for each treatment condition.

Supplementary Figure 3. Sequencing analysis of enriched gRNAs in surviving B16F10-OVA cells following co-culture with OT-I CD8 T cells in the genome scale CRISPR screen.

a, Schematic of B16F10 CRISPR screen. Total B16F10 cell number at each step is shown. 2 independent replicates of each of the 4 treatment conditions were done and analyzed for enriched gRNAs.

b, PCR amplification of gRNA barcode regions in Annexin V positive and Annexin V negative B16F10 fractions from genomic DNA of Annexin V column purified B16F10 cells.

c, Correlation between 2 independent replicates of the screen. Baseline refers to control B16F10 cells that were isolated following lentiviral infection but prior to any treatment (with radiation or anti-PD1 antibody) and prior to co-culture with CD8 T cells. RT refers to radiation treatment alone, PD1 refers to anti-PD1 antibody treatment alone and RT_PD1 refers to the combination of radiation and anti-PD1 antibody treatment. 1 or 2 within the labels refers to replicate 1 or replicate 2.

d, sgRNA detection for baseline and each of the treatment conditions (no treatment, radiation alone, anti-PD1 antibody, radiation and anti-PD1 antibody). 1 or 2 within the labels refers to replicate 1 or replicate 2.

e, PCA analysis of different treatment conditions between the two independent replicates of the screen.

f, Scatter plots of MAGeCK-RRA screen analyses for positive selection. Each plot is titled with the comparison used for the analysis.

g, T7E1 analysis of the 2 *Capza3* targeting gRNAs (Capza3-2 and Capza3-3) that were significantly enriched in surviving B16F10 cells following radiation treatment (with and without anti-PD1 antibody treatment) and co-culture with OT-I CD8 T cells.

h, qPCR analysis of *Capza1*, *Capza2* and *Capza3* expression in B16F10 cell lines transduced with lentivirus containing the 2 *Capza3* targeting gRNAs (gRNA 2 and gRNA 3) that were significantly enriched in surviving B16F10 cells following radiation treatment (with and without anti-PD1 antibody treatment) and co-culture with OT-I CD8 T cells. Significance testing was performed with two-way ANOVA, two biological replicates were done for each sample, * $p < 0.05$, ** $p < 0.01$, *** $p < 0.001$, **** $p < 0.0001$.

Supplementary Figure 4. Sequencing analysis of *Capza3* KO B16F10 cells following transduction with lentivirus containing *Capza3* gRNA 2 and *Capza3* gRNA 3.

a, Analysis of OVA expression (top) or PDL1 (bottom) in B16F10 cells transduced with either lentivirus containing a non-targeting gRNA or the 2 *Capza3* targeting gRNAs that were enriched in the CRISPR screen.

b, Next generation sequencing analysis of the *Capza3* locus in B16F10 cells transduced with lentivirus containing a non-targeting gRNA or the 2 *Capza3* targeting gRNAs that were enriched in the CRISPR screen. Percent modified and unmodified alleles within each cell population are shown.

c, Next generation sequencing analysis of the *Capza3* locus in B16F10 cells transduced with lentivirus containing *Capza*3 gRNA 2. Specific mutations identified within each cell population at the *Capza3* locus are shown.

d, Next generation sequencing analysis of the *Capza3* locus in B16F10 cells transduced with lentivirus *Capza3* gRNA 3. Specific mutations identified at the *Capza3* locus are shown.

For all experiments, WT cells were transduced with a lentiviral vector expressing a NTC gRNA.

Supplementary Figure 5. B16F10 *Capza3* KO cells show increased DNA damage after exposure to radiation.

a, Quantification of total 53BP1 (left) and pRPA (right) foci in individual WT and *Capza3* KO cells 24 hours after 1 Gy radiation treatment. Significance testing was performed with one-way ANOVA, individual cell data from three biological replicates were pooled together for each sample.

b, Quantification of total γH2AX (left), 53BP1 (middle) and pRPA (right) foci in individual WT and *Capza3* KO cells 6 hours after 1 Gy radiation treatment. Significance testing was performed with one-way ANOVA, individual cell data from three biological replicates were pooled together for each sample.

c, Quantification of total γH2AX in individual WT and *Capza3* KO cells 24 hours after different doses of radiation treatment. Significance testing was performed with one-way ANOVA, individual cell data from three biological replicates were pooled together for each sample.

d, Images from colony forming assay of WT and *Capza3* KO cells.

e, Colony forming ability (CFA) of WT and *Capza3* KO cells after different doses of radiation treatment with or without treatment with AZD 7648 (DNA-PK inhibitor, 10 μM). Surviving fraction for each treatment was determined after normalization with the colony number seen in no treatment control for each cell line. Significance testing was performed with two-way ANOVA, three biological replicates were done for each sample and treatment condition.

f, Quantification of γH2AX foci in WT and *Capza3* KO cells at different doses of radiation treatment with or without treatment with AZD 7648 (DNA-PK inhibitor, 10 μM). Significance testing was performed with two-way ANOVA, three biological replicates were done for each sample and treatment condition.
For all experiments, WT cells were transduced with a lentiviral vector expressing a NTC gRNA.
* $p < 0.05$, ** $p < 0.01$, *** $p < 0.001$, **** $p < 0.0001$.

Supplementary Figure 6. Laser micro-irradiation induced DNA damage and staining with yH2AX to monitor dispersion of DNA damage foci.

a, Immunofluorescence imaging of γH2AX DNA damage foci 1 minute, 5 minutes, 10 minutes, 15 minutes, and 20 minutes following laser micro-irradiation in WT and *Capza3* KO cells.
b, Quantification in individual cells of the ratio of intensity of γH2AX staining in the region of laser induced DNA damage versus outside this region, 5 minutes, 10 minutes and 15 minutes after laser micro-irradiation. Significance testing was performed with two-way ANOVA, individual cell data from three biological replicates were pooled together for each sample.
For all experiments, WT cells were transduced with a lentiviral vector expressing a NTC gRNA.
* $p < 0.05$, ** $p < 0.01$, *** $p < 0.001$, **** $p < 0.0001$.

Supplementary Figure 7. Analysis of DNA damage foci and repair efficiency in SK-MEL-28, PANC1 and MDA-MB-231 *CAPG* and *CAPZA3* KO cell lines.

a, Quantification of γH2AX foci in WT, *CAPG* and *CAPZA3* KO SK-MEL-28 cell lines 24 hours after different doses of radiation treatment. Significance testing was performed with two-way ANOVA, three biological replicates were done for each sample and treatment condition.
b, Quantification of luciferase activity compared to WT cells 48 hours after transfection with HDR and NHEJ extrachromosomal reporters in WT, *CAPG* and *CAPZA3* KO SK-MEL-28 cell lines. Significance testing was performed with two-way ANOVA, four biological replicates were done for each sample.
c, Quantification of luciferase activity compared to WT cells 48 hours after transfection with NHEJ extrachromosomal reporter in WT, *CAPG* and *CAPZA3* KO PANC1 and MDA-MB-231 cell lines. Significance testing was performed with two-way ANOVA, at least three biological replicates were done for each sample.
d, QPCR of *CAPG* and *CAPZA3* expression in PANC1, MDA-MB-231 and SK-MEL-28 WT cells. Significance testing was performed with two-way ANOVA, four biological replicates were done for each sample.

e, QPCR analysis of *CAPG* (left) and *CAPZA3* (right) expression in WT, *CAPG* and *CAPZA3* KO in PANC1, MDA-MB-231 and SK-MEL-28 cell lines. Significance testing was performed with two-way ANOVA, four biological replicates were done for each sample.

f, CFA for WT, *CAPG* KO and *CAPZA3* KO PANC1 lines following treatment with different concentrations of Olaparib. The p value for WT vs *CAPG* KO is shown in blue and the p value for WT vs *CAPZA3* KO is shown in red. Significance testing was performed with two-way ANOVA, three biological replicates were done for each sample.

For all experiments, WT cells were passage-matched controls that underwent the procedure to generate KO cell lines (transfected with plasmid containing *CAPG* or *CAPZA3* targeting gRNA, sorted as single cells into a 96 well plate and expanded) but did not have a mutation at either the *CAPG* or *CAPZA3* locus. * $p < 0.05$, ** $p < 0.01$, *** $p < 0.001$, **** $p < 0.0001$.

Supplementary Figure 8. Generation and testing of an *AAVS1* Traffic Light Reporter (TLR) PANC1 cell line.

a, Colony PCR to identify PANC1 clones with targeted insertion of the traffic light reporter construct into the *AAVS1* locus.

b, Allele specific PCR of clones #1-2. PCR bands for nontargeted allele (WT: 500 bp) and targeted allele (300 bp) are shown. Both PANC1 clones showed insertion of the TLR construct into both *AAVS1* alleles.

c, Flow cytometry analysis of % GFP positive cells signaling HDR (left) and % RFP positive cells signaling NHEJ (right) after transfection of plasmid containing *Rosa26* targeting gRNA and a BFP reporter and gating on BFP positive cells.

d, Quantification of GFP positive cells signaling HDR 72 hours after transfection of *Rosa26* gRNA in PANC1 AAVS1 traffic light reporter (TLR) WT, *CAPG* and *CAPZA3* KO cell lines. Significance testing was performed with two-way ANOVA, three biological replicates were done for each sample, * $p < 0.05$, ** $p< 0.01$, *** $p < 0.001$, **** $p < 0.0001$.

Supplementary Figure 9. RNA sequencing analysis of B16F10 WT and *Capza3* gRNA 2 and *Capza3* gRNA 3 KO cells before and after 1 Gy radiation treatment.

a, Correlation between 2 independent replicates of RNA sequencing analysis. C21_1 refers to *Capza3* KO gRNA 2, clone 1 and replicate 1, C32_2 refers *Capza3* KO gRNA 3, clone 2 and replicate 2, etc. All samples before radiation treatment are shown on the left (12 samples in total) and all samples after radiation treatment are shown on the right (12 samples total).

b, PCA analysis of WT and *Capza3* KO mutants from 2 independent replicates of RNA sequencing analysis. All samples before radiation treatment are shown on the left (12 samples in total) and all samples after radiation treatment are shown on the right (12 samples in total).

c, Targets of *Irf9* transcription factor that show the greatest upregulation in *Capza3* KO compared to WT B16F10 cells, before radiation (left) and after radiation (right).

d, Quantification of STING (left) and IRF3 (right) for western blot shown in **Figure 5e**.

For RNA-Seq analyses, n = 2 replicates for each cell line (WT #1, WT #2, *Capza3* gRNA 2 KO #1, *Capza3* gRNA 2 KO #2, *Capza3* gRNA 3 KO #1, *Capza3* gRNA 3 KO #2) and each condition (no radiation or after 1 Gy radiation) were done, for 24 samples in total.

Supplementary Figure 10. Gating for analysis of cancer cells and EGFR CAR-T following co-culture

a, Gating strategy to quantify surviving cancer cells following co-culture with EGFR Car-T is shown. Cancer cells and lymphocytes were first gated based on forward and side scatter properties and then lymphocytes were identified using CD3-FITC staining.

b, Gating for flow analysis of CD69-BV421, CD25-PE, LAG3-PerCp5.5, PD1-APC and TIM3-PE-Cy7 in EGFR Car-T after co-culture with PANC1 and MDA-MB-231 *CAPG* and *CAPZA3* KOs are shown.

Supplementary Figure 11. Analysis of T cell activation and inhibitory markers after co-culture with PANC1 WT and *CEACAM1*, *CAPG* and *CAPZA3* single and double KO cells.

a, Flow cell analysis of *TIM3* expression in CAR-T cells after co-culture with PANC1 WT and *CEACAM1*, *CAPG* and *CAPZA3* single and double KO cells under 4 different treatment conditions (no treatment, 1 Gy RT before co-culture, anti-TIM3 antibody during co-culture, 1 Gy RT before co-culture and anti-TIM3 antibody during co-culture).

b, Flow cell analysis of *PD1* expression in CAR-T cells after co-culture with PANC1 WT and *CEACAM1*, *CAPG* and *CAPZA3* single and double KO cells under 4 different treatment conditions (no treatment, 1 Gy RT before co-culture, anti-TIM3 antibody during co-culture, 1 Gy RT before co-culture and anti-TIM3 antibody during co-culture).

c, Flow cell analysis of *LAG3* expression in CAR-T cells after co-culture with PANC1 WT and *CEACAM1*, *CAPG* and *CAPZA3* single and double KO cells under 4 different treatment conditions (no treatment, 1 Gy RT before co-culture, anti-TIM3 antibody during co-culture, 1 Gy RT before co-culture and anti-TIM3 antibody during co-culture).

d, Flow cell analysis of *CD69* expression in CAR-T cells after co-culture with PANC1 WT and *CEACAM1*, *CAPG* and *CAPZA3* single and double KO cells under 4 different treatment conditions (no treatment, 1 Gy RT before co-culture, anti-TIM3 antibody during co-culture, 1 Gy RT before co-culture and anti-TIM3 antibody during co-culture).

e, Flow cell analysis of *CD25* expression in CAR-T cells after co-culture with PANC1 WT and *CEACAM1*, *CAPG* and *CAPZA3* single and double KO cells under 4 different treatment conditions (no treatment, 1 Gy RT before co-culture, anti-TIM3 antibody with co-culture, 1 Gy RT before co-culture and anti-TIM3 antibody during co-culture).

For all experiments, WT cells were passage-matched controls that underwent the procedure to generate KO cell lines (transfected with plasmid containing *CAPG* or *CAPZA3* targeting gRNA, sorted as single cells into a 96 well plate and expanded) but did not have a mutation at either the *CAPG* or *CAPZA3* locus. For all experiments in this figure, significance testing was performed with two-way ANOVA, three biological replicates were done for each sample, * $p < 0.05$, ** $p < 0.01$, *** $p < 0.001$, **** $p < 0.0001$.

Supplementary Figure 12. Cell survival of MDA-MB-231 *CAPG* and *CAPZA3* KO cell lines compared to WT cells following treatment with radiation, anti-TIM3 antibody or anti-PD1 antibody and co-culture with EGFR CAR-T.

a, Expression of *PDL1* inhibitory ligand in WT, *CAPG* and *CAPZA3* KO MDA-MB-231 cell lines following radiation treatment. Representative flow plots are shown on the left and quantification is shown on the right. Significance testing was performed with one-way ANOVA, four biological replicates were done for each sample.

b, Cell survival of MDA-MB-231 *CAPG* and *CAPZA3* KO cell lines compared to WT cells following treatment with radiation, anti-TIM3 antibody and anti-PD1 antibody and co-culture with EGFR CAR-T. Significance testing was performed with two-way ANOVA, all comparisons were made to the no radiation or antibody treatment control. WT p-values: No RT or Ab vs. RT: 0.1076, No RT or Ab vs. RT + TIM3 Ab: 0.0588, No RT or Ab vs. RT + PD1 Ab: 0.0187. *CAPG* KO p-values: No RT or Ab vs. RT: 0.9808, No RT or Ab vs. RT + TIM3 Ab: 0.1766, No RT or Ab vs. RT + PD1 Ab: 0.3485. *CAPZA3* KO p-values: No RT or Ab vs. RT: 0.0354, No RT or Ab vs. RT + TIM3 Ab: 0.0058, No RT or Ab vs. RT + PD1 Ab: 0.9793. Three biological replicates were done for each sample and treatment condition.

For all experiments, WT cells were passage-matched controls that underwent the procedure to generate KO cell lines (transfected with plasmid containing *CAPG* or *CAPZA3* targeting gRNA, sorted as single

cells into a 96 well plate and expanded) but did not have a mutation at either the *CAPG* or *CAPZA3* locus. * $p < 0.05$, ** $p < 0.01$, *** $p < 0.001$, **** $p < 0.0001$.

Supplementary Figure 13. TCGA analysis of *CAPG* and *CAPZA3* expression among different cancer types, mutation count and correlation with overall survival.

a, Expression of *CAPG*, *CAPZA3* and other HDR associated genes among different cancer types.

b, Analysis of mutation count in patients with an isolated inactivating mutation in *CAPG* or *CAPZA3* or a mutation in a single HDR associated gene. P-values are shown for selected comparisons. Significance testing was performed with one-way ANOVA.

c, The number of cancers for which a HDR gene was prognostic for patient OS are shown. The number of cancers in which high expression of the HDR gene was associated with poorer OS are shown (HR > 1). The number of cancers in which high expression of the HDR gene was associated with improved OS (HR < 1) are shown.

d, The number of HDR genes that were prognostic for patient OS for each cancer type are shown. The number of HDR genes for which high expression was associated with poorer OS in each cancer are shown (HR > 1). The number of HDR genes for which high expression of the HDR gene was associated with improved OS in each cancer (HR < 1) are shown. Cancers in which high expression of an HDR gene was associated with improved survival (or low expression was associated with poorer survival) are highlighted in red.

Supplementary Figure 14. Correlation between immune cell infiltration and expression of *CAPG* and other known HDR associated genes.

a, Correlation between *CAPG* expression and infiltration of different immune cells within tumors.

b, Correlation between CD8 cytotoxic T cell tumor infiltration and expression of different HDR-associated genes.

c, Correlation between *CAPG* expression and infiltration of different immune cells within melanoma, breast cancer and pancreatic cancer cell types.

Pearson correlation coefficient and the corresponding p-values are shown.

Supplementary Figure 15. TCGA analysis of overall survival for cancer types based on expression of HDR-associated genes.

a, Survival curves for different cancer types based on high versus low expression of *CAPG*, *CAPZA3*, *BRCA1* and *BRCA2* are shown. Cancer types that had a significant difference in survival for high versus low expression of either *CAPG* or *CAPZA3* are highlighted. Significance testing between Kaplan Meier survival curves was done using the Log Rank test.

Supplementary Figure 16. TCGA analysis of overall curves for particular cancer types based on expression of HDR-associated genes.

a, Survival curves for different cancer types based on high versus low expression of *CAPG*, *CAPZA3*, *BRCA1* and *BRCA2* are shown. Cancer types that had a significant difference in survival for high versus low expression of either *CAPG* or *CAPZA3* are highlighted. Significance testing between Kaplan Meier survival curves was done using the Log Rank test.

Supplementary Tables

Table S1.

CRISPR KO lines used in this study listed in a table.

Table S2.

Oligo sequences used in this study listed in a table.

Table S3.

Key reagents used in this study listed in a table.

Supplementary Datasets

Dataset S1.

CRISPR screen processed data and analyses.

Dataset S2

RNA-seq processed data and analyses.

Dataset S3

Source data and statistics of non-NGS type data provided in an excel file.

Codes

Zip of codes for NGS data analysis

References:

1 Atun, R. *et al.* Expanding global access to radiotherapy. *Lancet Oncol* **16**, 1153-1186 (2015). https://doi.org:10.1016/S1470-2045(15)00222-3

2 Citrin, D. E. Recent Developments in Radiotherapy. *N Engl J Med* **377**, 2200-2201 (2017). https://doi.org:10.1056/NEJMc1713349

3 Jackson, S. P. & Bartek, J. The DNA-damage response in human biology and disease. *Nature* **461**, 1071-1078 (2009). https://doi.org:10.1038/nature08467

4 Sirbu, B. M. & Cortez, D. DNA damage response: three levels of DNA repair regulation. *Cold Spring Harb Perspect Biol* **5**, a012724 (2013). https://doi.org:10.1101/cshperspect.a012724

5 Symington, L. S. & Gautier, J. Double-strand break end resection and repair pathway choice. *Annu Rev Genet* **45**, 247-271 (2011). https://doi.org:10.1146/annurev-genet-110410-132435

6 Huang, R. X. & Zhou, P. K. DNA damage response signaling pathways and targets for radiotherapy sensitization in cancer. *Signal Transduct Target Ther* **5**, 60 (2020). https://doi.org:10.1038/s41392-020-0150-x

7 Liu, C., Yang, M., Zhang, D., Chen, M. & Zhu, D. Clinical cancer immunotherapy: Current progress and prospects. *Front Immunol* **13**, 961805 (2022). https://doi.org:10.3389/fimmu.2022.961805

8 Taefehshokr, S. *et al.* Cancer immunotherapy: Challenges and limitations. *Pathol Res Pract* **229**, 153723 (2022). https://doi.org:10.1016/j.prp.2021.153723

9 Apetoh, L. *et al.* Toll-like receptor 4-dependent contribution of the immune system to anticancer chemotherapy and radiotherapy. *Nat Med* **13**, 1050-1059 (2007). https://doi.org:10.1038/nm1622

10 Dovedi, S. J. *et al.* Systemic delivery of a TLR7 agonist in combination with radiation primes durable antitumor immune responses in mouse models of lymphoma. *Blood* **121**, 251-259 (2013). https://doi.org:10.1182/blood-2012-05-432393

11 Lee, Y. *et al.* Therapeutic effects of ablative radiation on local tumor require CD8+ T cells: changing strategies for cancer treatment. *Blood* **114**, 589-595 (2009). https://doi.org:10.1182/blood-2009-02-206870

12 Messmer, D. *et al.* High mobility group box protein 1: an endogenous signal for dendritic cell maturation and Th1 polarization. *J Immunol* **173**, 307-313 (2004). https://doi.org:10.4049/jimmunol.173.1.307

13 Matsumura, S. *et al.* Radiation-induced CXCL16 release by breast cancer cells attracts effector T cells. *J Immunol* **181**, 3099-3107 (2008). https://doi.org:10.4049/jimmunol.181.5.3099

14 Takeshima, T. *et al.* Local radiation therapy inhibits tumor growth through the generation of tumor-specific CTL: its potentiation by combination with Th1 cell therapy. *Cancer Res* **70**, 2697-2706 (2010). https://doi.org:10.1158/0008-5472.CAN-09-2982

15 Formenti, S. C. & Demaria, S. Combining radiotherapy and cancer immunotherapy: a paradigm shift. *J Natl Cancer Inst* **105**, 256-265 (2013). https://doi.org:10.1093/jnci/djs629

16 Ngwa, W. *et al.* Using immunotherapy to boost the abscopal effect. *Nat Rev Cancer* **18**, 313-322 (2018). https://doi.org:10.1038/nrc.2018.6

17 Takahashi, J. & Nagasawa, S. Immunostimulatory Effects of Radiotherapy for Local and Systemic Control of Melanoma: A Review. *Int J Mol Sci* **21** (2020). https://doi.org:10.3390/ijms21239324

18 Wu, M. *et al.* Systemic Immune Activation and Responses of Irradiation to Different Metastatic Sites Combined With Immunotherapy in Advanced Non-Small Cell Lung Cancer. *Front Immunol* **12**, 803247 (2021). https://doi.org:10.3389/fimmu.2021.803247

19 Doench, J. G. *et al.* Optimized sgRNA design to maximize activity and minimize off-target effects of CRISPR-Cas9. *Nat Biotechnol* **34**, 184-191 (2016). https://doi.org:10.1038/nbt.3437

20 Li, W. *et al.* MAGeCK enables robust identification of essential genes from genome-scale CRISPR/Cas9 knockout screens. *Genome Biol* **15**, 554 (2014). https://doi.org:10.1186/s13059-014-0554-4

21 Wilson, B. G. & Roberts, C. W. SWI/SNF nucleosome remodellers and cancer. *Nat Rev Cancer* **11**, 481-492 (2011). https://doi.org:10.1038/nrc3068

22 Kaeser, M. D., Aslanian, A., Dong, M. Q., Yates, J. R., 3rd & Emerson, B. M. BRD7, a novel PBAF-specific SWI/SNF subunit, is required for target gene activation and repression in embryonic stem cells. *J Biol Chem* **283**, 32254-32263 (2008). https://doi.org:10.1074/jbc.M806061200

23 Soniat, M. M., Myler, L. R., Kuo, H. C., Paull, T. T. & Finkelstein, I. J. RPA Phosphorylation Inhibits DNA Resection. *Mol Cell* **75**, 145-153 e145 (2019). https://doi.org:10.1016/j.molcel.2019.05.005

24 Mochan, T. A., Venere, M., DiTullio, R. A., Jr. & Halazonetis, T. D. 53BP1, an activator of ATM in response to DNA damage. *DNA Repair (Amst)* **3**, 945-952 (2004). https://doi.org:10.1016/j.dnarep.2004.03.017

25 Fernandez-Capetillo, O. *et al.* DNA damage-induced G2-M checkpoint activation by histone H2AX and 53BP1. *Nat Cell Biol* **4**, 993-997 (2002). https://doi.org:10.1038/ncb884

26 Sulkowski, P. L. *et al.* 2-Hydroxyglutarate produced by neomorphic IDH mutations suppresses homologous recombination and induces PARP inhibitor sensitivity. *Sci Transl Med* **9** (2017). https://doi.org:10.1126/scitranslmed.aal2463

27 Chu, V. T. *et al.* Increasing the efficiency of homology-directed repair for CRISPR-Cas9-induced precise gene editing in mammalian cells. *Nat Biotechnol* **33**, 543-548 (2015). https://doi.org:10.1038/nbt.3198

28 Chae, Y. K. *et al.* Genomic landscape of DNA repair genes in cancer. *Oncotarget* **7**, 23312-23321 (2016). https://doi.org:10.18632/oncotarget.8196

29 Aymard, F. *et al.* Genome-wide mapping of long-range contacts unveils clustering of DNA double-strand breaks at damaged active genes. *Nat Struct Mol Biol* **24**, 353-361 (2017). https://doi.org:10.1038/nsmb.3387

30 Caridi, C. P. *et al.* Nuclear F-actin and myosins drive relocalization of heterochromatic breaks. *Nature* **559**, 54-60 (2018). https://doi.org:10.1038/s41586-018-0242-8

31 Dion, V., Kalck, V., Horigome, C., Towbin, B. D. & Gasser, S. M. Increased mobility of double-strand breaks requires Mec1, Rad9 and the homologous recombination machinery. *Nat Cell Biol* **14**, 502-509 (2012). https://doi.org:10.1038/ncb2465

32 Mine-Hattab, J. & Rothstein, R. Increased chromosome mobility facilitates homology search during recombination. *Nat Cell Biol* **14**, 510-517 (2012). https://doi.org:10.1038/ncb2472

33 Neumaier, T. *et al.* Evidence for formation of DNA repair centers and dose-response nonlinearity in human cells. *Proc Natl Acad Sci U S A* **109**, 443-448 (2012). https://doi.org:10.1073/pnas.1117849108

34 Schrank, B. & Gautier, J. Assembling nuclear domains: Lessons from DNA repair. *J Cell Biol* **218**, 2444-2455 (2019). https://doi.org:10.1083/jcb.201904202

35 Schrank, B. R. *et al.* Nuclear ARP2/3 drives DNA break clustering for homology-directed repair. *Nature* **559**, 61-66 (2018). https://doi.org:10.1038/s41586-018-0237-5

36 Aten, J. A. *et al.* Dynamics of DNA double-strand breaks revealed by clustering of damaged chromosome domains. *Science* **303**, 92-95 (2004). https://doi.org:10.1126/science.1088845

37 Belin, B. J., Lee, T. & Mullins, R. D. DNA damage induces nuclear actin filament assembly by Formin -2 and Spire-(1/2) that promotes efficient DNA repair. [corrected]. *Elife* **4**, e07735 (2015). https://doi.org:10.7554/eLife.07735

38 Hurst, V., Shimada, K. & Gasser, S. M. Nuclear Actin and Actin-Binding Proteins in DNA Repair. *Trends Cell Biol* **29**, 462-476 (2019). https://doi.org:10.1016/j.tcb.2019.02.010

39 Virtanen, J. A. & Vartiainen, M. K. Diverse functions for different forms of nuclear actin. *Curr Opin Cell Biol* **46**, 33-38 (2017). https://doi.org:10.1016/j.ceb.2016.12.004

40 Baarlink, C. & Grosse, R. Formin' actin in the nucleus. *Nucleus* **5**, 15-20 (2014). https://doi.org:10.4161/nucl.28066

41 Buchbinder, D., Nugent, D. J. & Fillipovich, A. H. Wiskott-Aldrich syndrome: diagnosis, current management, and emerging treatments. *Appl Clin Genet* **7**, 55-66 (2014). https://doi.org:10.2147/TACG.S58444

42 Debaugnies, M. *et al.* RHOJ controls EMT-associated resistance to chemotherapy. *Nature* **616**, 168-175 (2023). https://doi.org:10.1038/s41586-023-05838-7

43 Le, D. T. *et al.* Mismatch repair deficiency predicts response of solid tumors to PD-1 blockade. *Science* **357**, 409-413 (2017). https://doi.org:10.1126/science.aan6733

44 Ma, J., Setton, J., Lee, N. Y., Riaz, N. & Powell, S. N. The therapeutic significance of mutational signatures from DNA repair deficiency in cancer. *Nat Commun* **9**, 3292 (2018). https://doi.org:10.1038/s41467-018-05228-y

45 Marabelle, A. *et al.* Efficacy of Pembrolizumab in Patients With Noncolorectal High Microsatellite Instability/Mismatch Repair-Deficient Cancer: Results From the Phase II KEYNOTE-158 Study. *J Clin Oncol* **38**, 1-10 (2020). https://doi.org:10.1200/JCO.19.02105

46 Matulonis, U. A. *et al.* Antitumor activity and safety of pembrolizumab in patients with advanced recurrent ovarian cancer: results from the phase II KEYNOTE-100 study. *Ann Oncol* **30**, 1080-1087 (2019). https://doi.org:10.1093/annonc/mdz135

47 Winer, E. P. *et al.* Pembrolizumab versus investigator-choice chemotherapy for metastatic triple-negative breast cancer (KEYNOTE-119): a randomised, open-label, phase 3 trial. *Lancet Oncol* **22**, 499-511 (2021). https://doi.org:10.1016/S1470-2045(20)30754-3

48 Liu, J. F. *et al.* Safety, clinical activity and biomarker assessments of atezolizumab from a Phase I study in advanced/recurrent ovarian and uterine cancers. *Gynecol Oncol* **154**, 314-322 (2019). https://doi.org:10.1016/j.ygyno.2019.05.021

49 Hamanishi, J. *et al.* Nivolumab Versus Gemcitabine or Pegylated Liposomal Doxorubicin for Patients With Platinum-Resistant Ovarian Cancer: Open-Label, Randomized Trial in Japan (NINJA). *J Clin Oncol* **39**, 3671-3681 (2021). https://doi.org:10.1200/JCO.21.00334

50 Sloan, E. A., Ring, K. L., Willis, B. C., Modesitt, S. C. & Mills, A. M. PD-L1 Expression in Mismatch Repair-deficient Endometrial Carcinomas, Including Lynch Syndrome-associated and MLH1 Promoter Hypermethylated Tumors. *Am J Surg Pathol* **41**, 326-333 (2017). https://doi.org:10.1097/PAS.0000000000000783

51 Permata, T. B. M. *et al.* Base excision repair regulates PD-L1 expression in cancer cells. *Oncogene* **38**, 4452-4466 (2019). https://doi.org:10.1038/s41388-019-0733-6

52 Parkes, E. E. *et al.* Activation of STING-Dependent Innate Immune Signaling By S-Phase-Specific DNA Damage in Breast Cancer. *J Natl Cancer Inst* **109** (2017). https://doi.org:10.1093/jnci/djw199

53 Mills, A. M. *et al.* The Relationship Between Mismatch Repair Deficiency and PD-L1 Expression in Breast Carcinoma. *Am J Surg Pathol* **42**, 183-191 (2018). https://doi.org:10.1097/PAS.0000000000000949

54 Howitt, B. E. *et al.* Association of Polymerase e-Mutated and Microsatellite-Instable Endometrial Cancers With Neoantigen Load, Number of Tumor-Infiltrating Lymphocytes, and Expression of PD-1 and PD-L1. *JAMA Oncol* **1**, 1319-1323 (2015). https://doi.org:10.1001/jamaoncol.2015.2151

55 Nagaishi, T., Iijima, H., Nakajima, A., Chen, D. & Blumberg, R. S. Role of CEACAM1 as a regulator of T cells. *Ann N Y Acad Sci* **1072**, 155-175 (2006). https://doi.org:10.1196/annals.1326.004

56 Kim, W. M., Huang, Y. H., Gandhi, A. & Blumberg, R. S. CEACAM1 structure and function in immunity and its therapeutic implications. *Semin Immunol* **42**, 101296 (2019). https://doi.org:10.1016/j.smim.2019.101296

57 Huang, Y. H. *et al.* CEACAM1 regulates TIM-3-mediated tolerance and exhaustion. *Nature* **517**, 386-390 (2015). https://doi.org:10.1038/nature13848

58 Dankner, M., Gray-Owen, S. D., Huang, Y. H., Blumberg, R. S. & Beauchemin, N. CEACAM1 as a multi-purpose target for cancer immunotherapy. *Oncoimmunology* **6**, e1328336 (2017). https://doi.org:10.1080/2162402X.2017.1328336

59 Theelen, W. *et al.* Effect of Pembrolizumab After Stereotactic Body Radiotherapy vs Pembrolizumab Alone on Tumor Response in Patients With Advanced Non-Small Cell Lung Cancer: Results of the PEMBRO-RT Phase 2 Randomized Clinical Trial. *JAMA Oncol* **5**, 1276-1282 (2019). https://doi.org:10.1001/jamaoncol.2019.1478

60 Rajeev-Kumar, G. & Pitroda, S. P. Synergizing radiotherapy and immunotherapy: Current challenges and strategies for optimization. *Neoplasia* **36**, 100867 (2023). https://doi.org:10.1016/j.neo.2022.100867

61 McBride, S. *et al.* Randomized Phase II Trial of Nivolumab With Stereotactic Body Radiotherapy Versus Nivolumab Alone in Metastatic Head and Neck Squamous Cell Carcinoma. *J Clin Oncol* **39**, 30-37 (2021). https://doi.org:10.1200/JCO.20.00290

62 Lee, N. Y. *et al.* Avelumab plus standard-of-care chemoradiotherapy versus chemoradiotherapy alone in patients with locally advanced squamous cell carcinoma of the head and neck: a randomised, double-blind, placebo-controlled, multicentre, phase 3 trial. *Lancet Oncol* **22**, 450-462 (2021). https://doi.org:10.1016/S1470-2045(20)30737-3

63 Zhao, M. *et al.* Rapid in vitro generation of bona fide exhausted CD8+ T cells is accompanied by Tcf7 promotor methylation. *PLoS Pathog* **16**, e1008555 (2020). https://doi.org:10.1371/journal.ppat.1008555

64 Martin, M. Cutadapt removes adapter sequences from high-throughput sequencing reads. . *Embnet.journal* **17** (2011).

65 Langmead, B., Trapnell, C., Pop, M. & Salzberg, S. L. Ultrafast and memory-efficient alignment of short DNA sequences to the human genome. *Genome Biol* **10**, R25 (2009). https://doi.org:10.1186/gb-2009-10-3-r25

66 Brown, J., Pirrung, M. & McCue, L. A. FQC Dashboard: integrates FastQC results into a web-based, interactive, and extensible FASTQ quality control tool. *Bioinformatics* **33**, 3137-3139 (2017). https://doi.org:10.1093/bioinformatics/btx373

67 Clement, K. *et al.* CRISPResso2 provides accurate and rapid genome editing sequence analysis. *Nat Biotechnol* **37**, 224-226 (2019). https://doi.org:10.1038/s41587-019-0032-3

68 Dobin, A. *et al.* STAR: ultrafast universal RNA-seq aligner. *Bioinformatics* **29**, 15-21 (2013). https://doi.org:10.1093/bioinformatics/bts635

69 Li, B. & Dewey, C. N. RSEM: accurate transcript quantification from RNA-Seq data with or without a reference genome. *BMC Bioinformatics* **12**, 323 (2011). https://doi.org:10.1186/1471-2105-12-323

70 Lun, A. T., Chen, Y. & Smyth, G. K. It's DE-licious: A Recipe for Differential Expression Analyses of RNA-seq Experiments Using Quasi-Likelihood Methods in edgeR. *Methods Mol Biol* **1418**, 391-416 (2016). https://doi.org:10.1007/978-1-4939-3578-9_19

71 Li, X., Cooper, N. G. F., O'Toole, T. E. & Rouchka, E. C. Choice of library size normalization and statistical methods for differential gene expression analysis in balanced two-group comparisons for RNA-seq studies. *BMC Genomics* **21**, 75 (2020). https://doi.org:10.1186/s12864-020-6502-7

72 Badia, I. M. P. *et al.* decoupleR: ensemble of computational methods to infer biological activities from omics data. *Bioinform Adv* **2**, vbac016 (2022). https://doi.org:10.1093/bioadv/vbac016

73 Garcia-Alonso, L., Holland, C. H., Ibrahim, M. M., Turei, D. & Saez-Rodriguez, J. Benchmark and integration of resources for the estimation of human transcription factor activities. *Genome Res* **29**, 1363-1375 (2019). https://doi.org:10.1101/gr.240663.118

74 Goldman, M. J. *et al.* Visualizing and interpreting cancer genomics data via the Xena platform. *Nat Biotechnol* **38**, 675-678 (2020). https://doi.org:10.1038/s41587-020-0546-8

75 Becht, E. *et al.* Estimating the population abundance of tissue-infiltrating immune and stromal cell populations using gene expression. *Genome Biol* **17**, 218 (2016). https://doi.org:10.1186/s13059-016-1070-5

76 Yu, G., Wang, L. G., Han, Y. & He, Q. Y. clusterProfiler: an R package for comparing biological themes among gene clusters. *OMICS* **16**, 284-287 (2012). https://doi.org:10.1089/omi.2011.0118

Figure 1

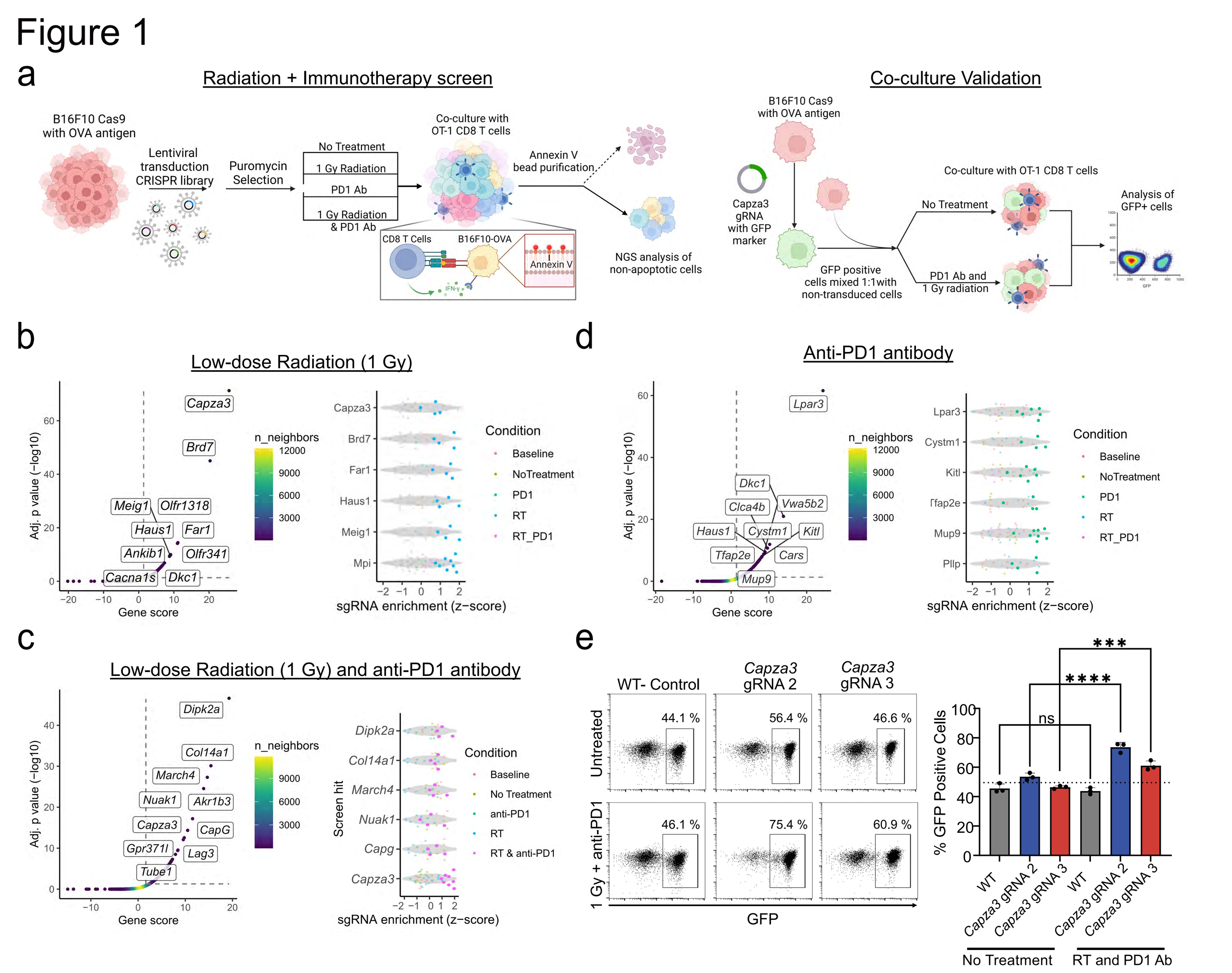

Figure 2

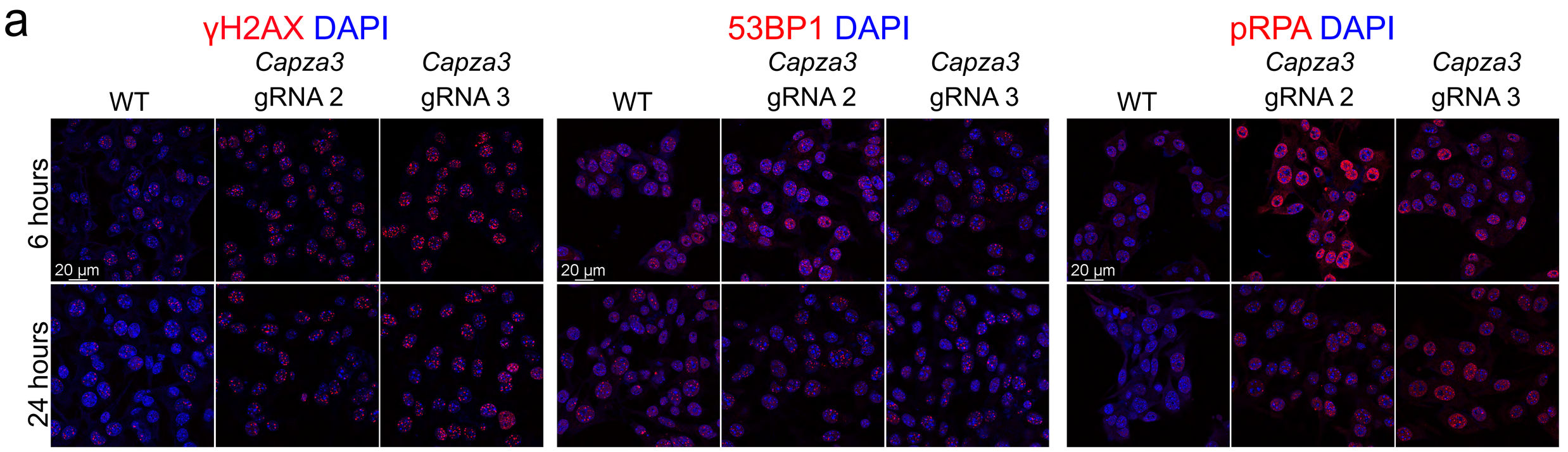

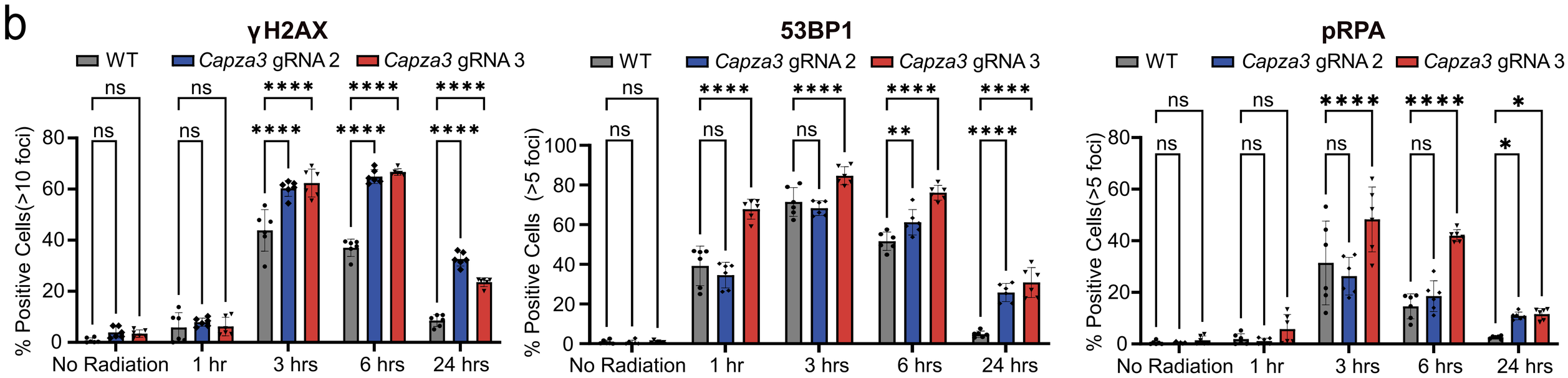

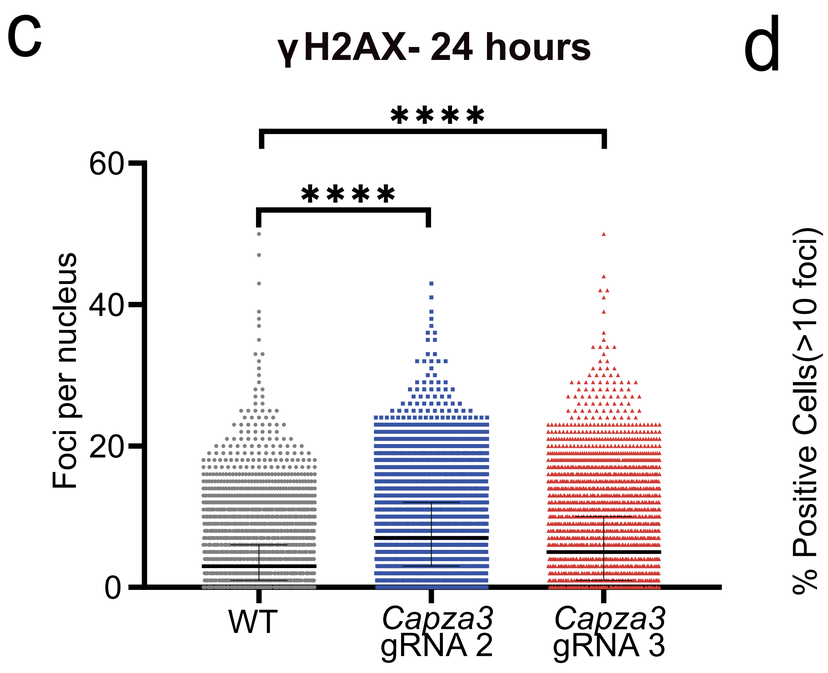

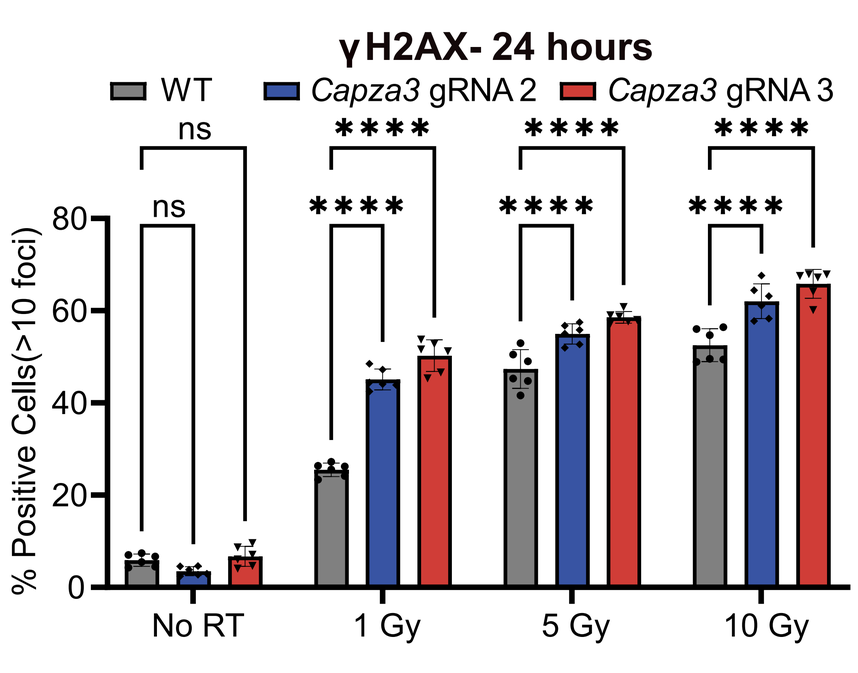

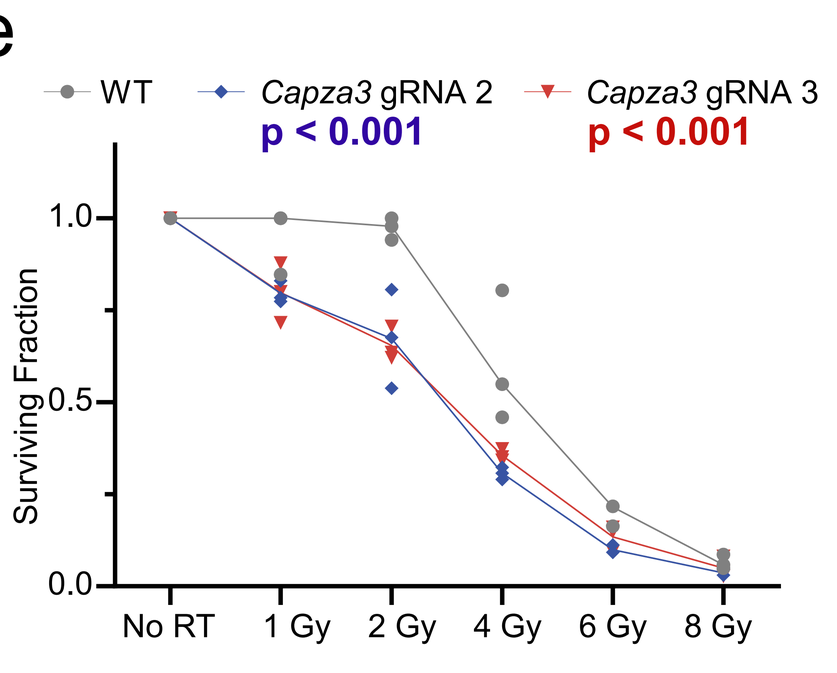

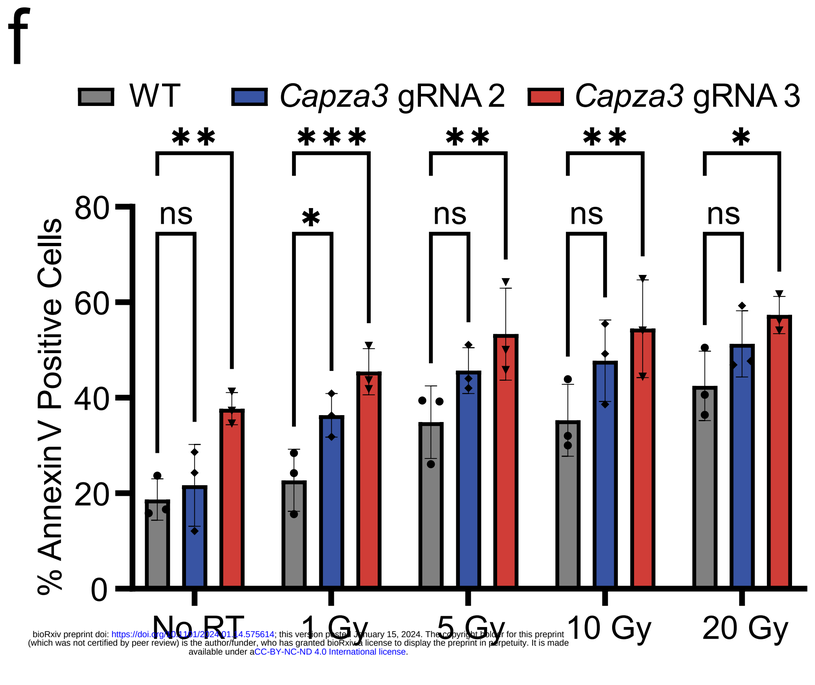

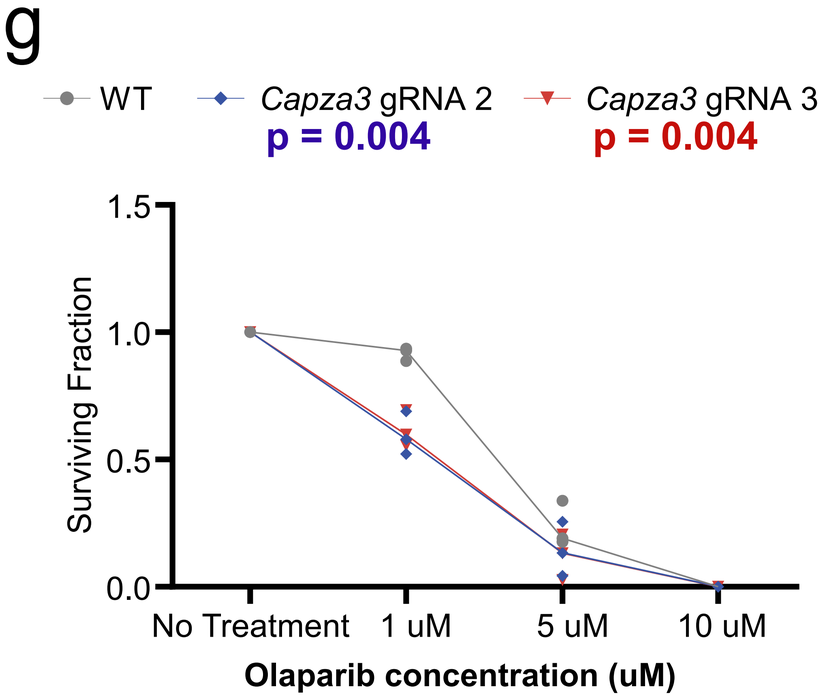

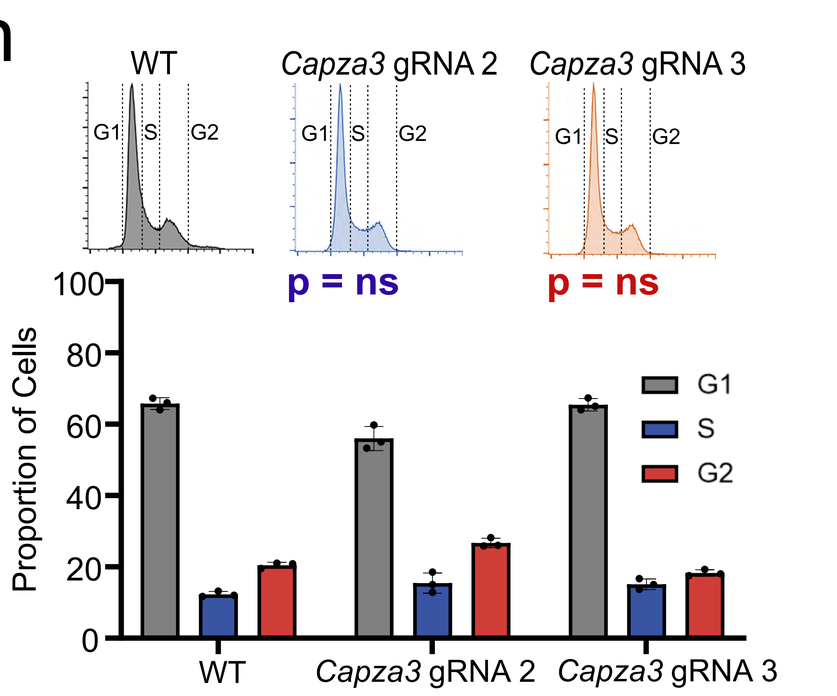

Figure 3

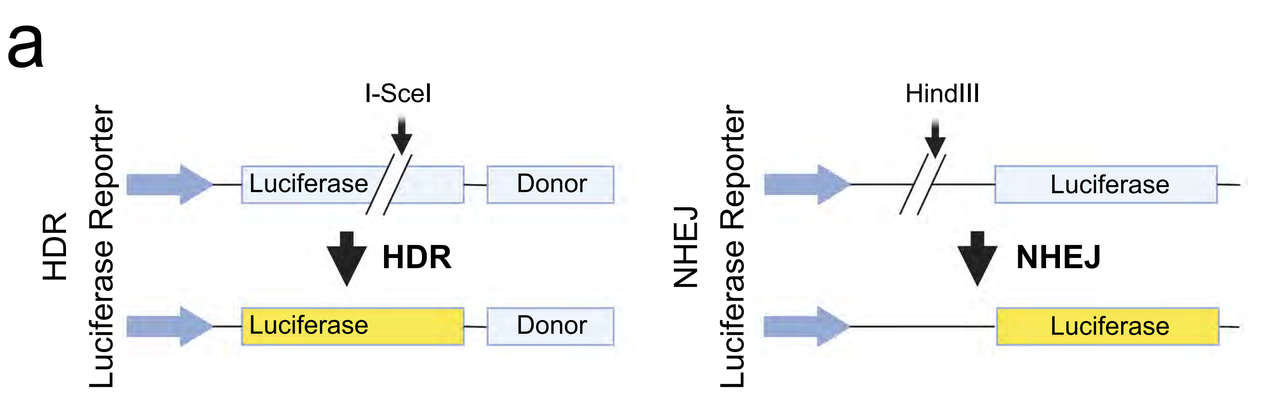

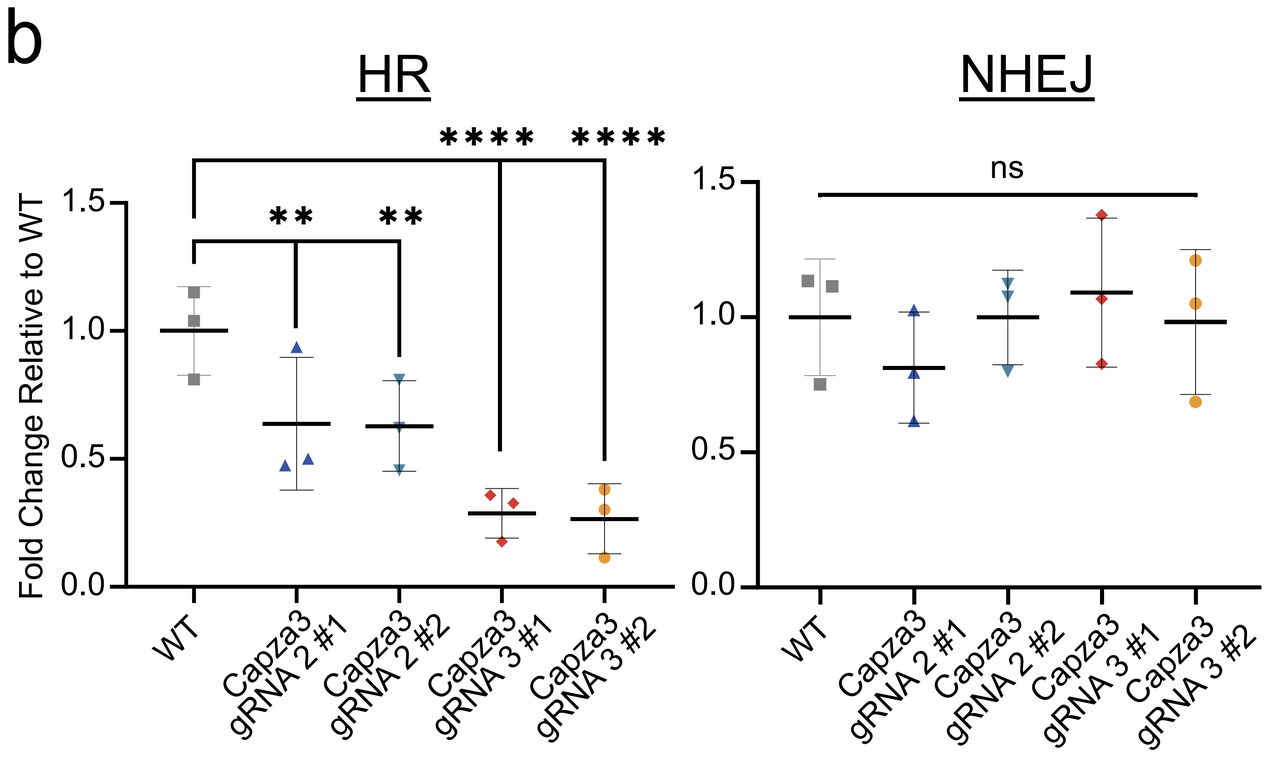

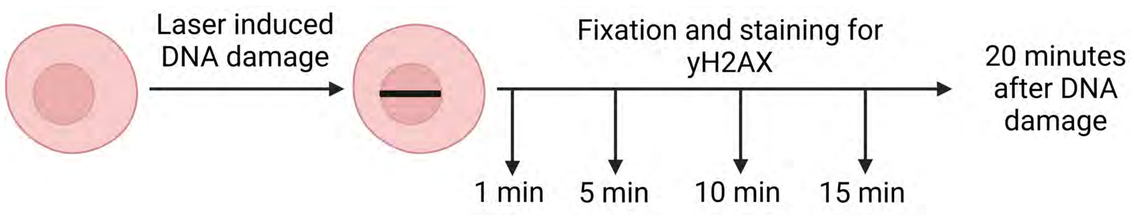

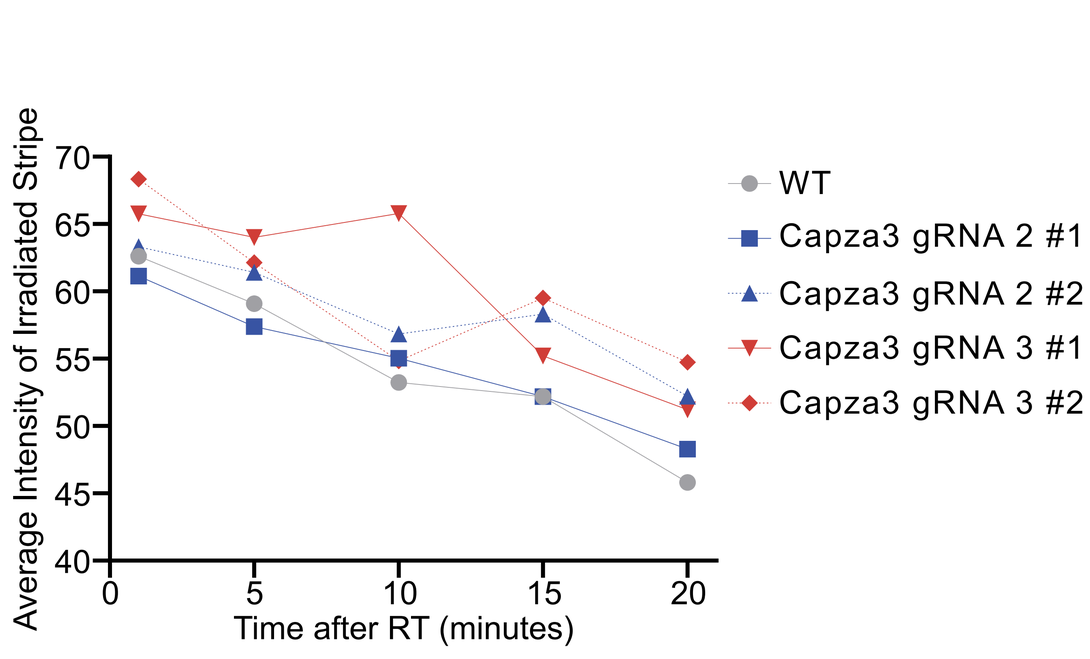

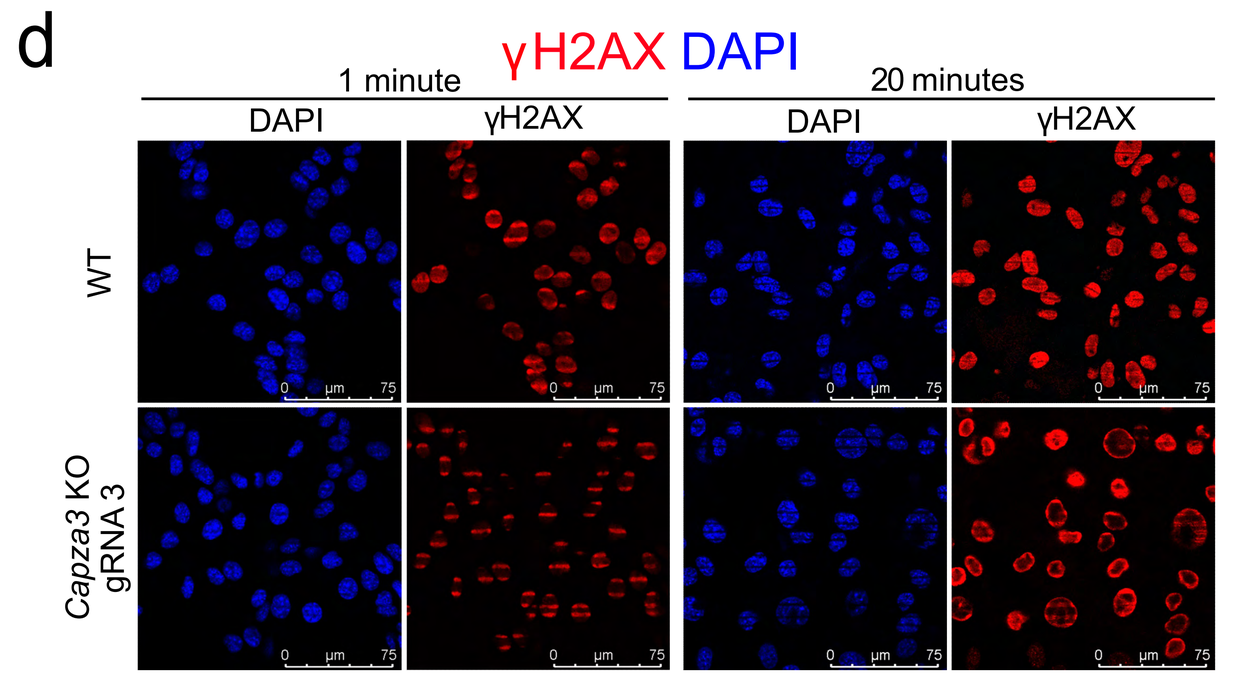

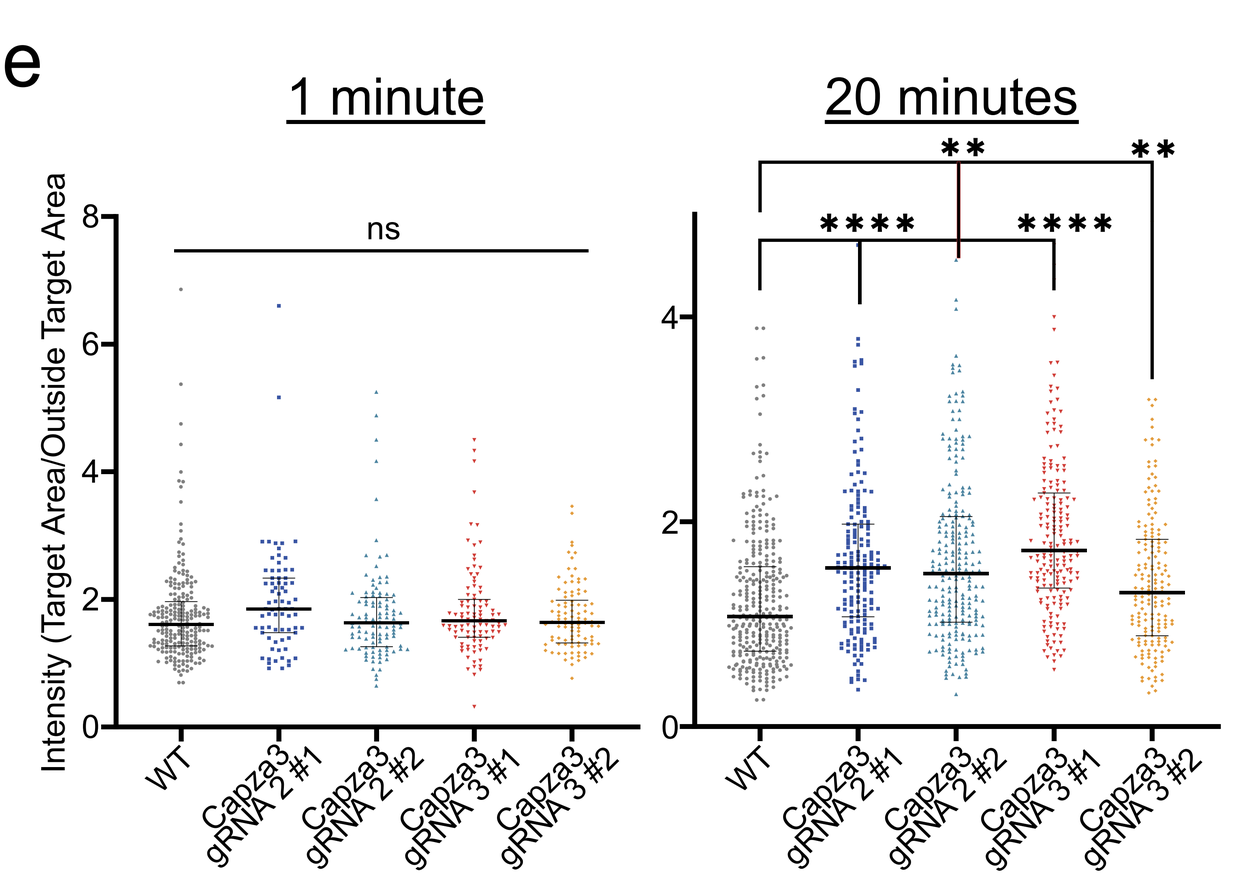

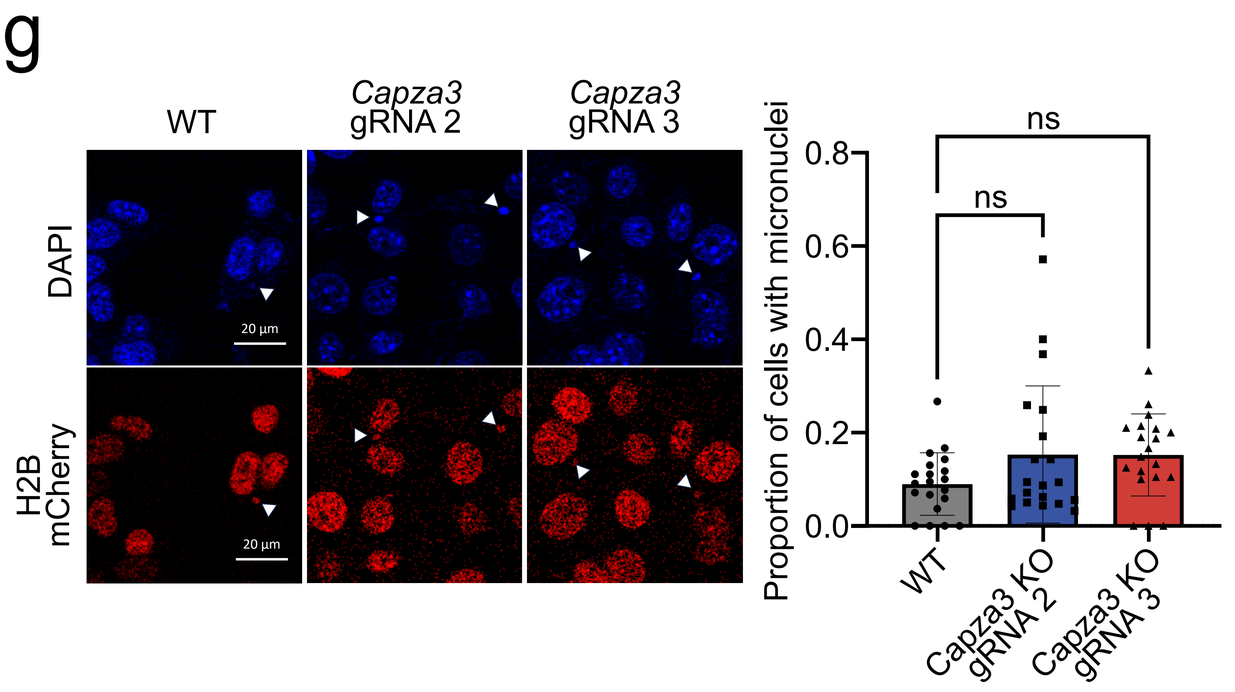

Figure 4

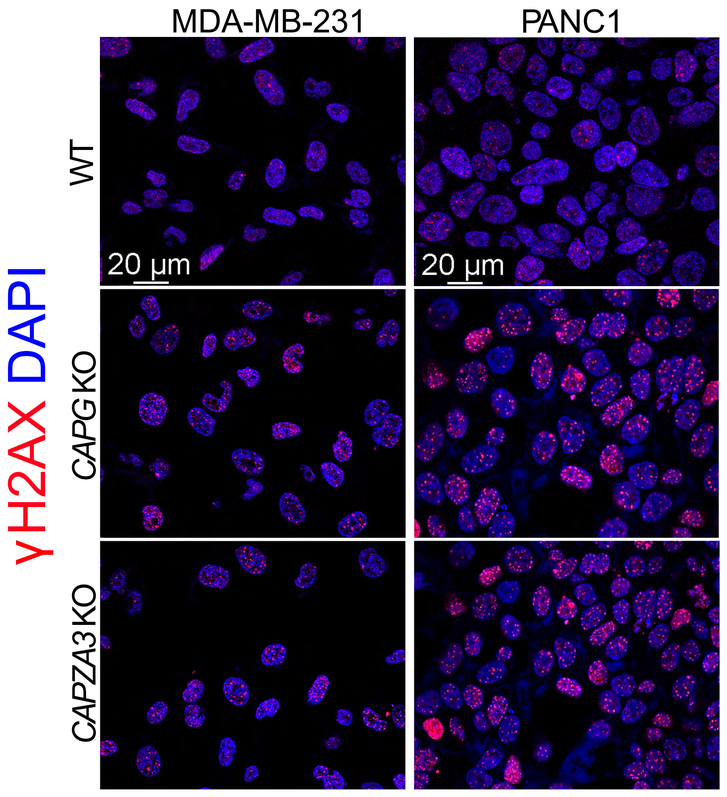

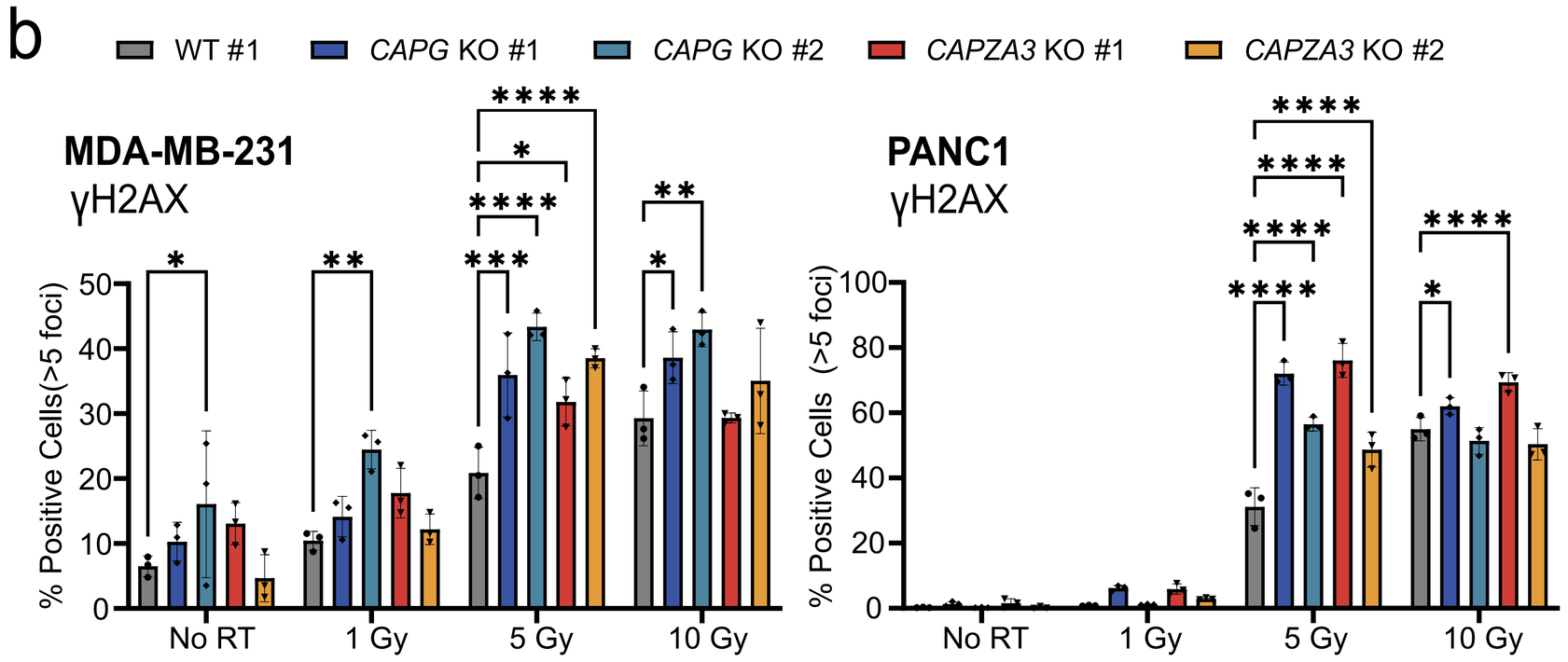

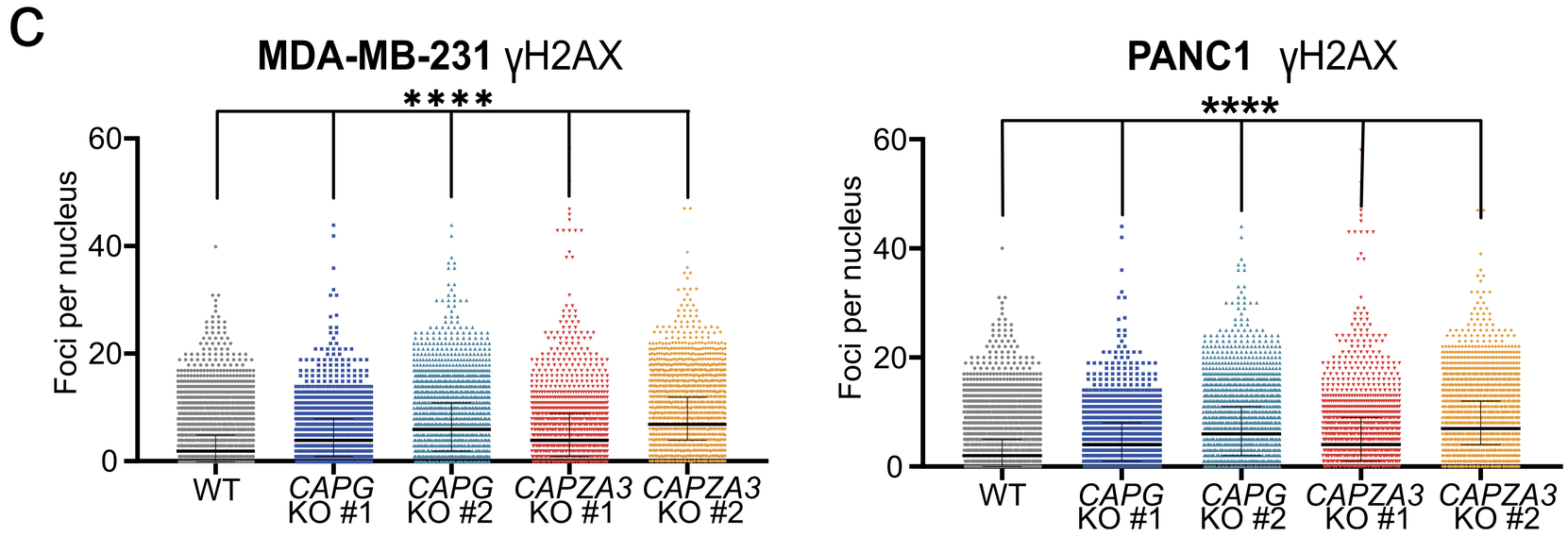

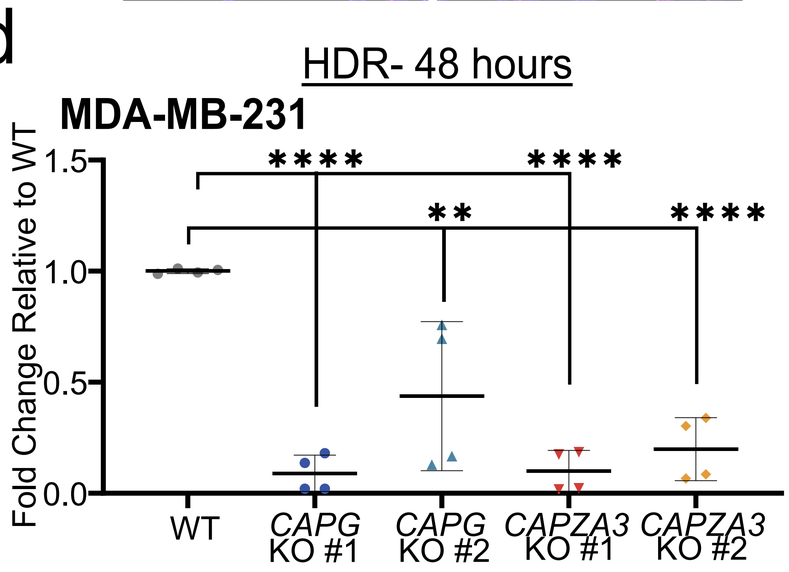

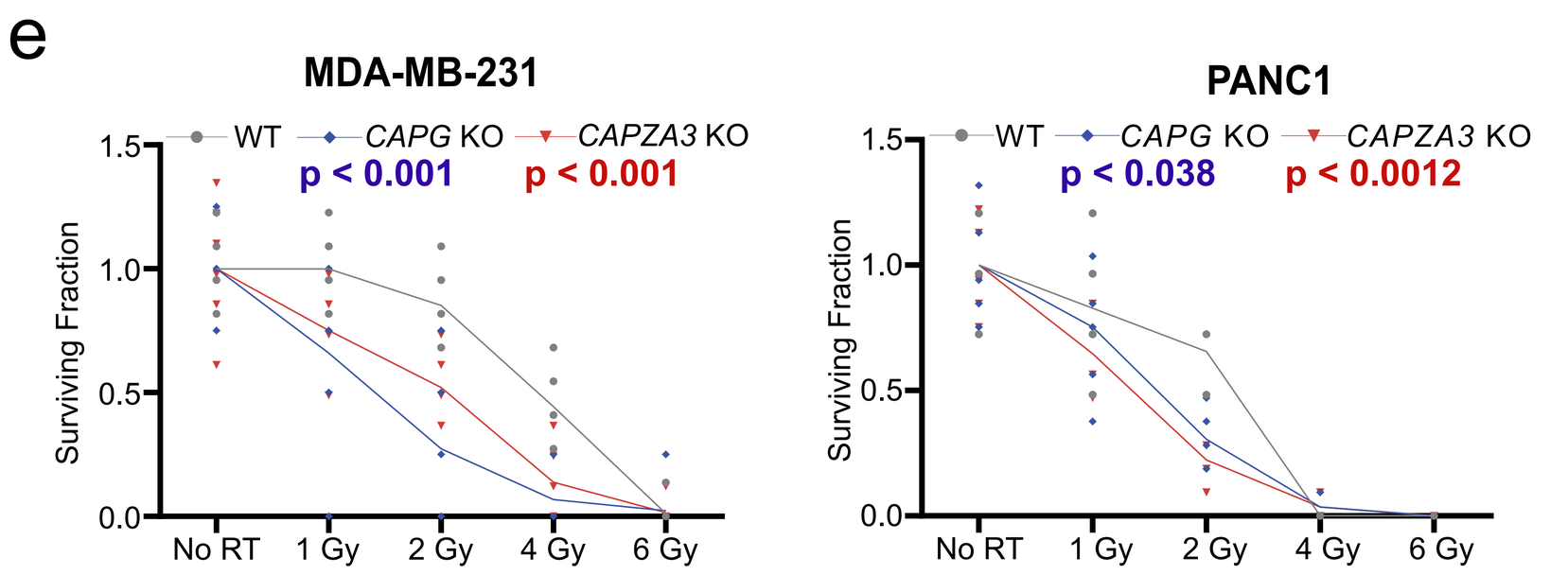

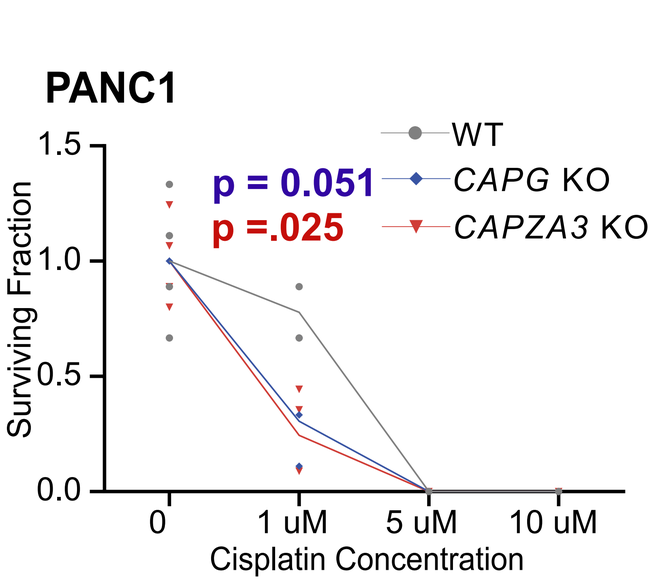

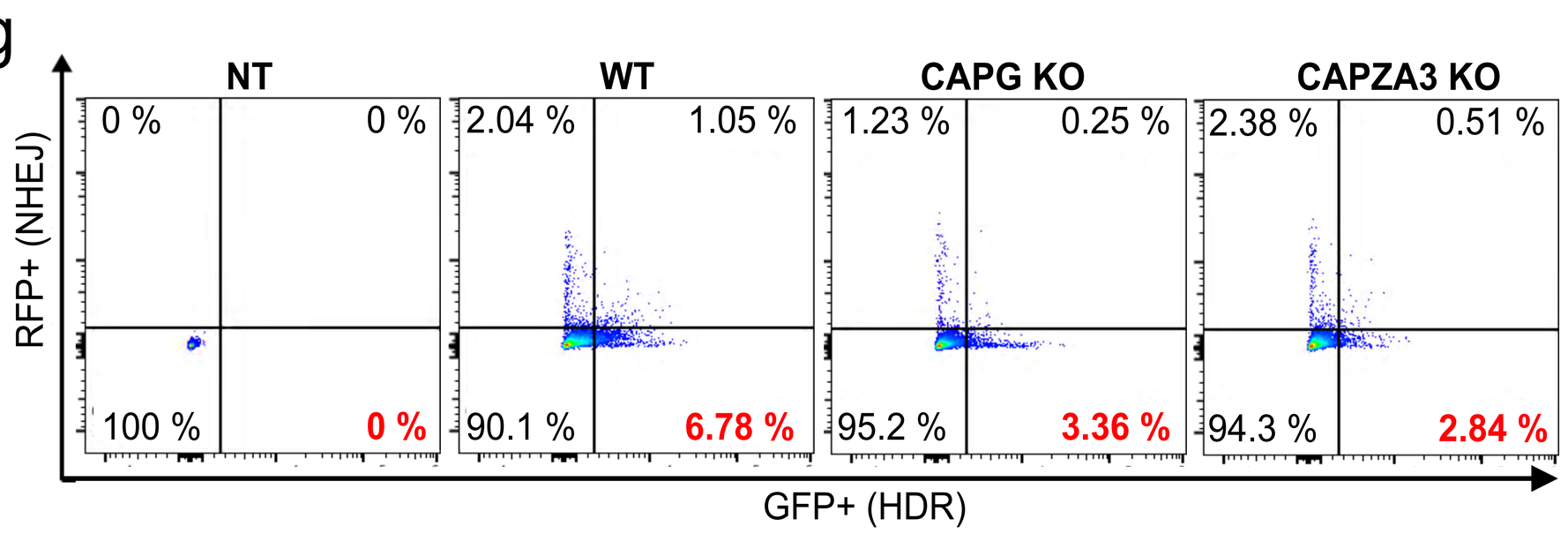

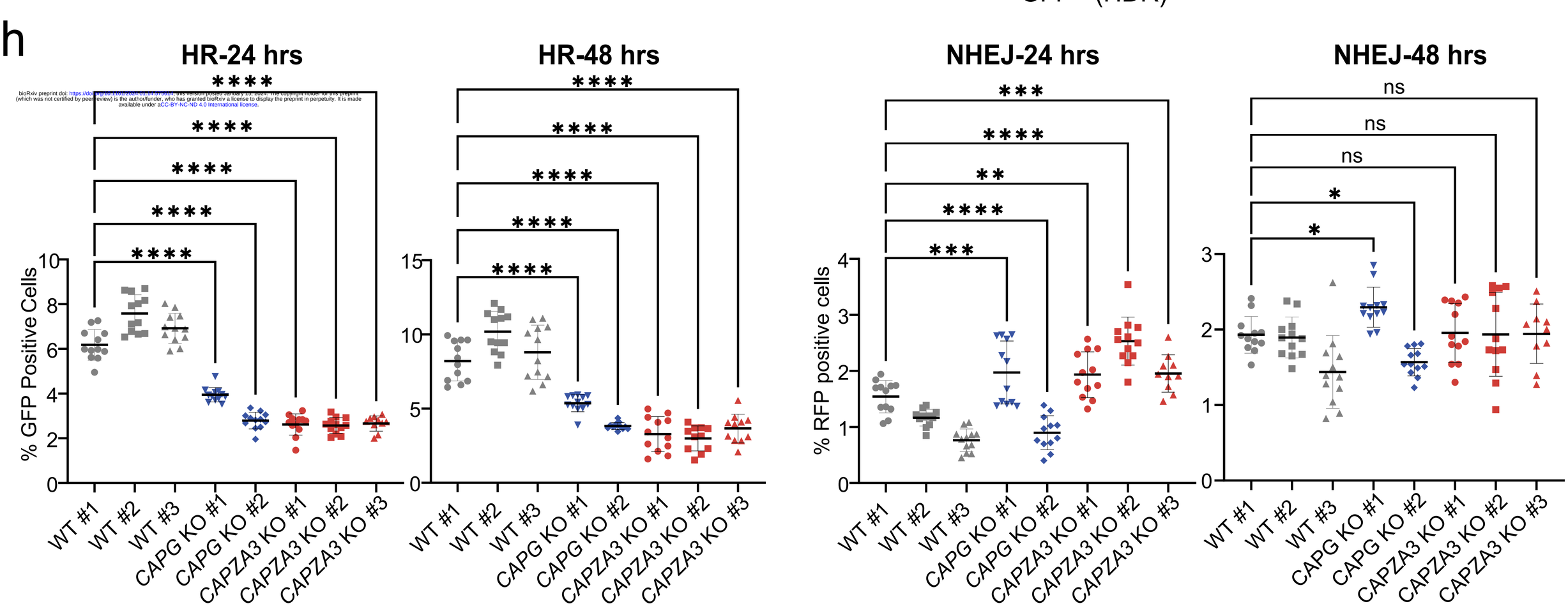

Figure 5

Figure 6

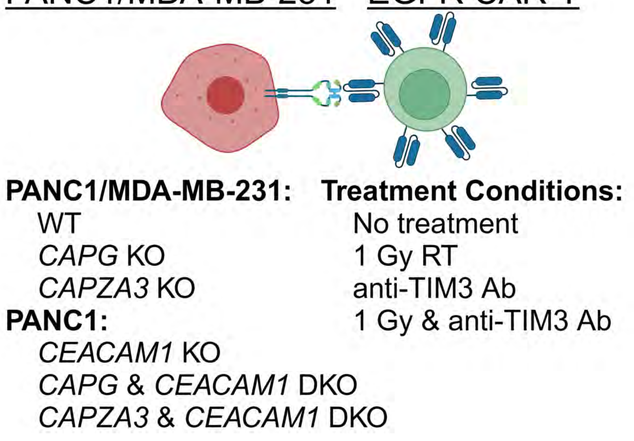

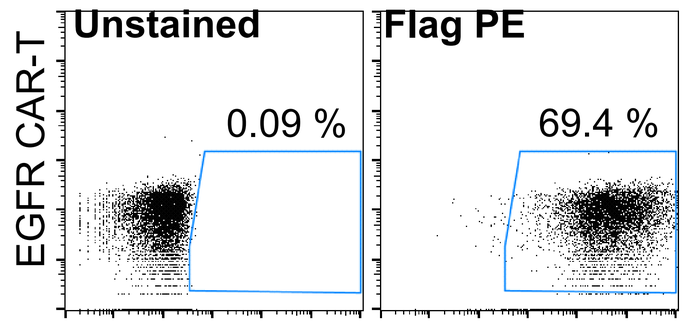

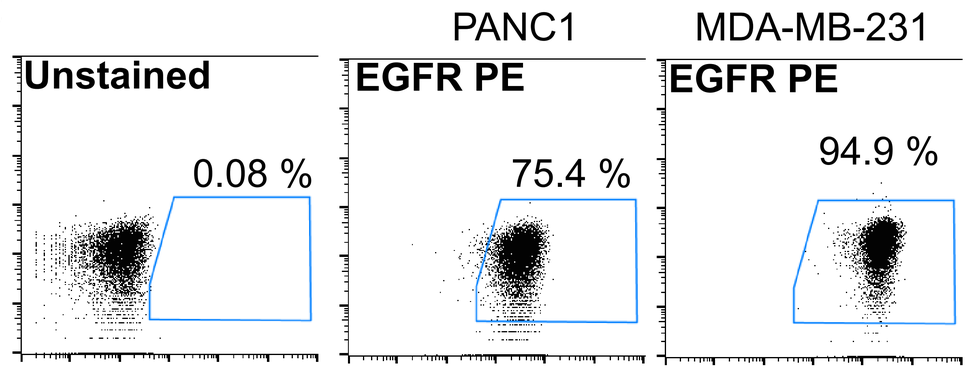

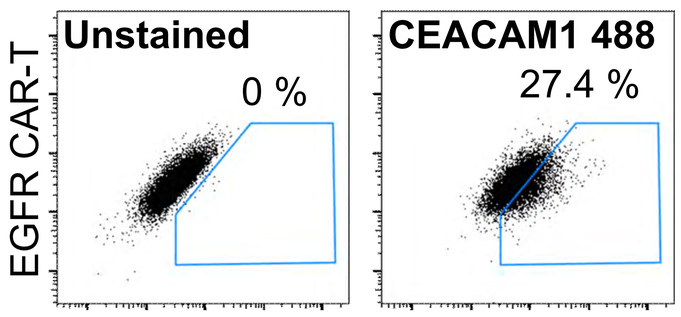

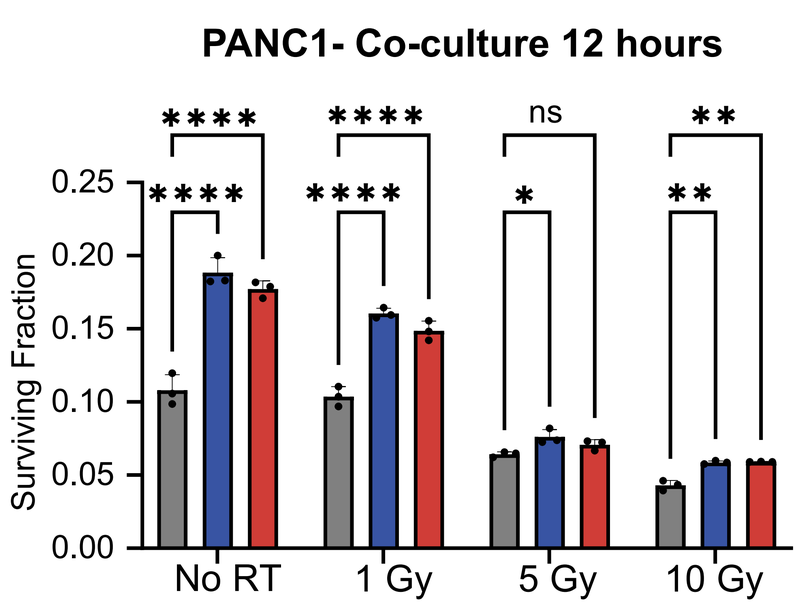

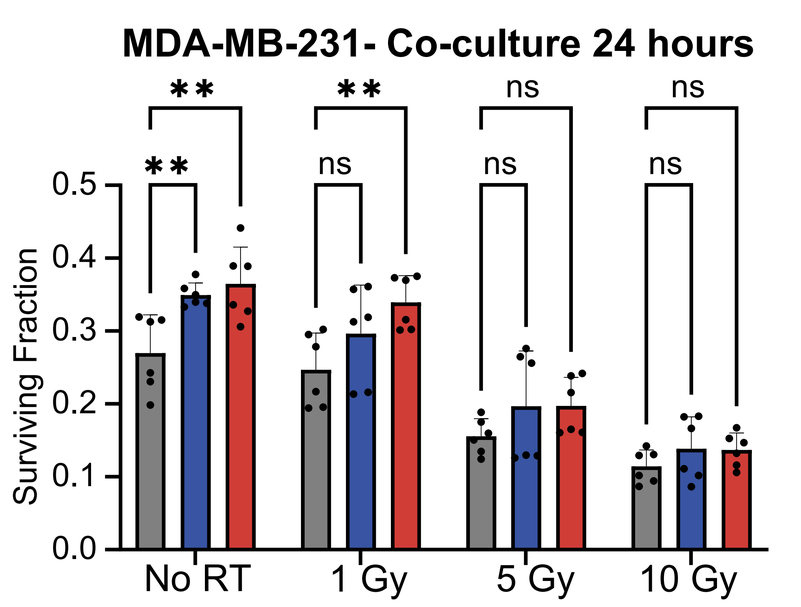

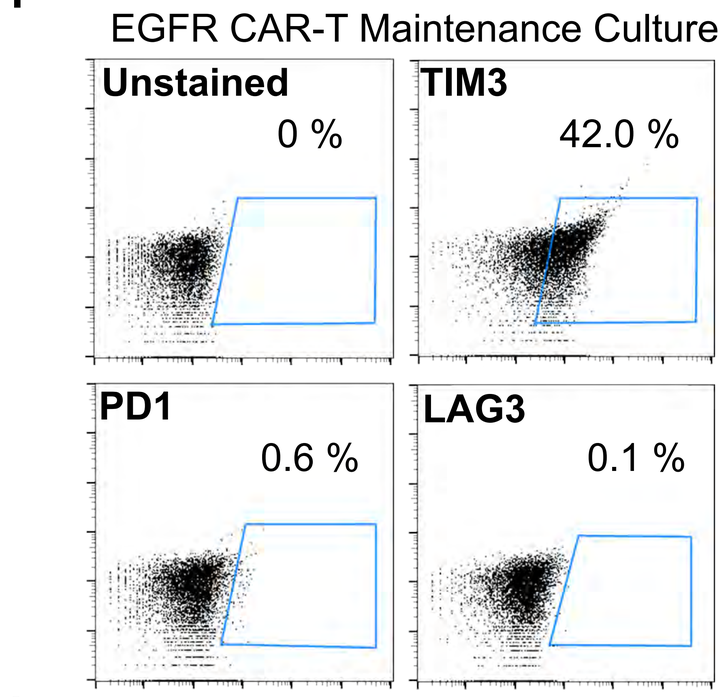

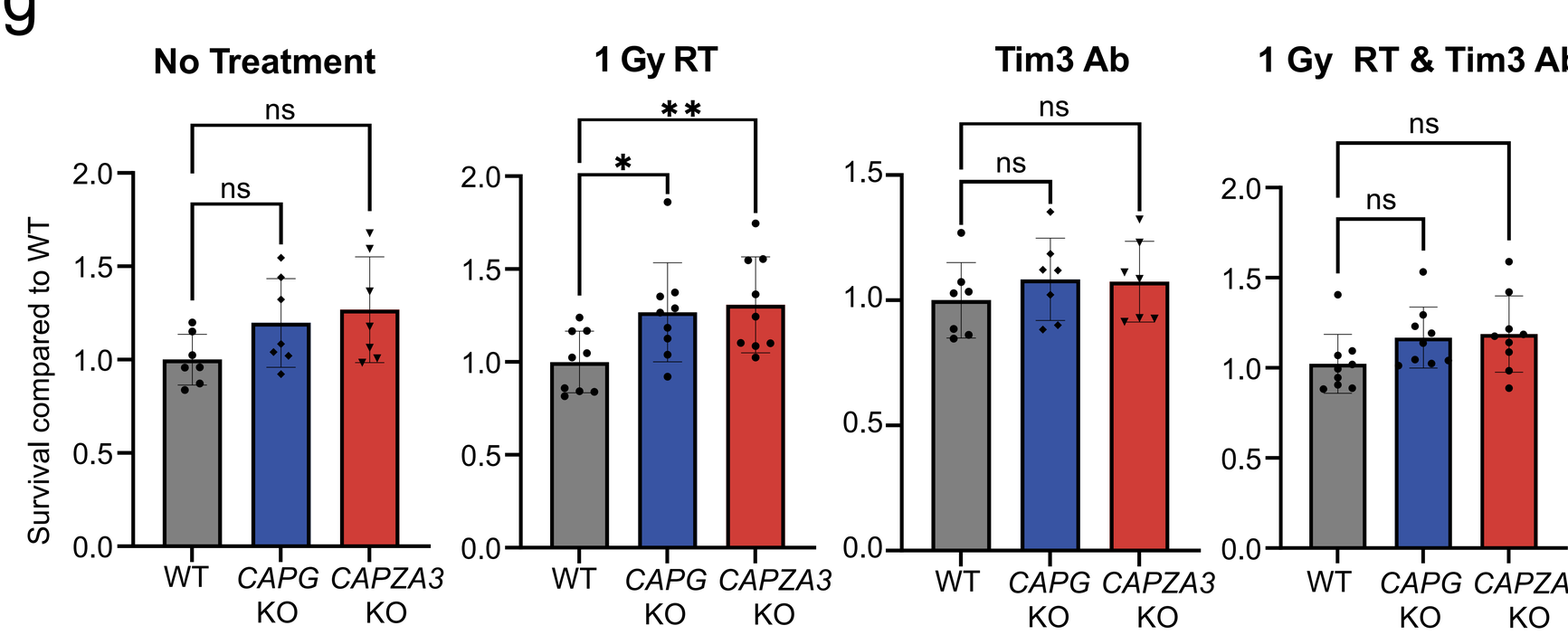

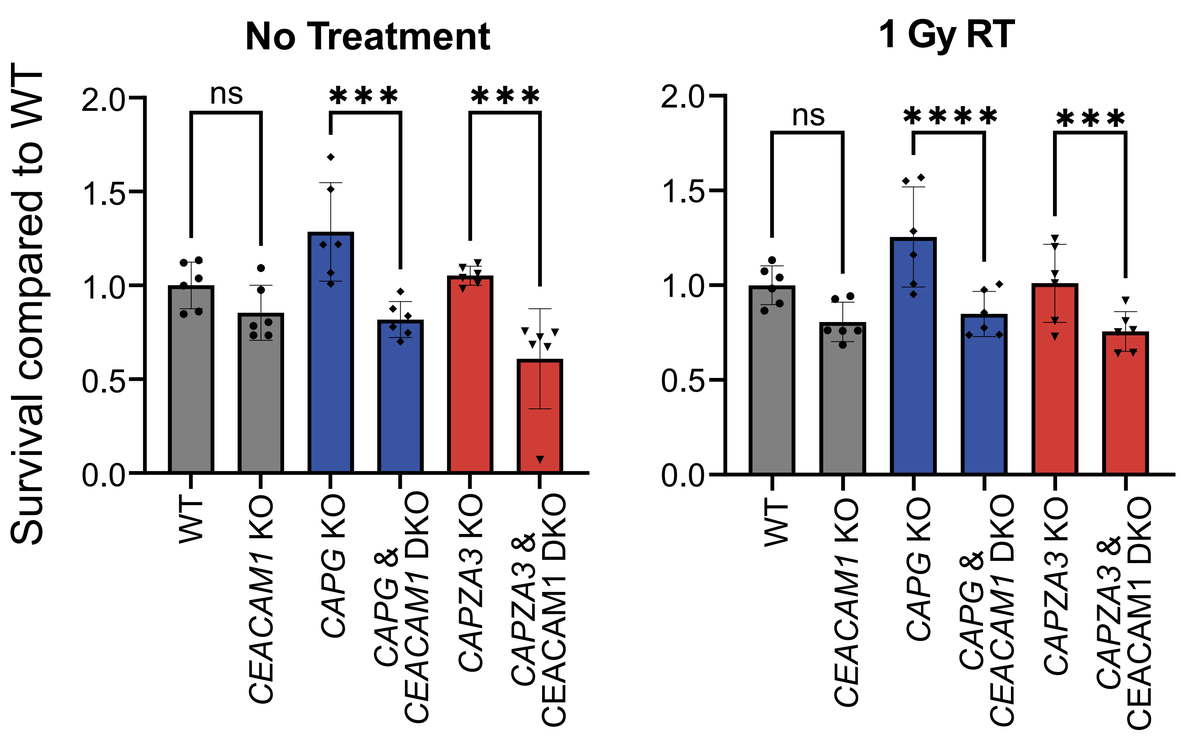

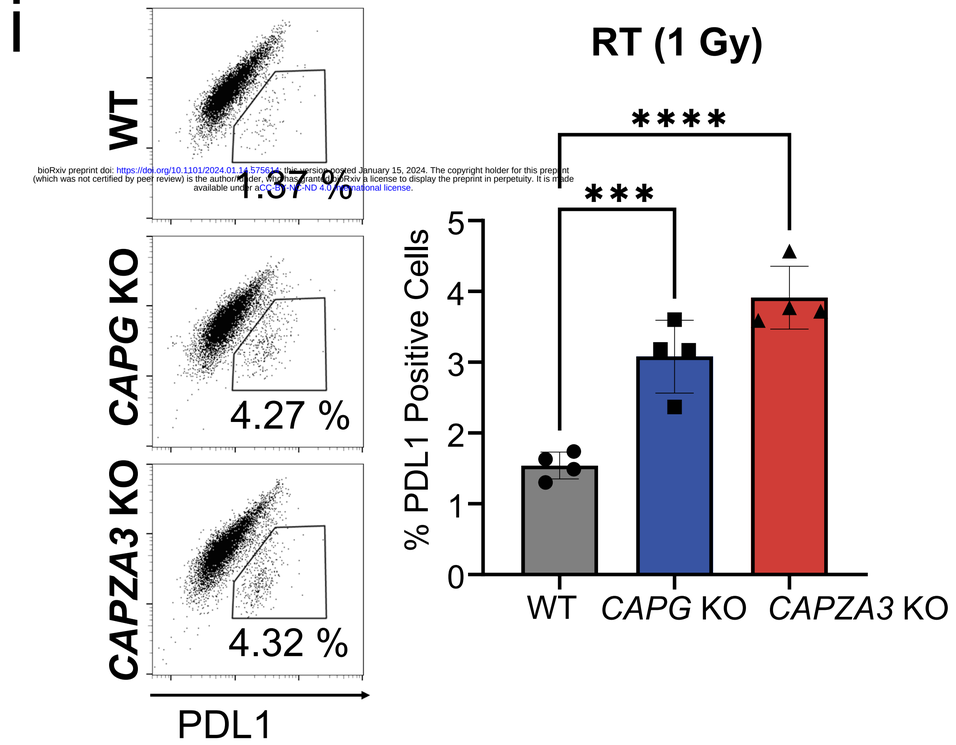

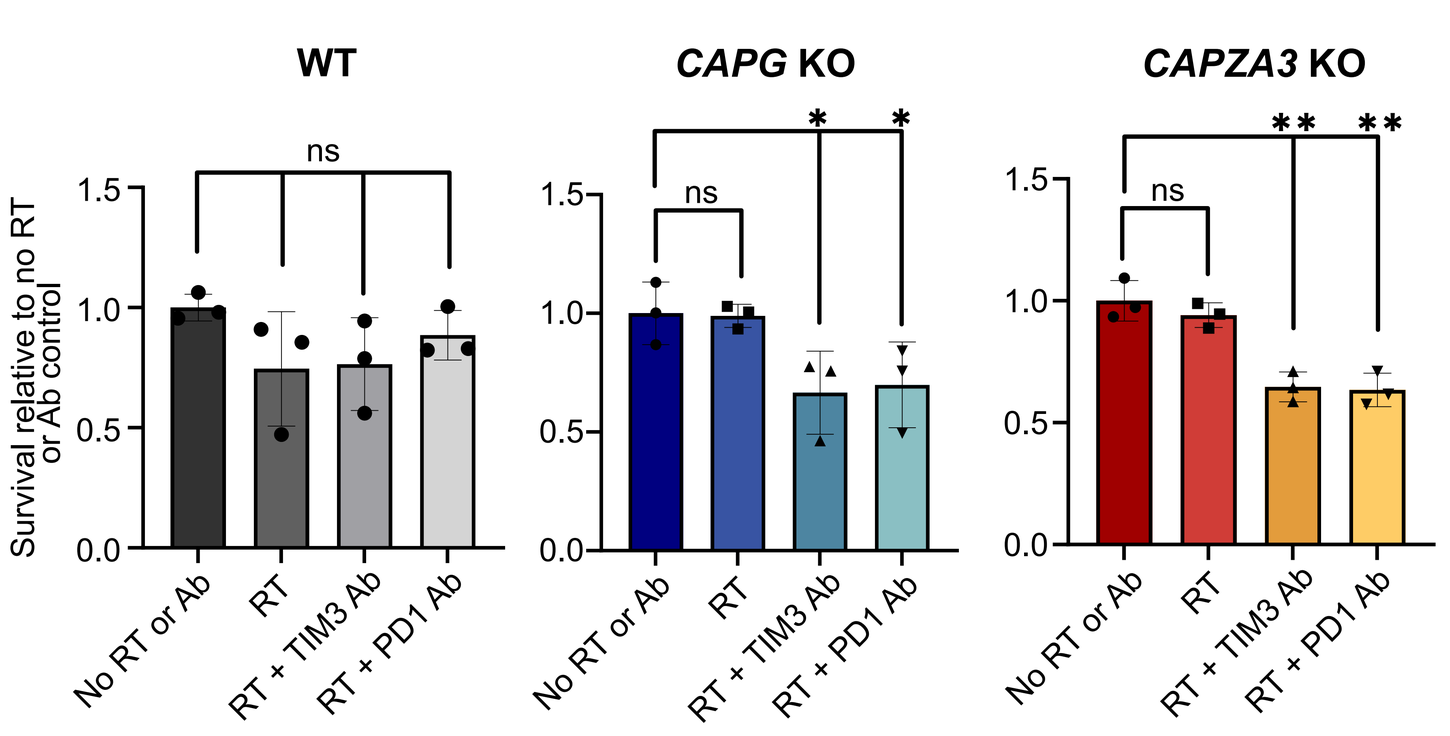

Figure 7

a

Gene	Odd ratio	P-value
APEX1	7.780	0.00073127
ATM	6.022	2.25E-13
BRCA1	7.109	2.87E-11
BRCA2	8.730	3.43E-19
BRIP1	10.319	9.64E-15
H2AFX	8.556	0.00179157
LIG1	7.100	7.42E-08
MDC1	8.138	3.19E-13
MRE11A	10.839	1.37E-10
NBN	10.348	1.82E-11
RAD50	10.678	1.77E-14
RAD51	9.411	8.45E-05
RAD52	6.503	0.0005411
RPA1	7.635	7.83E-06
RPA2	3.996	0.04461951
RPA3	7.764	0.00868572
TP53BP1	9.384	2.07E-16

b

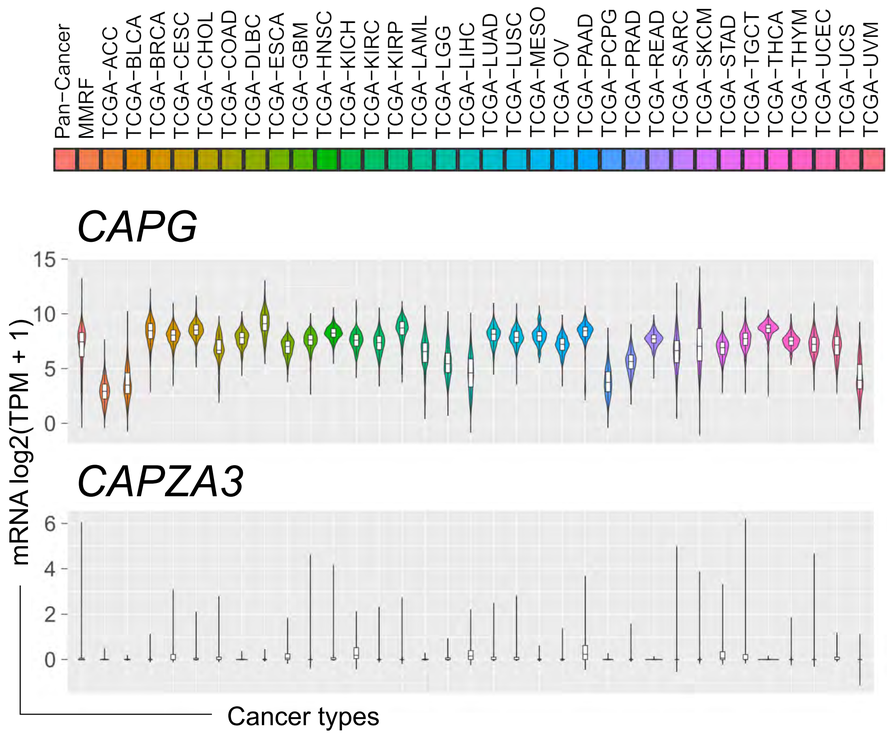

c

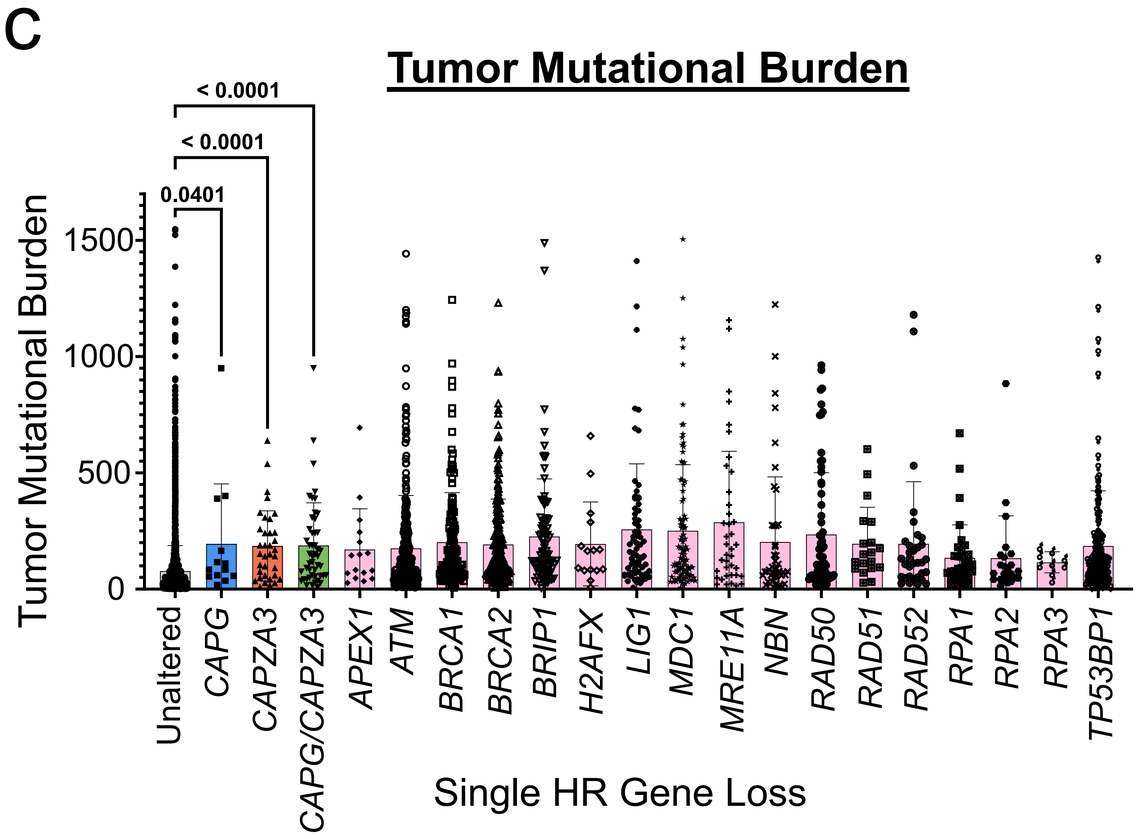

d

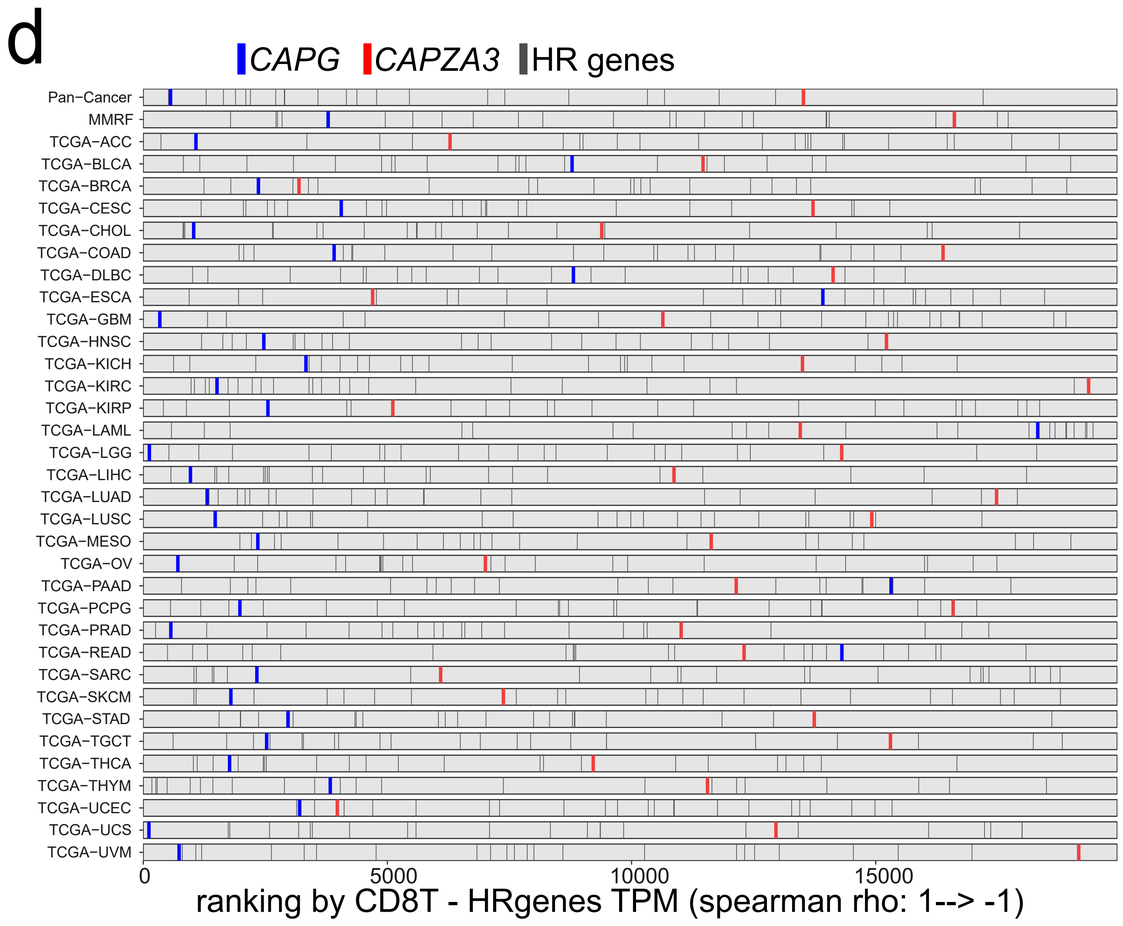

e

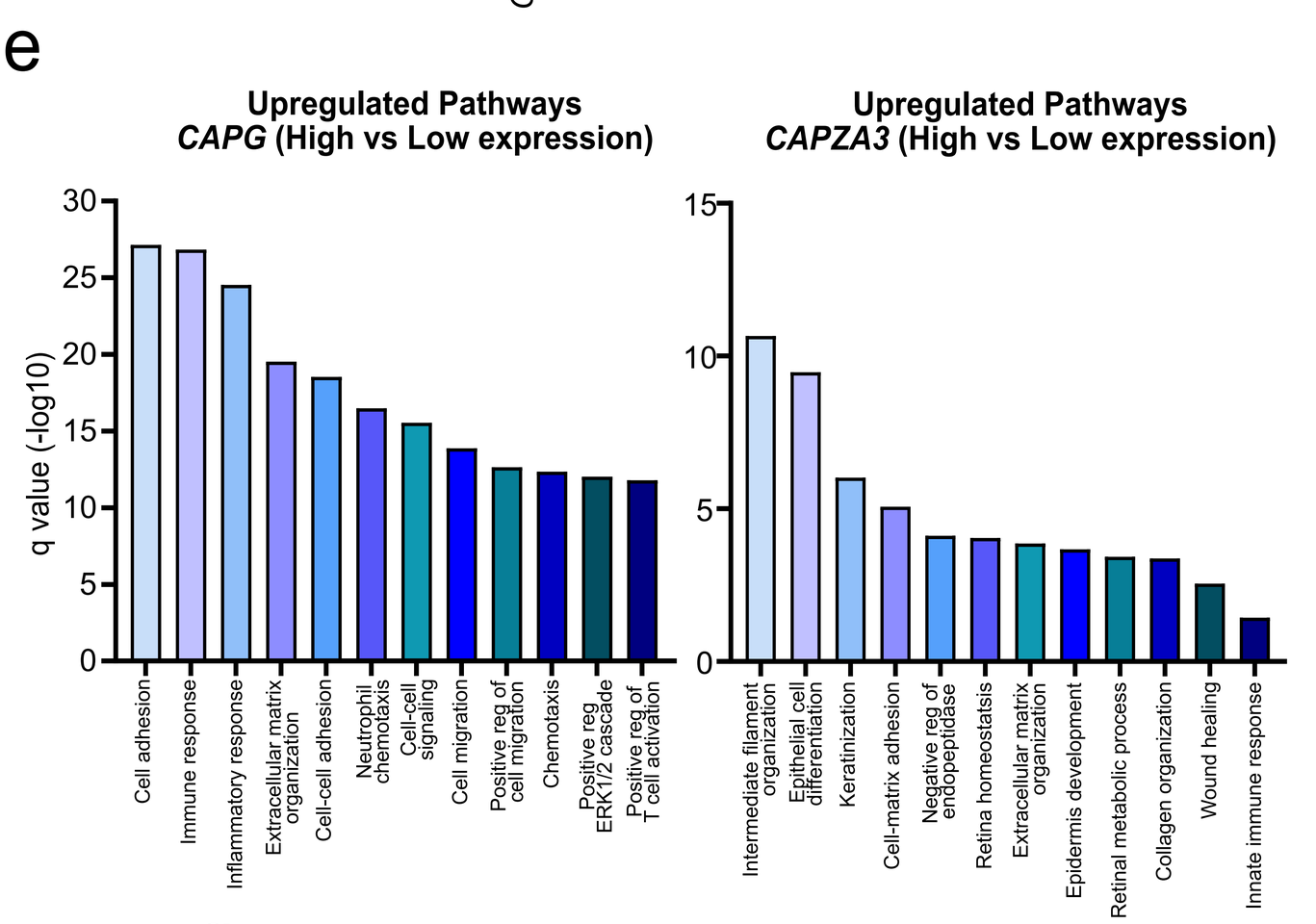

f

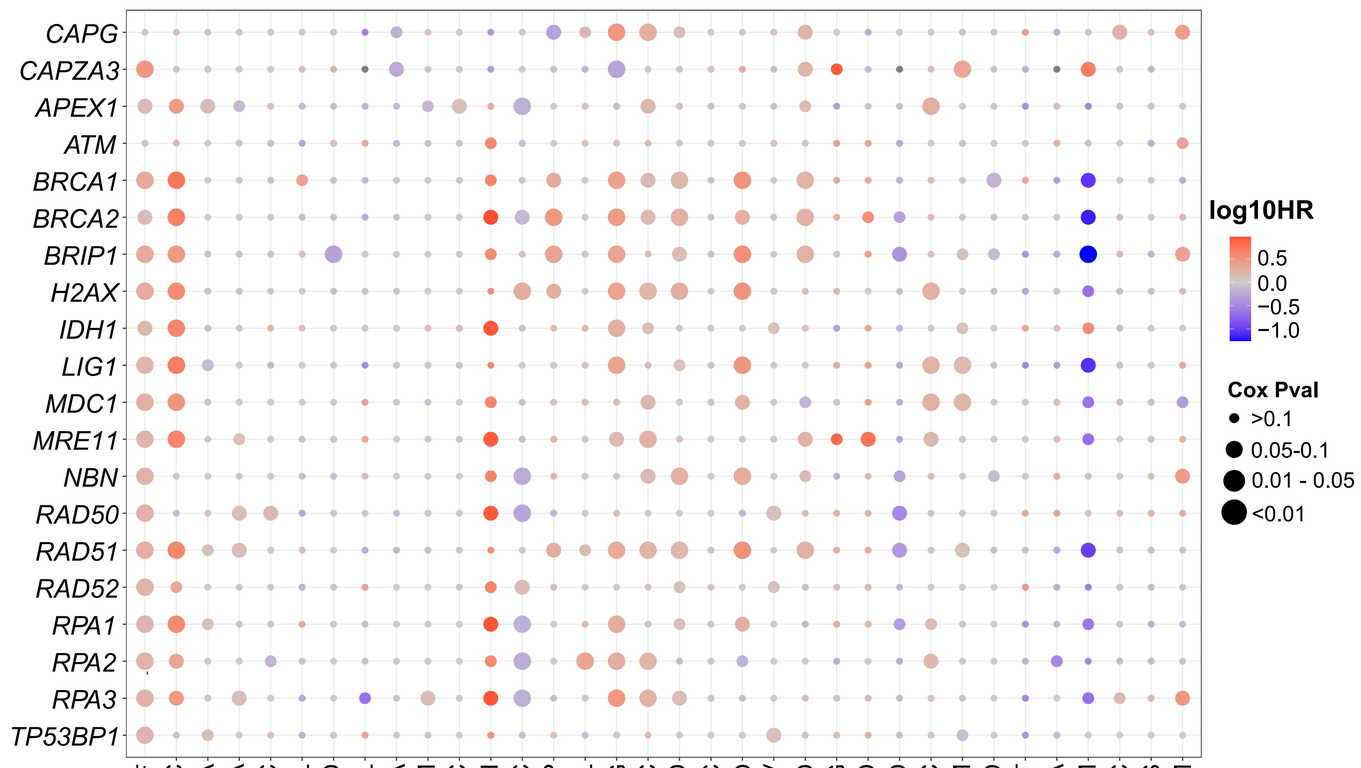

g

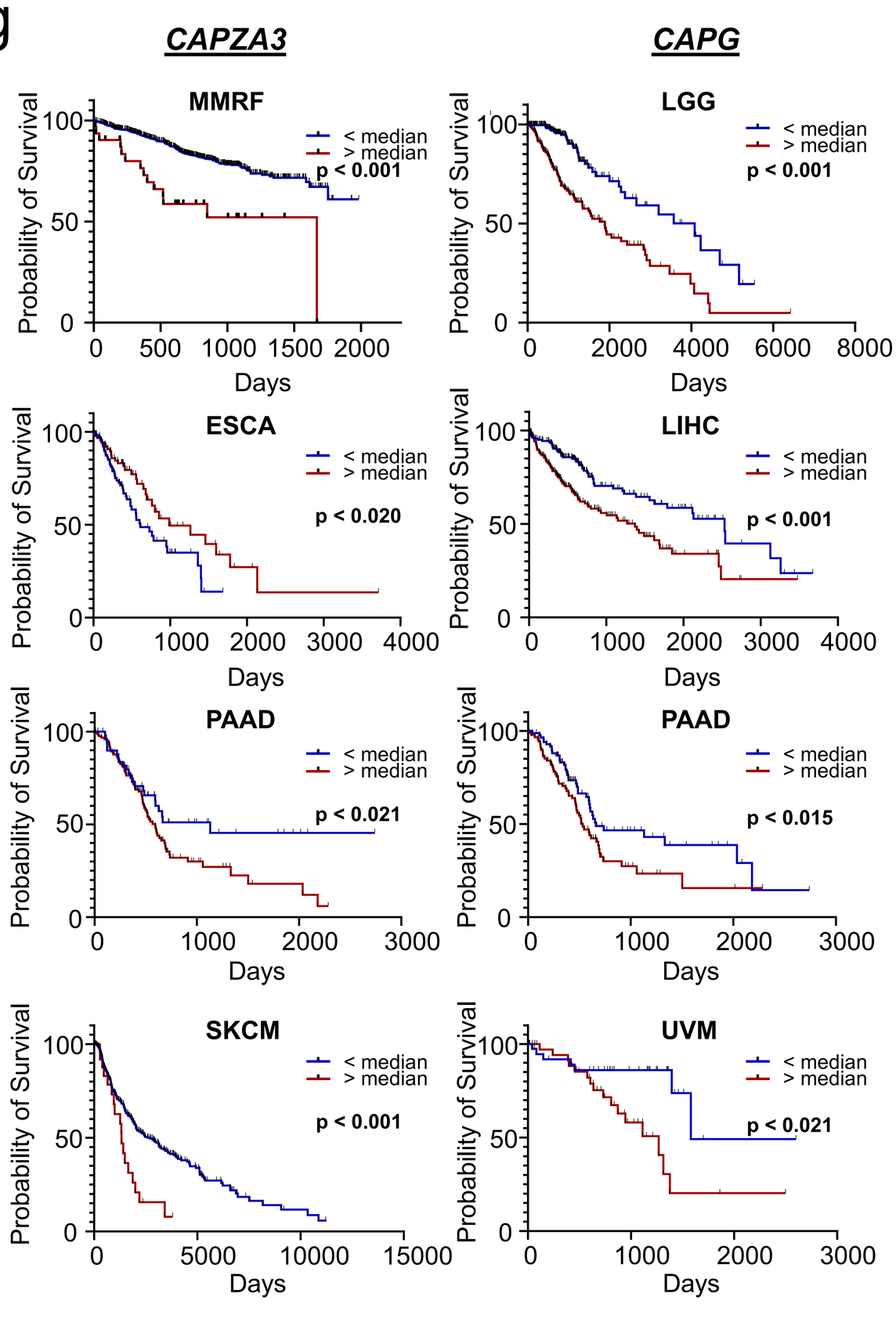

h

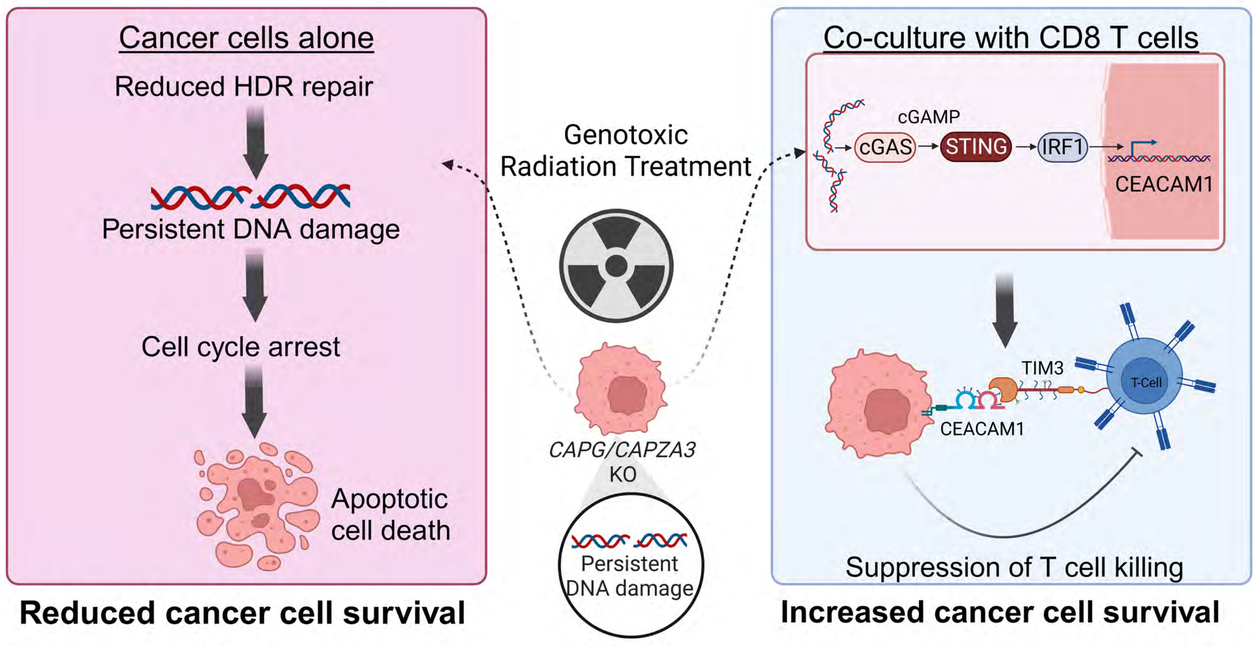

Supplementary Figure 1

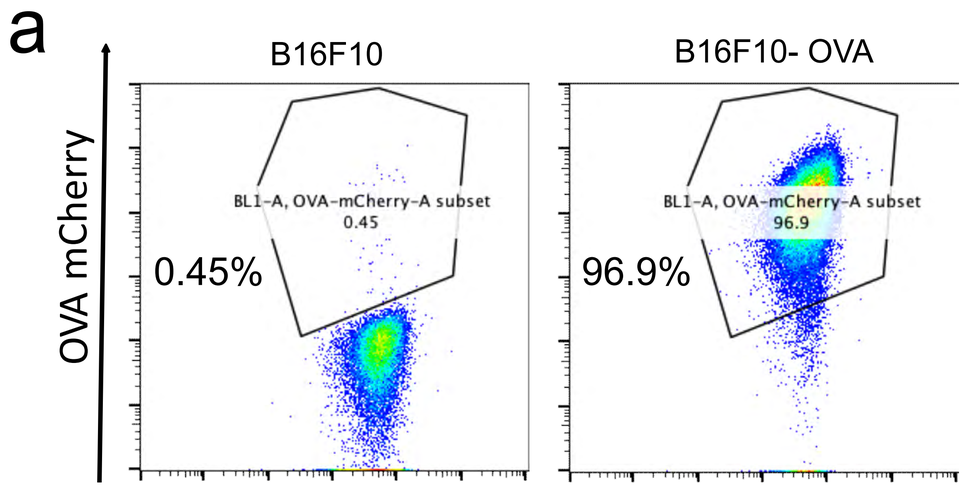

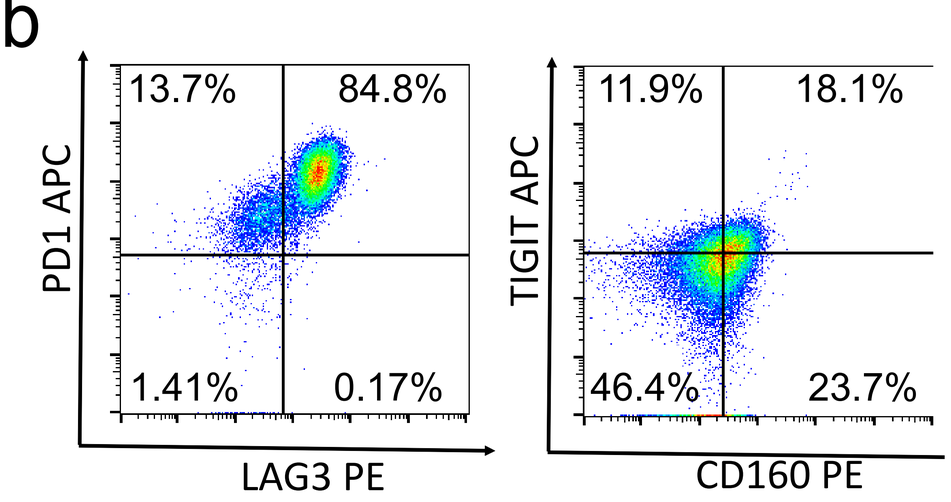

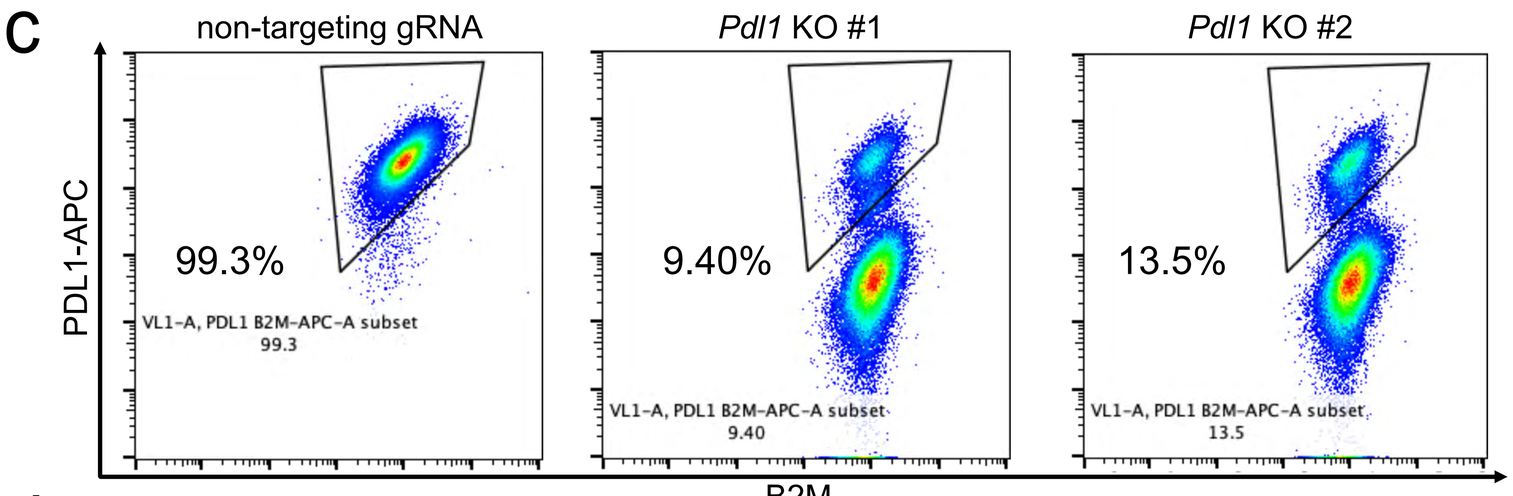

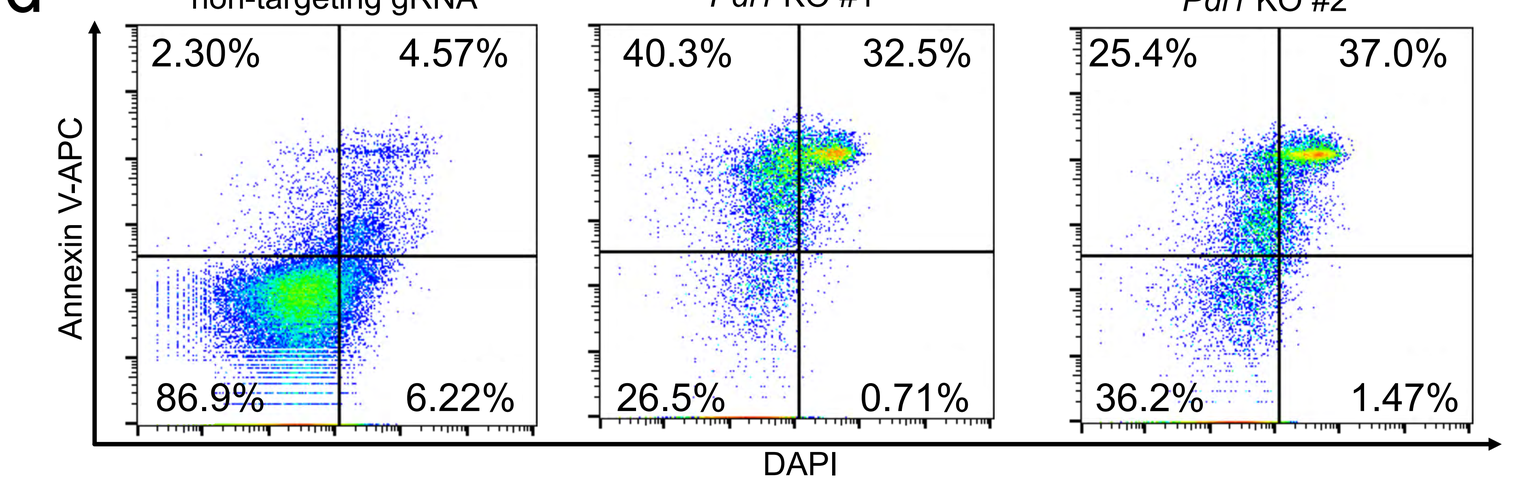

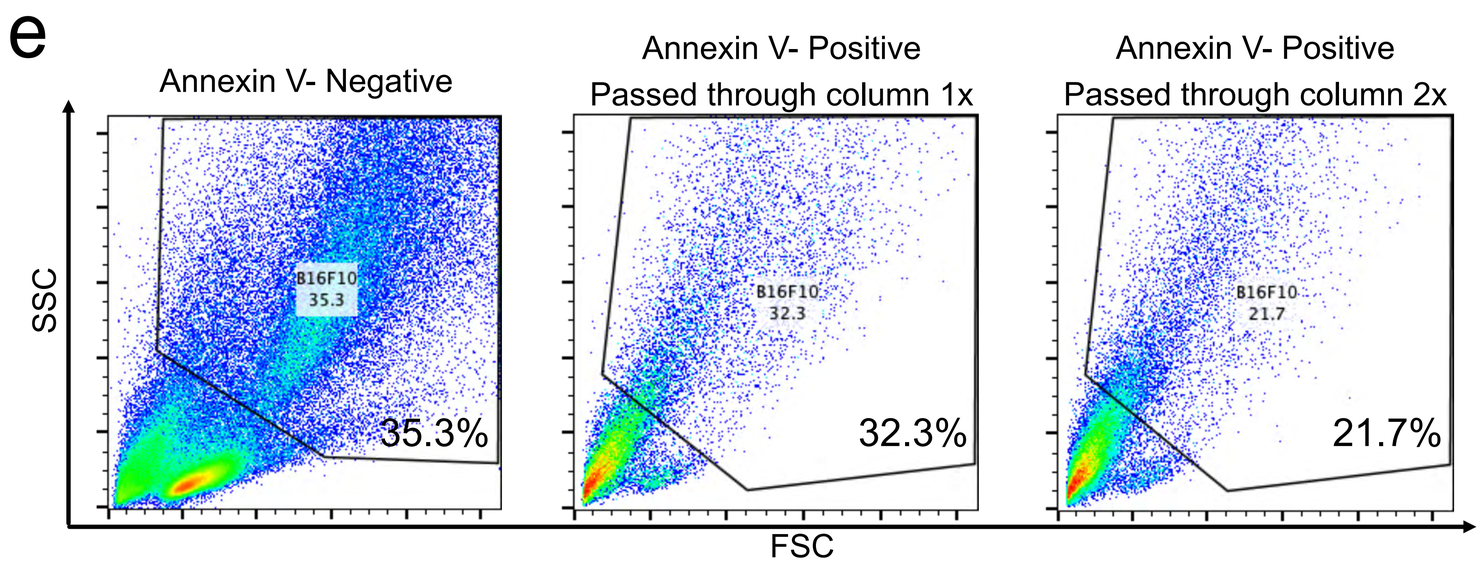

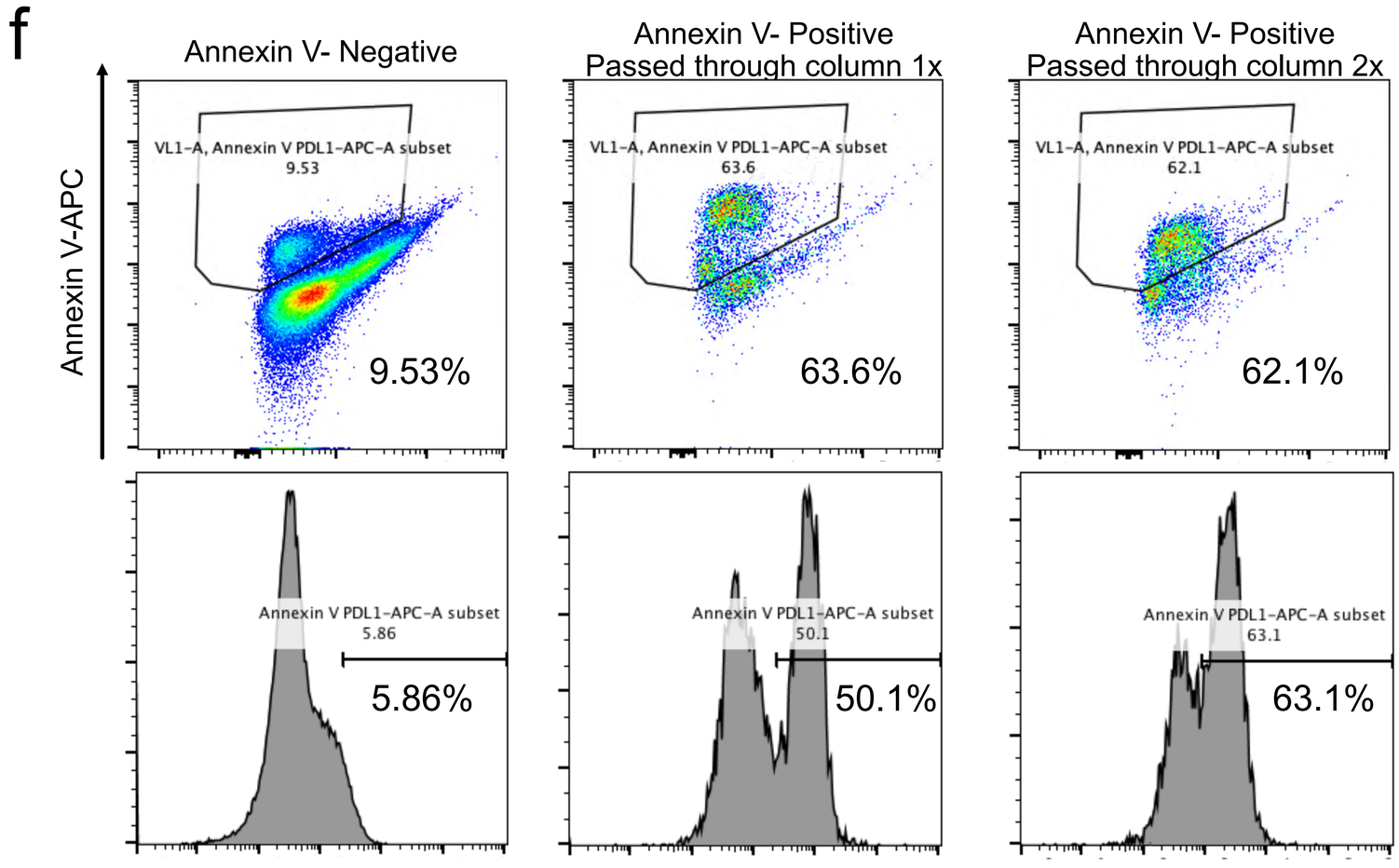

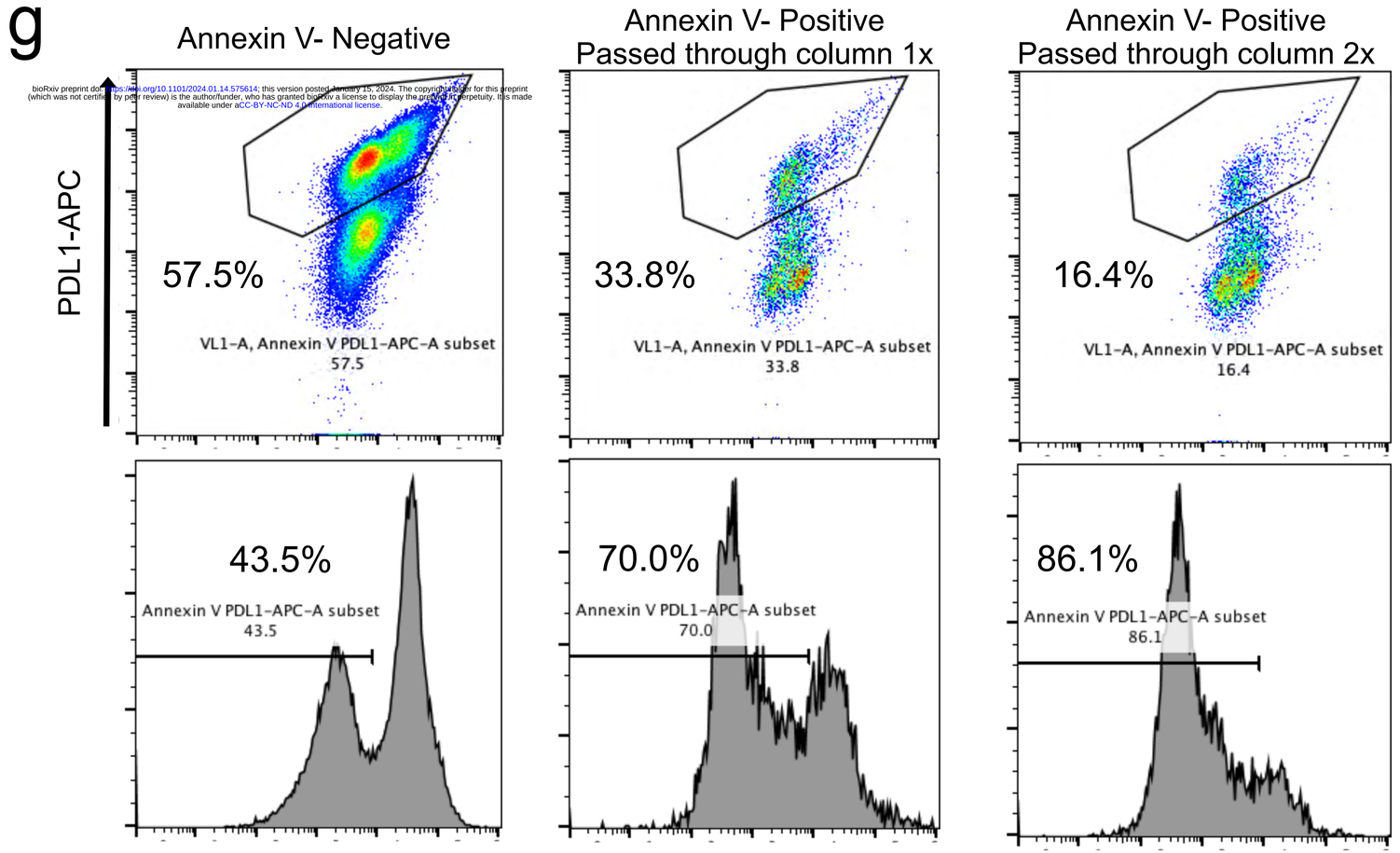

Supplementary Figure 2

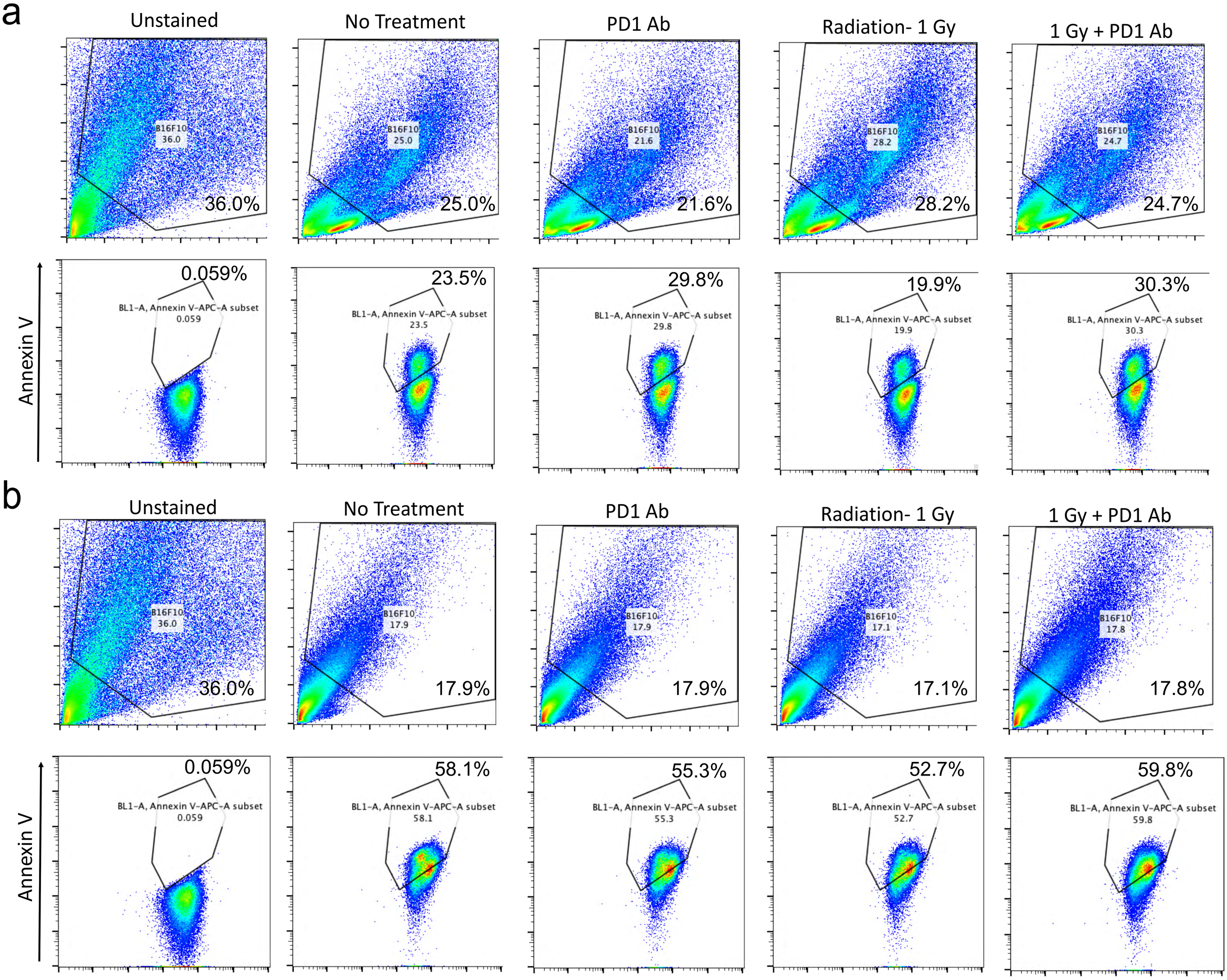

Supplementary Figure 3

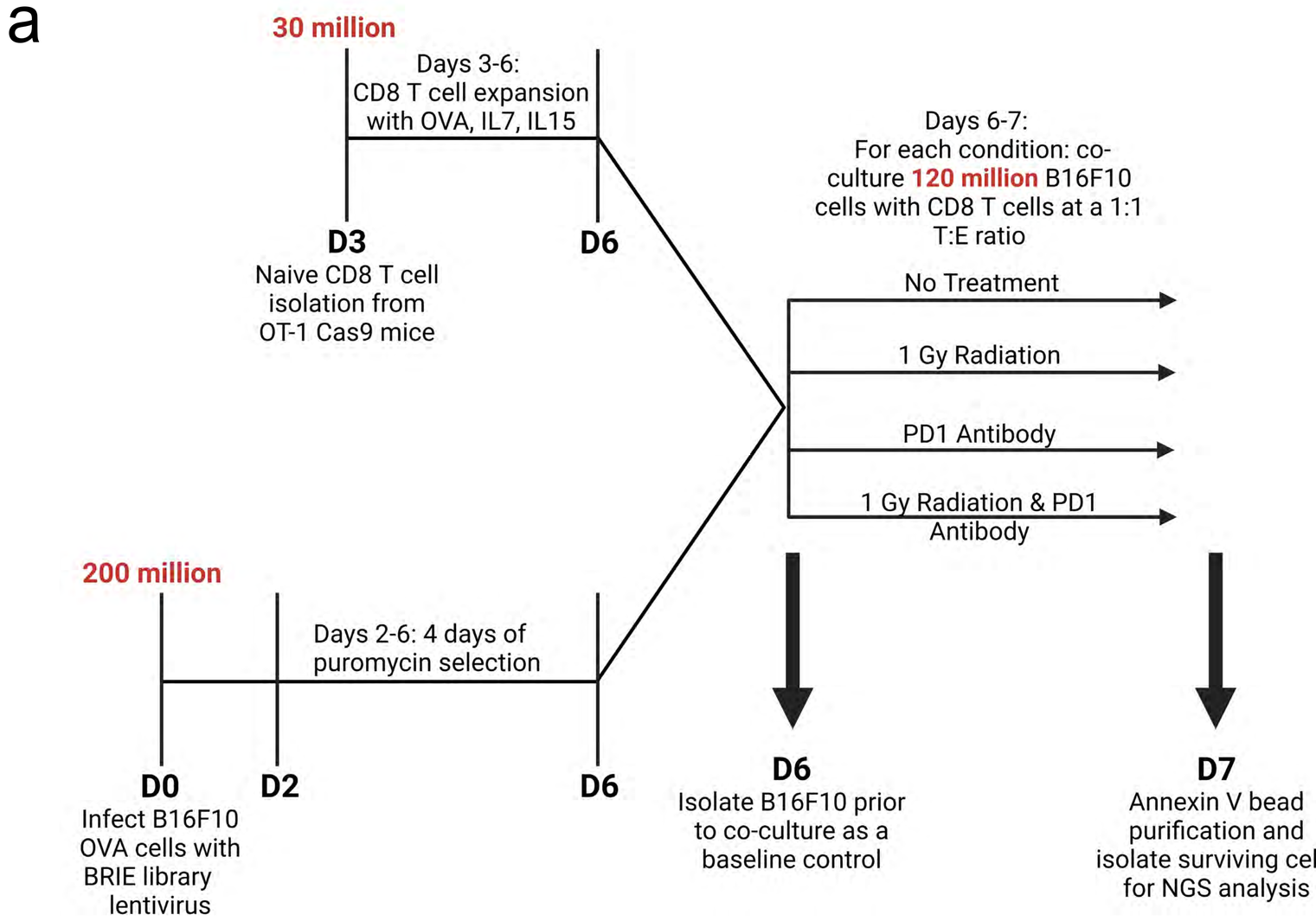

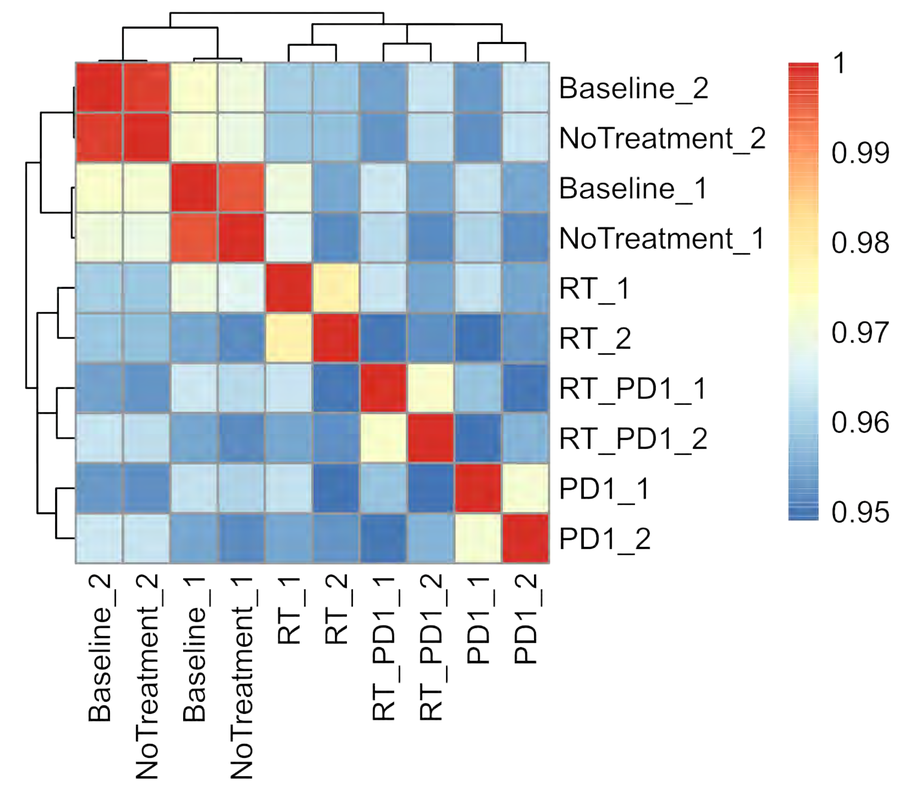

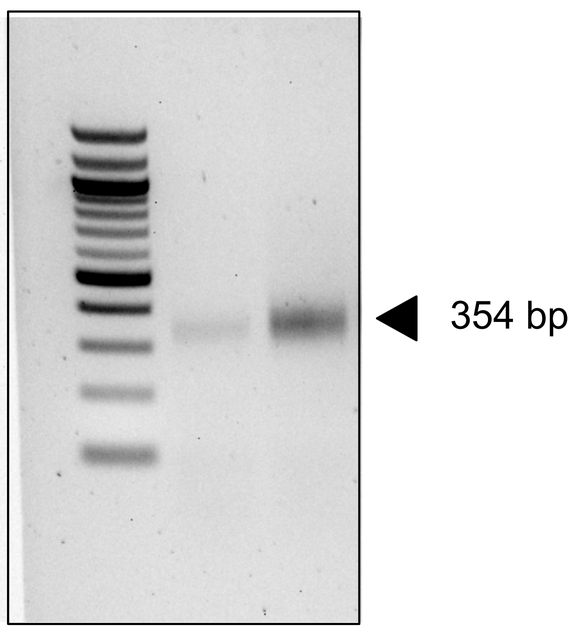

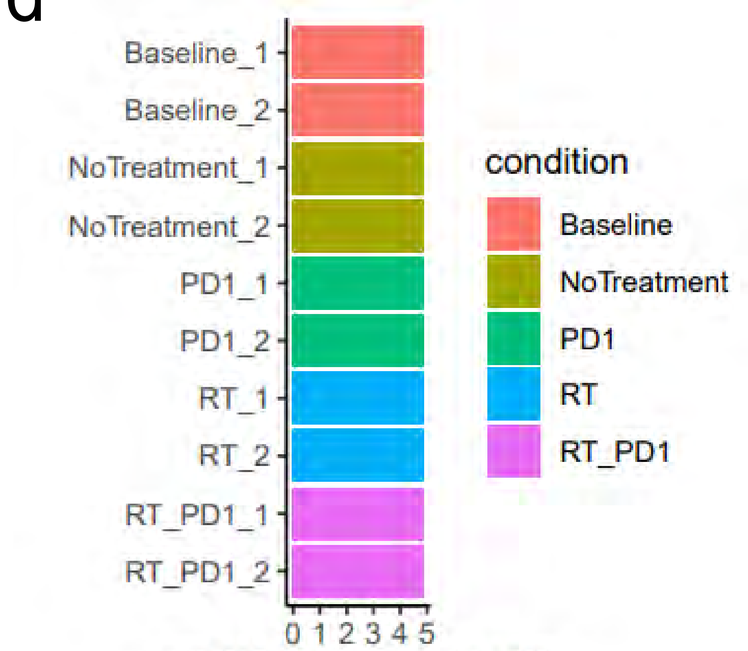

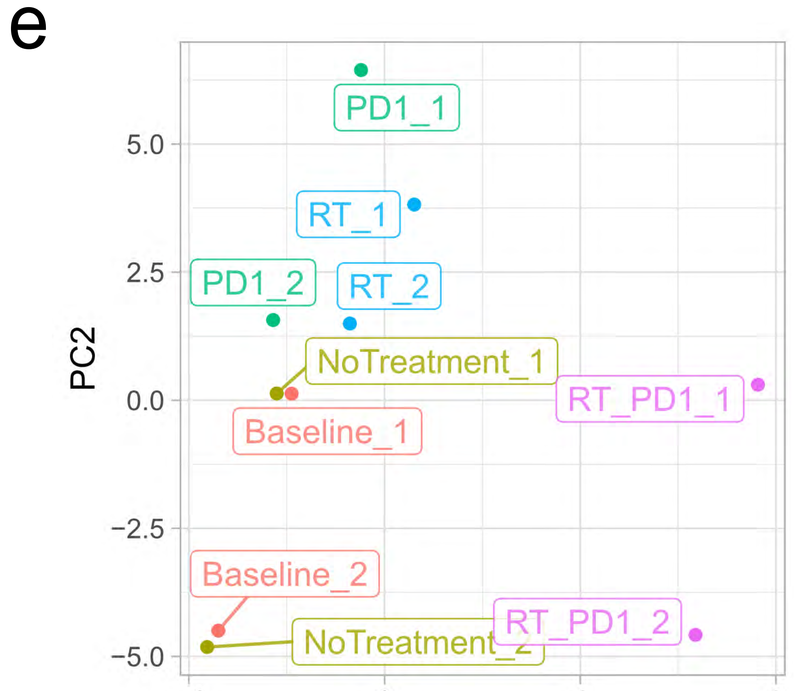

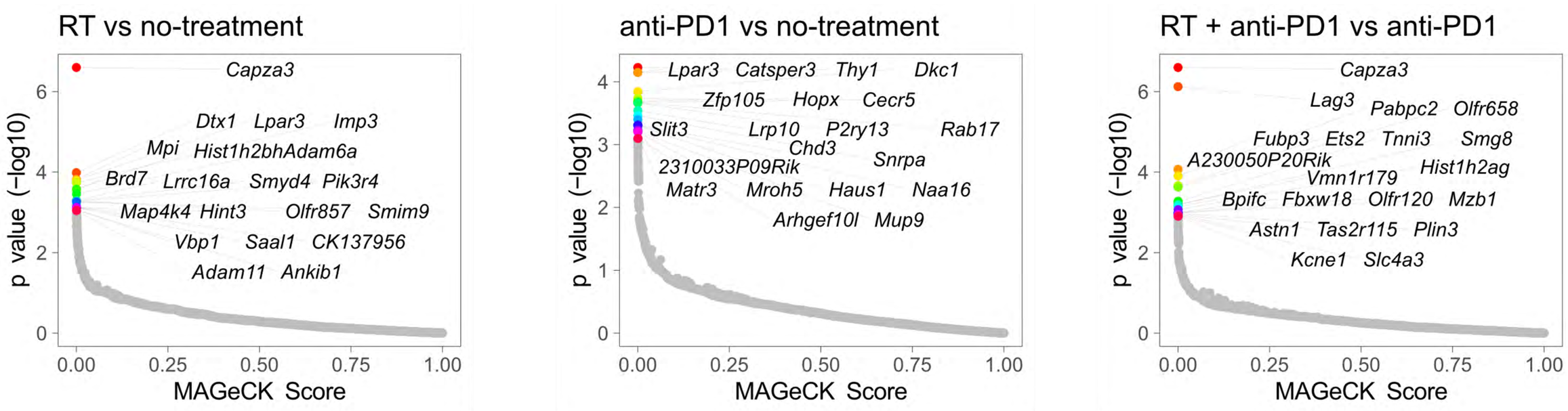

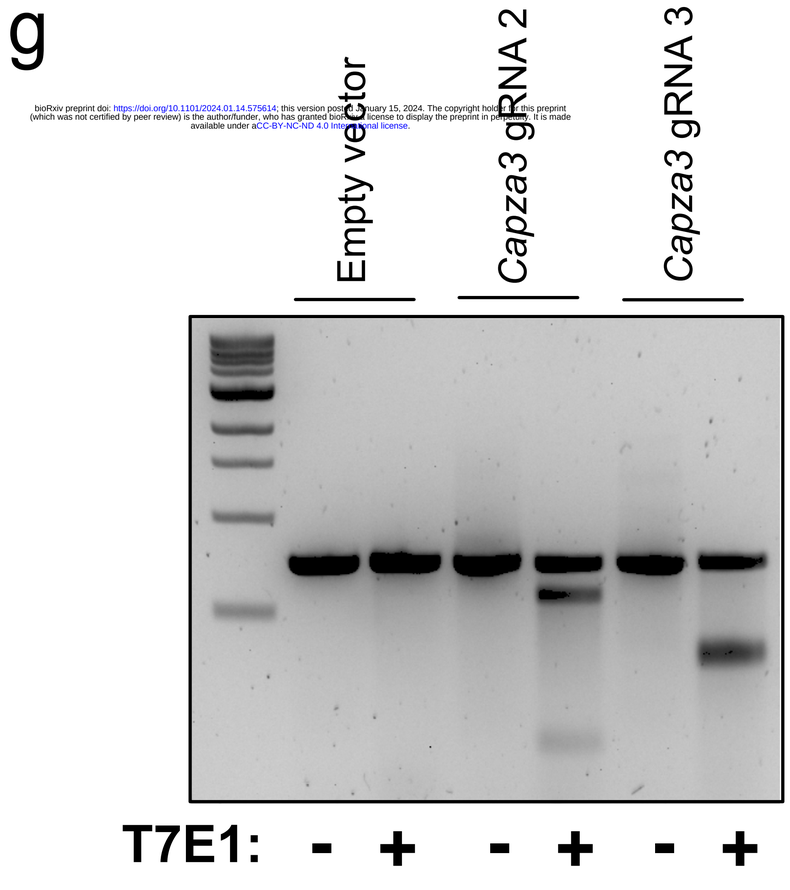

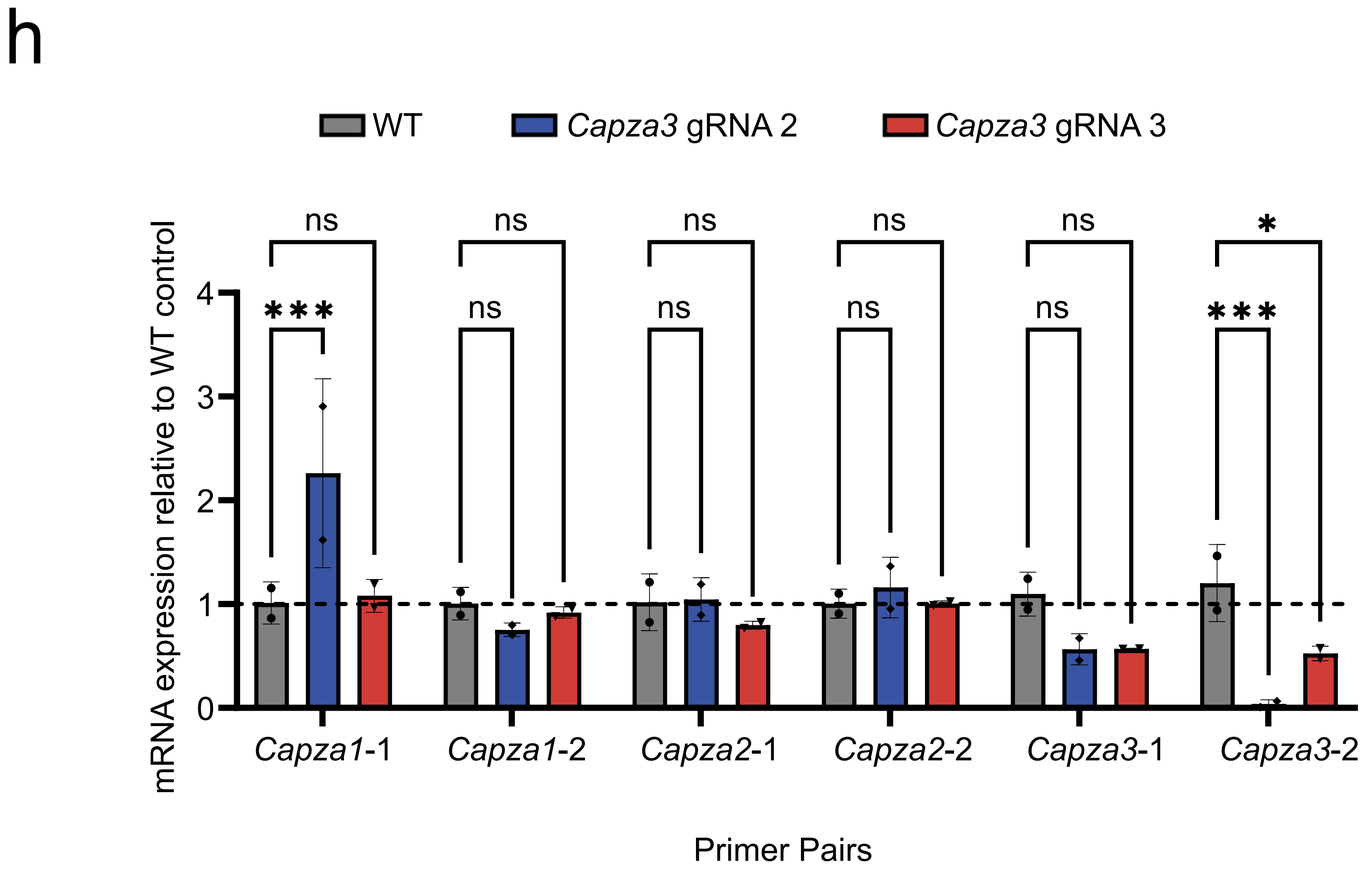

Supplementary Figure 4

a

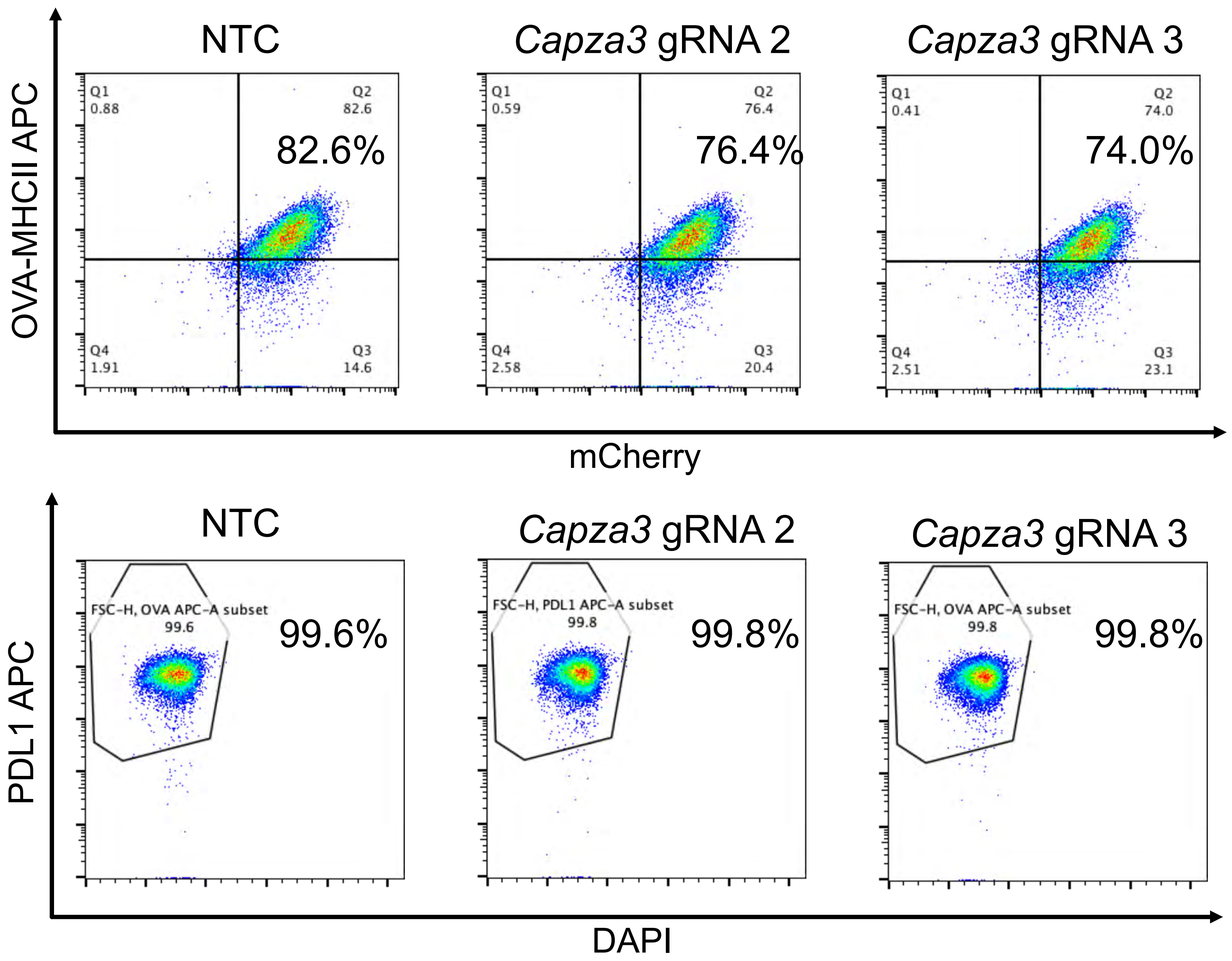

b

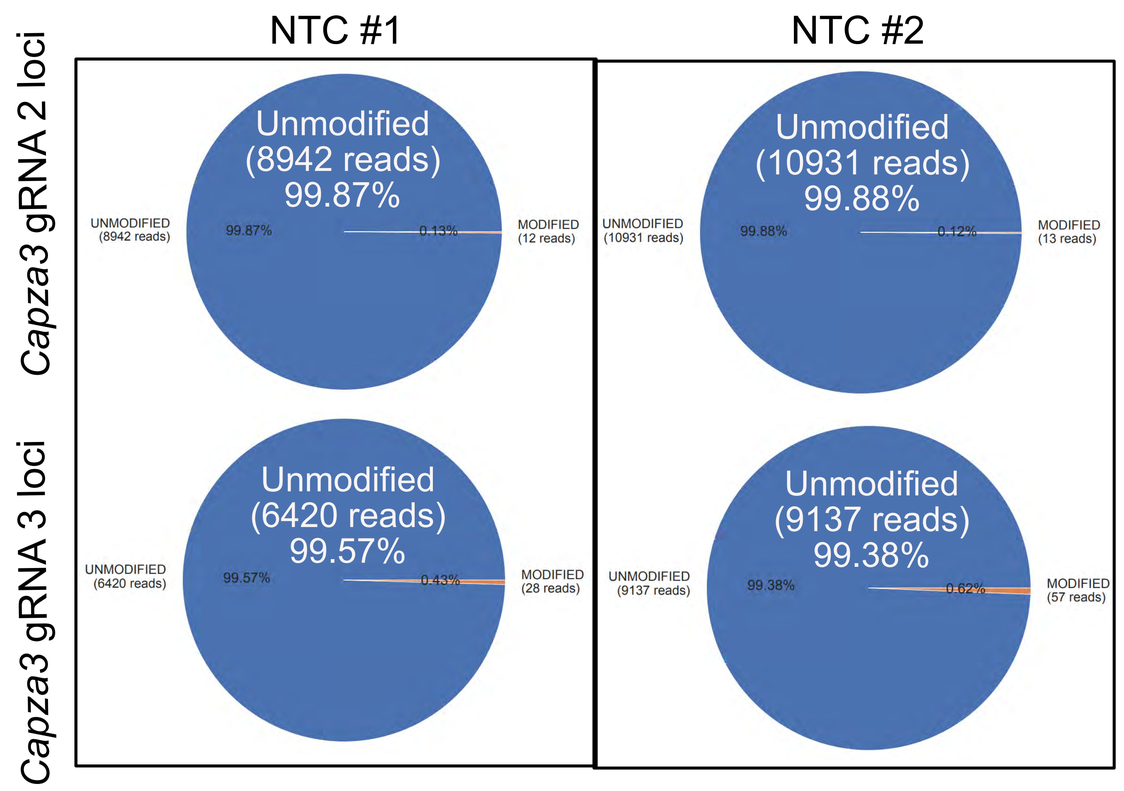

c

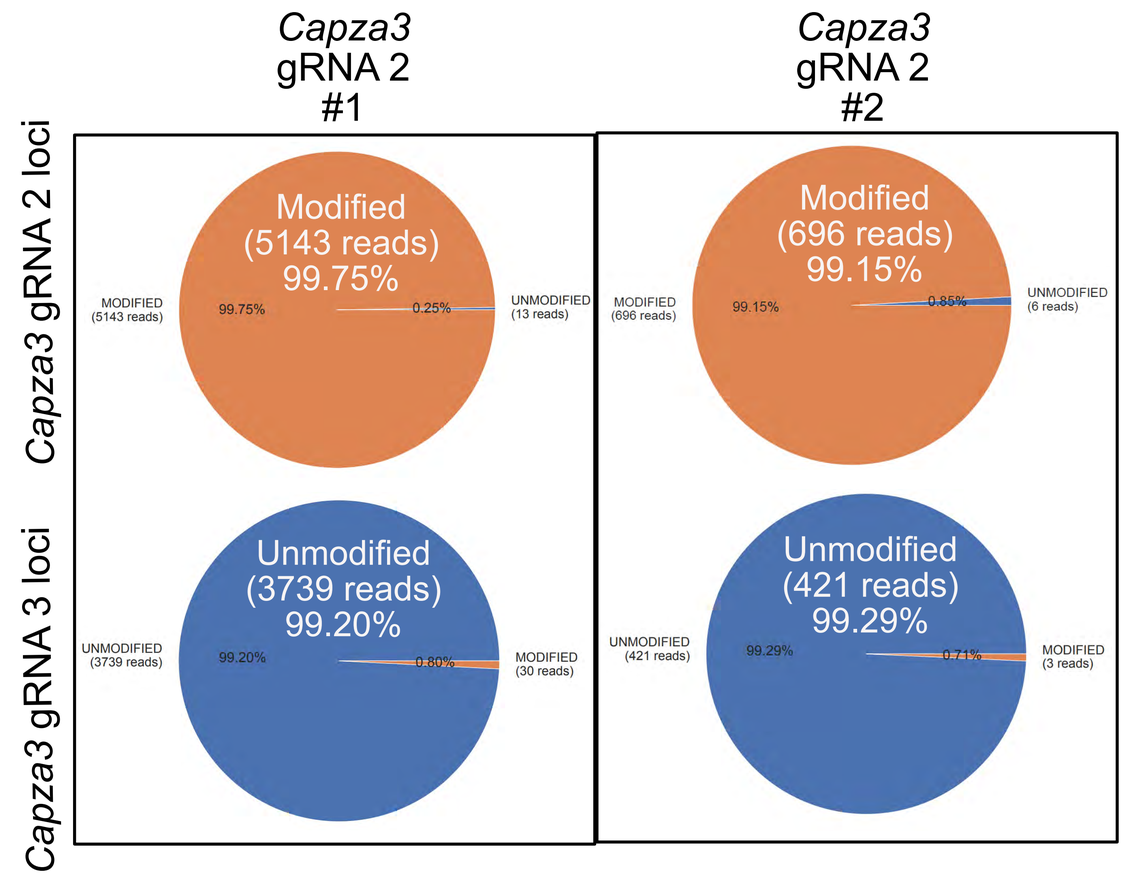

d

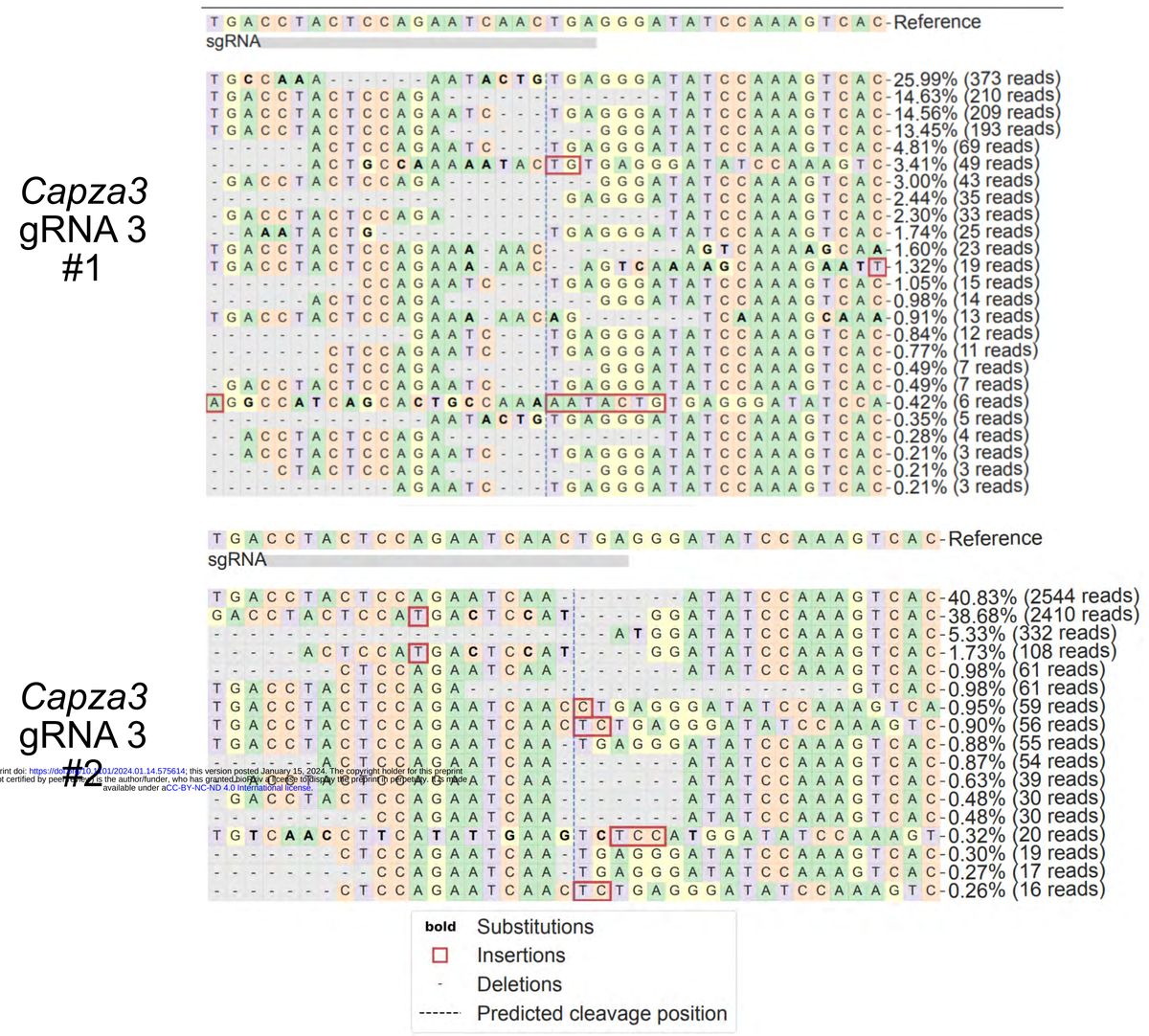

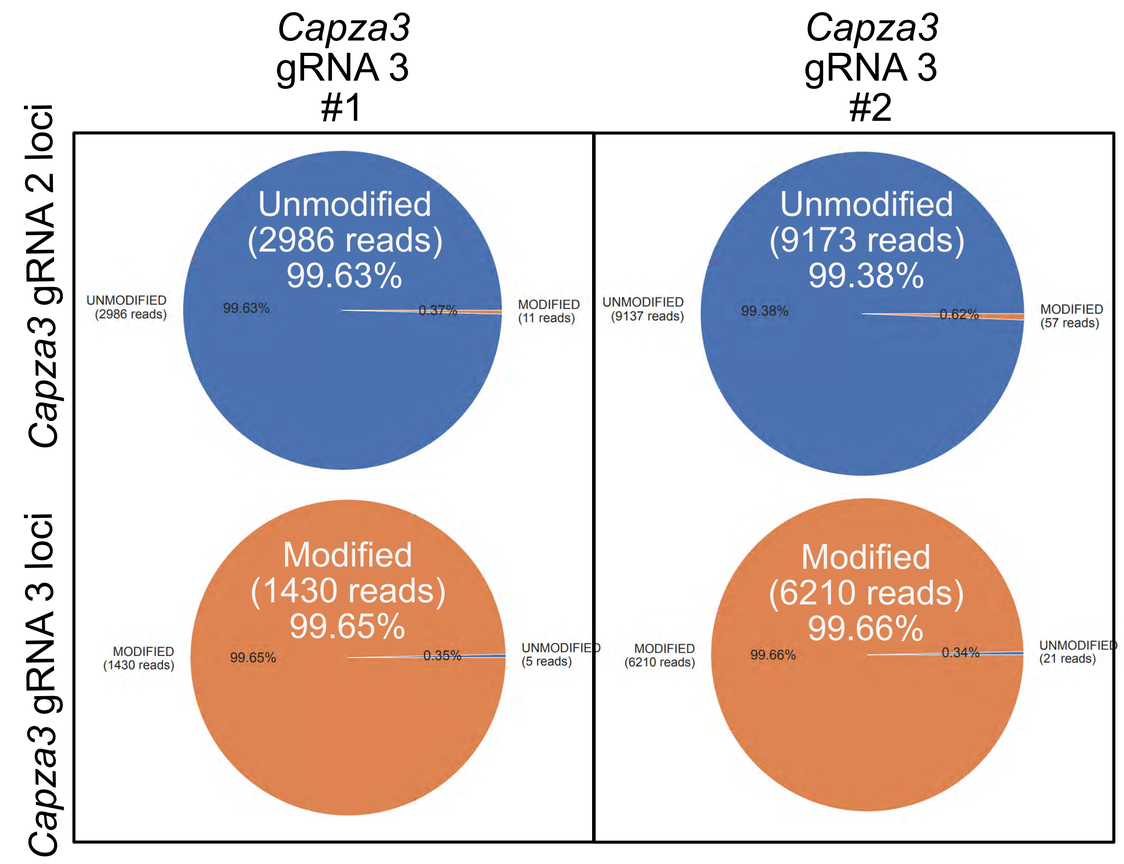

Supplementary Figure 5

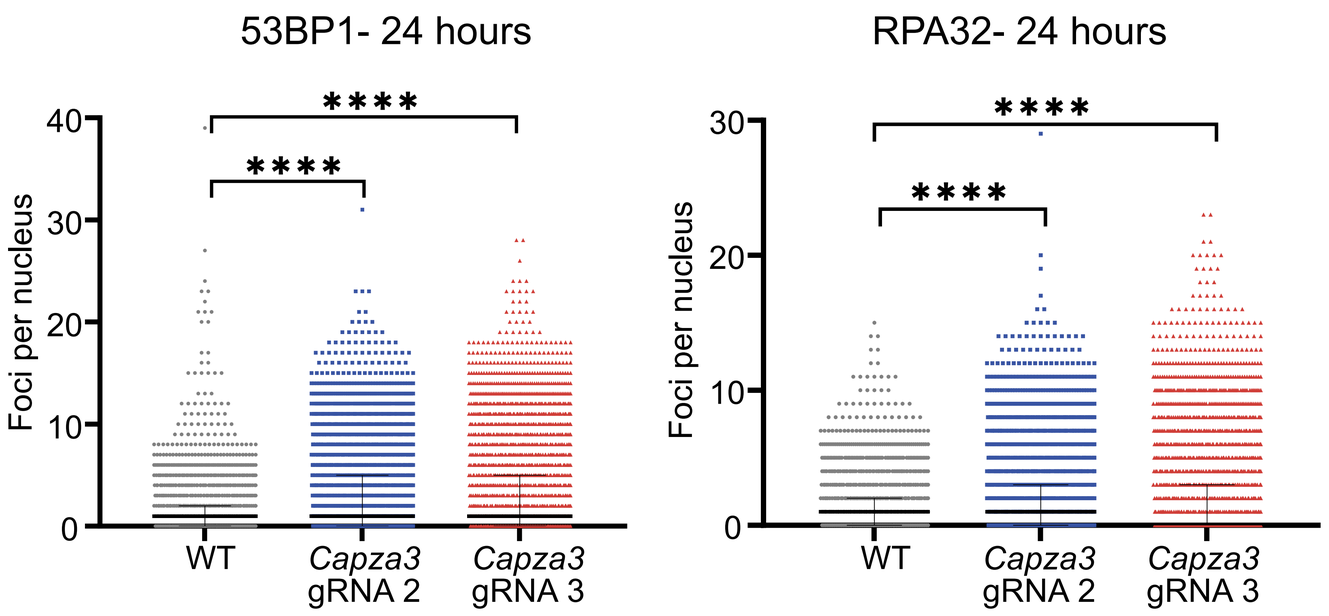

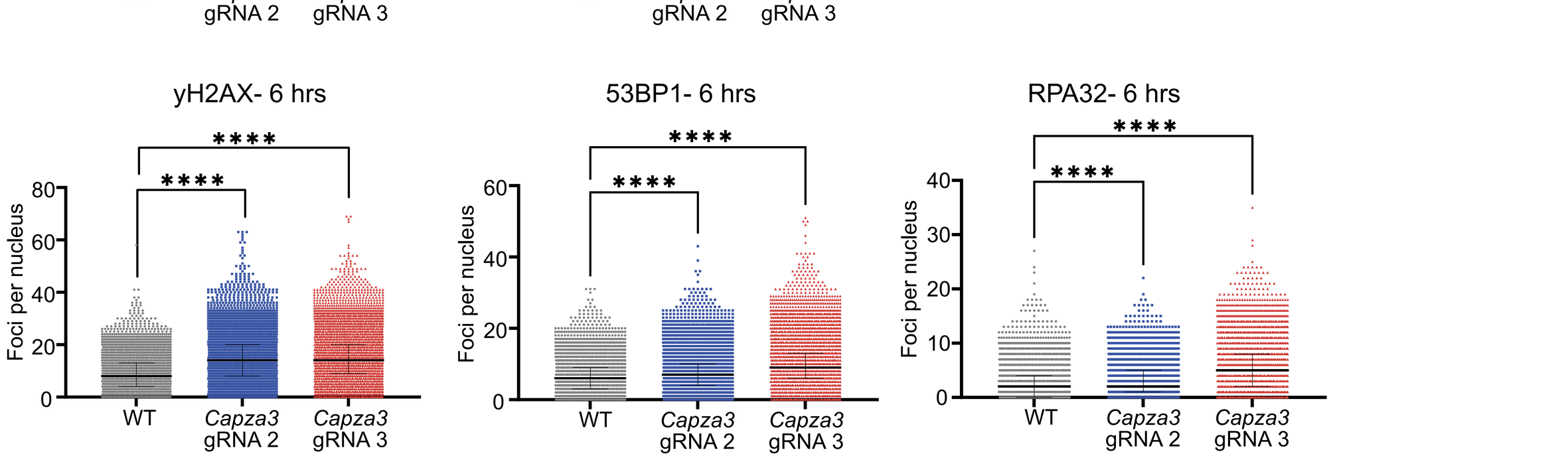

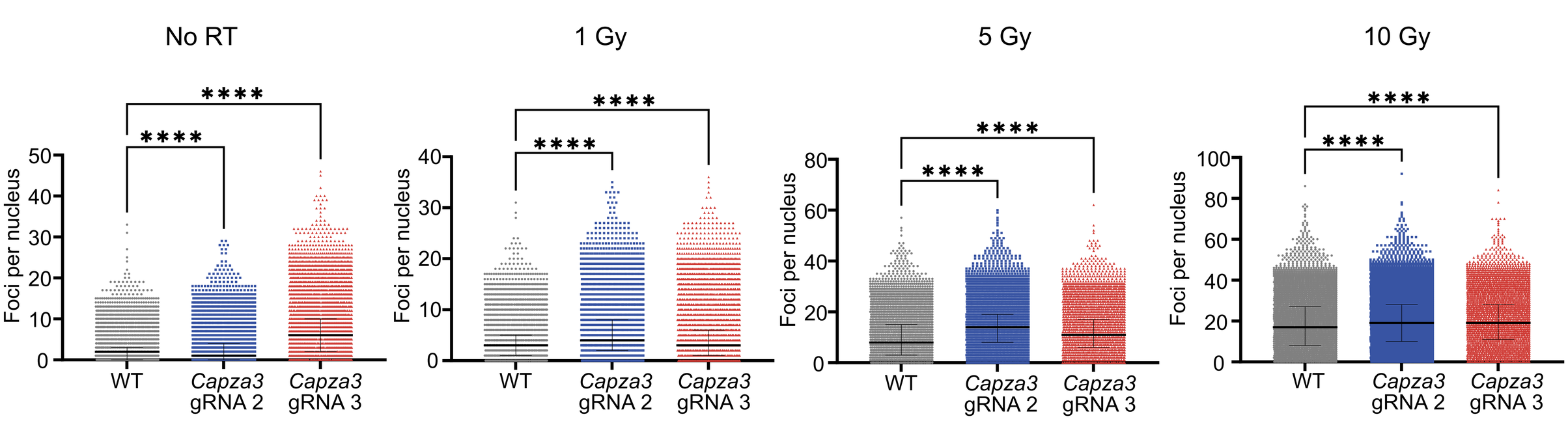

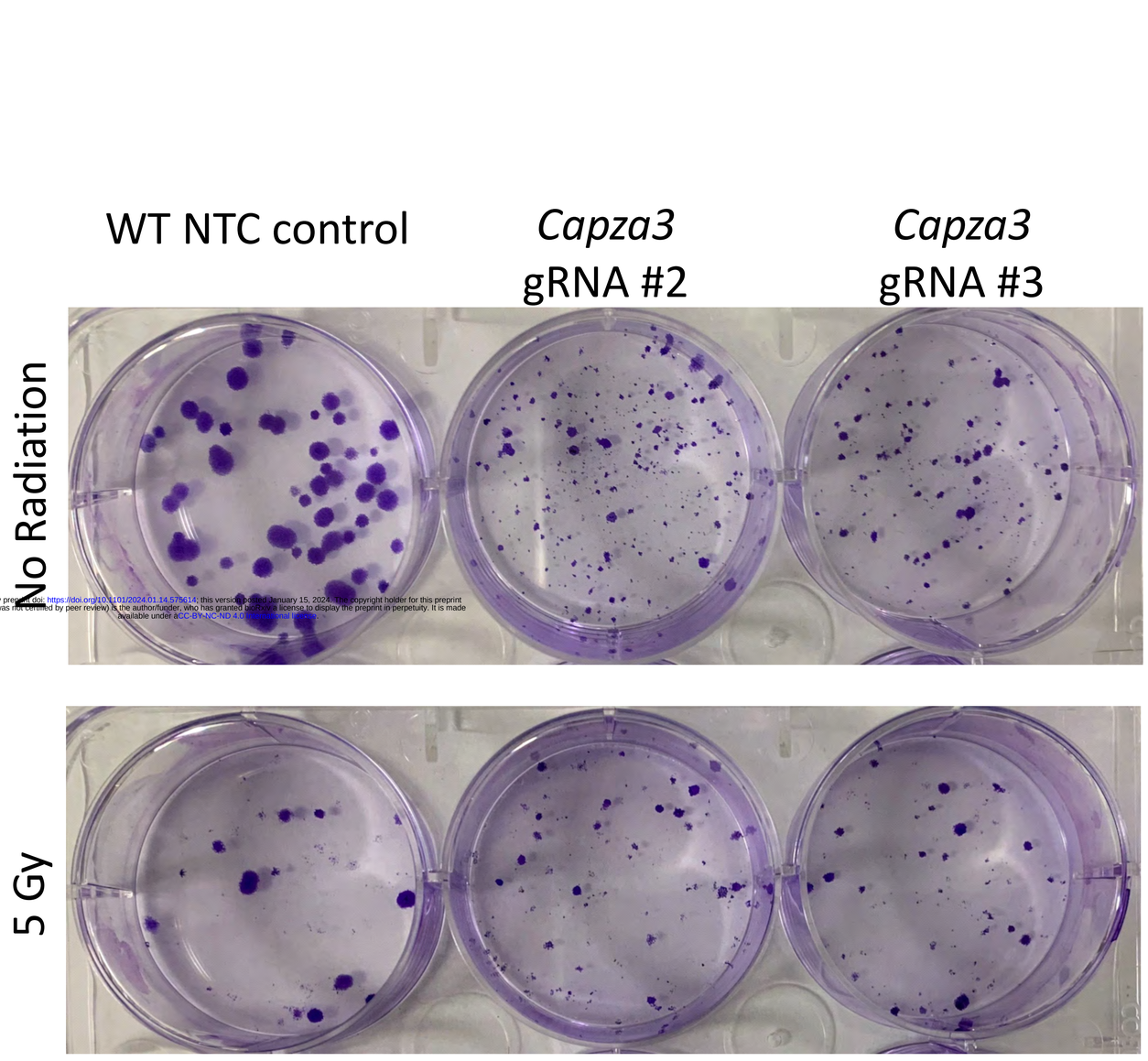

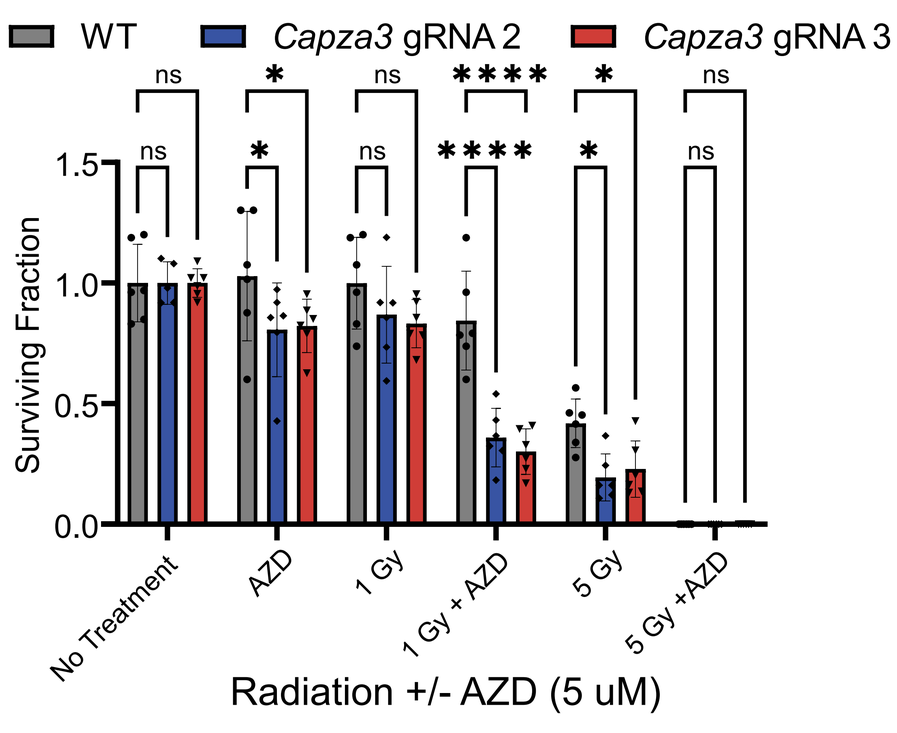

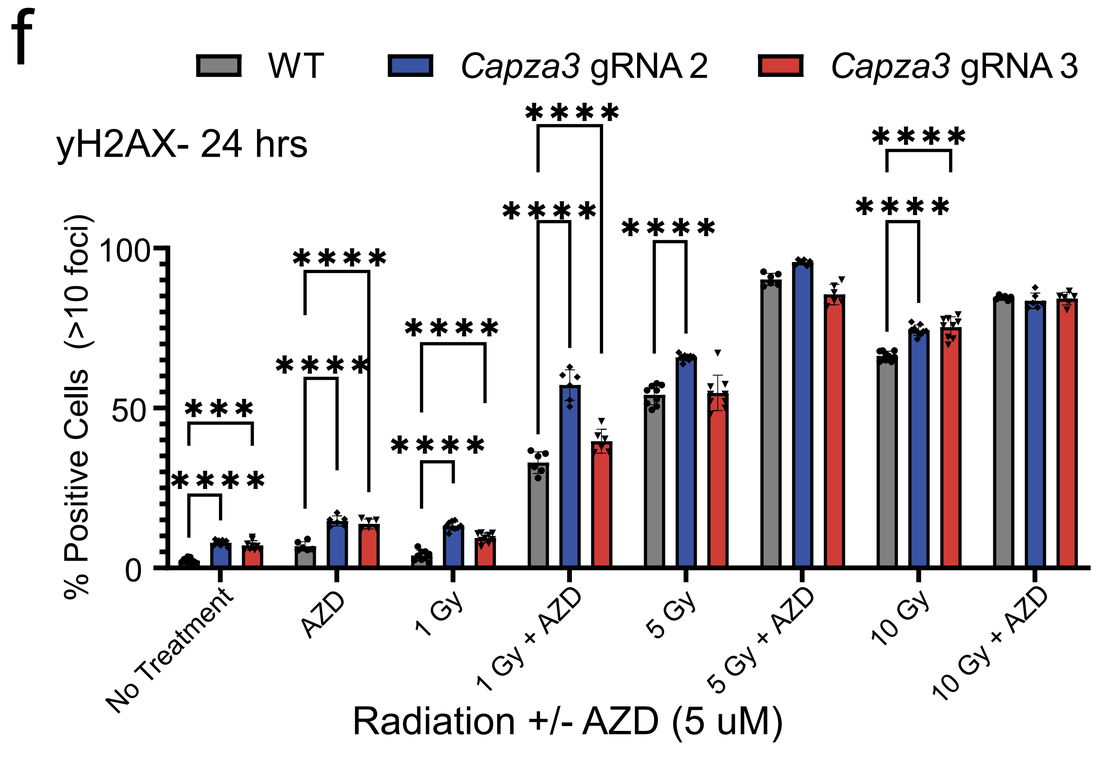

Supplementary Figure 6

a

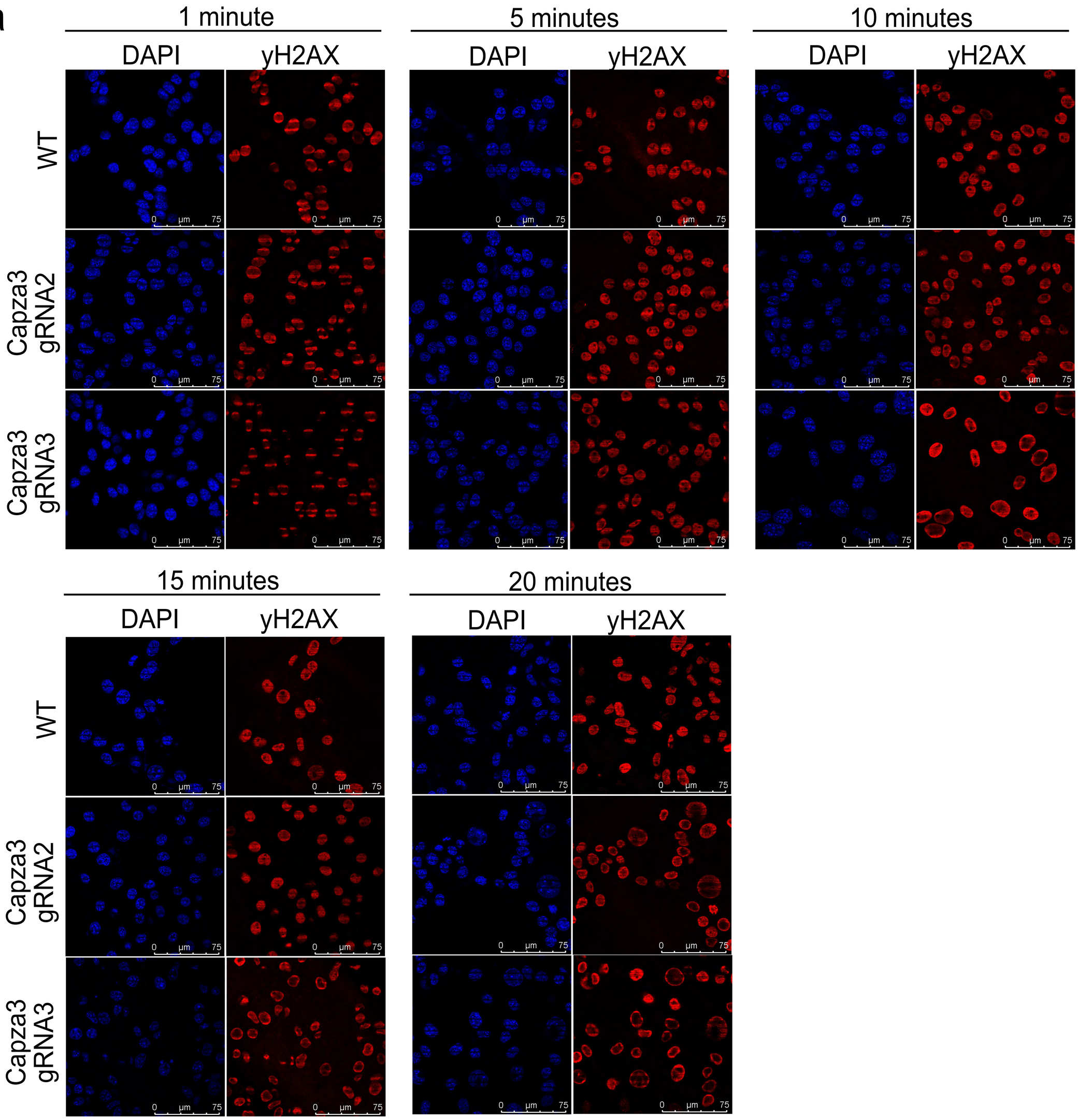

b

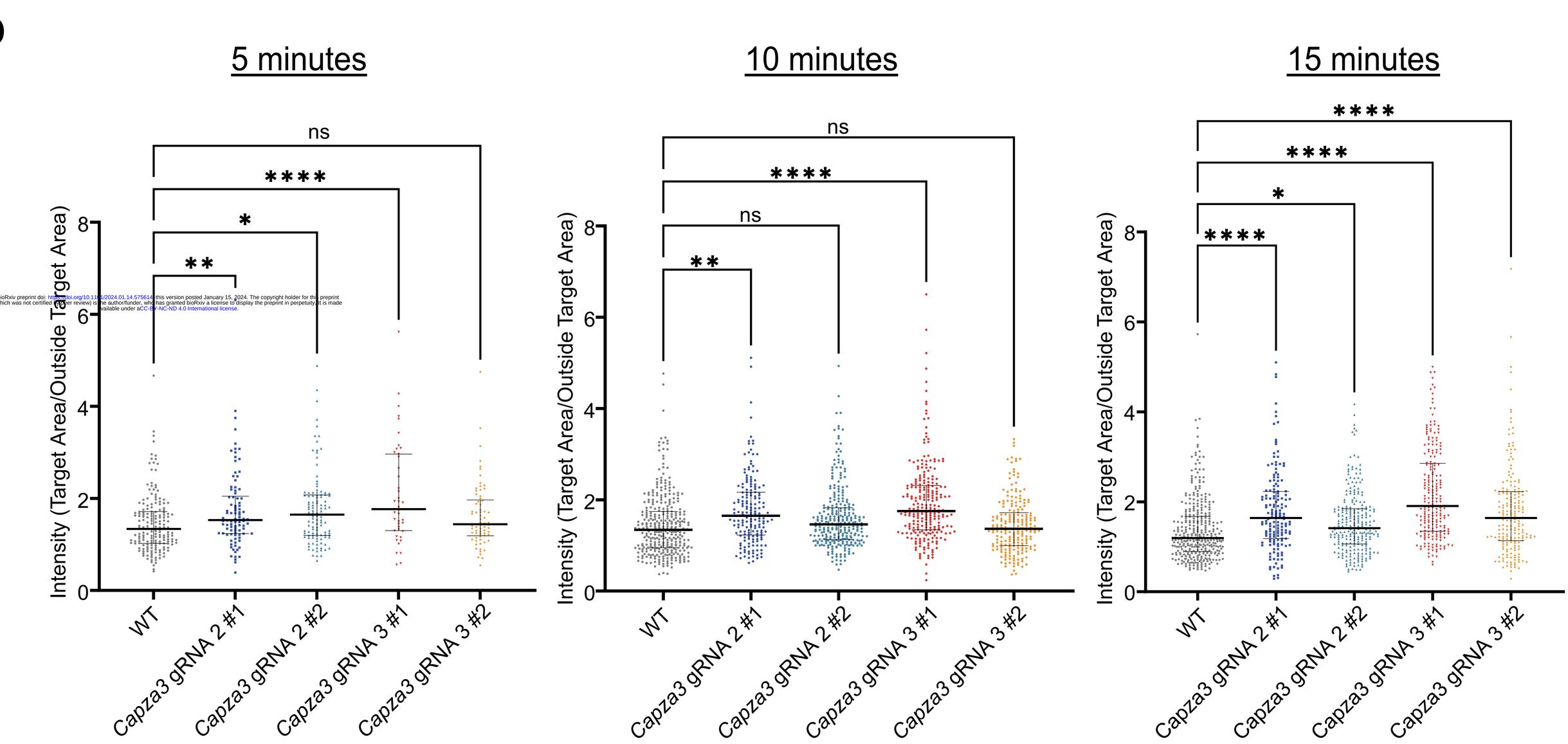

Supplementary Figure 7

a

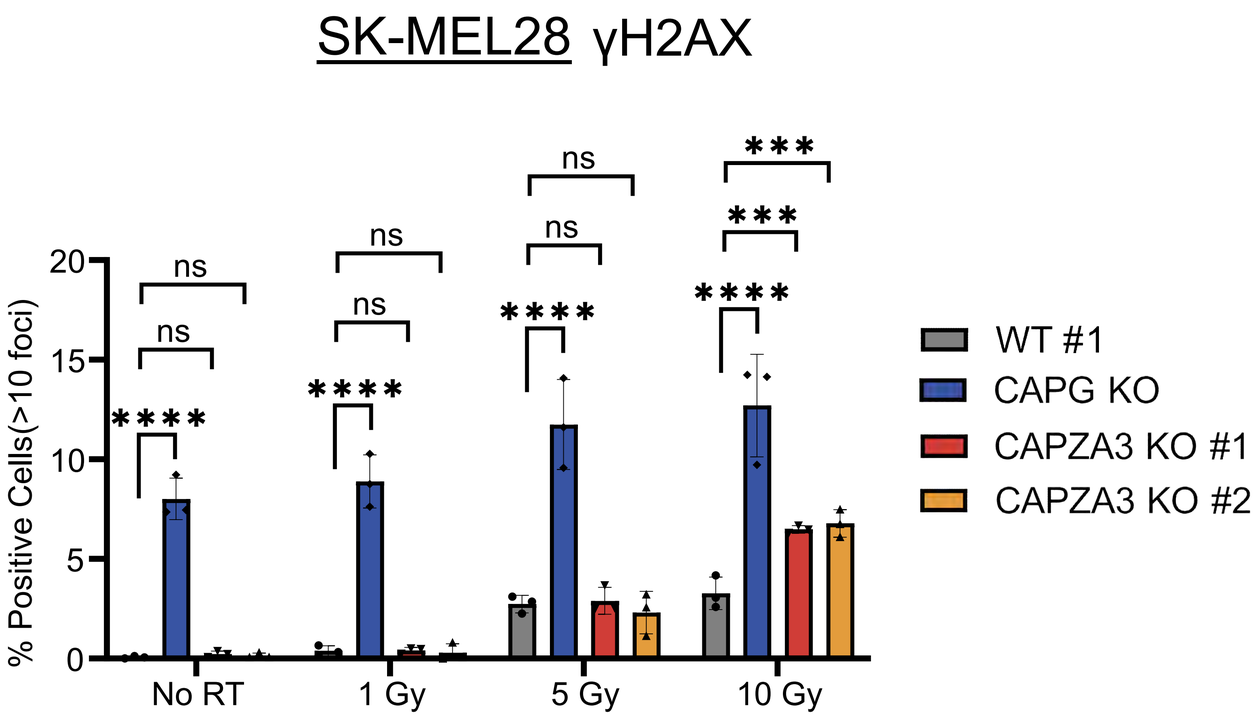

b

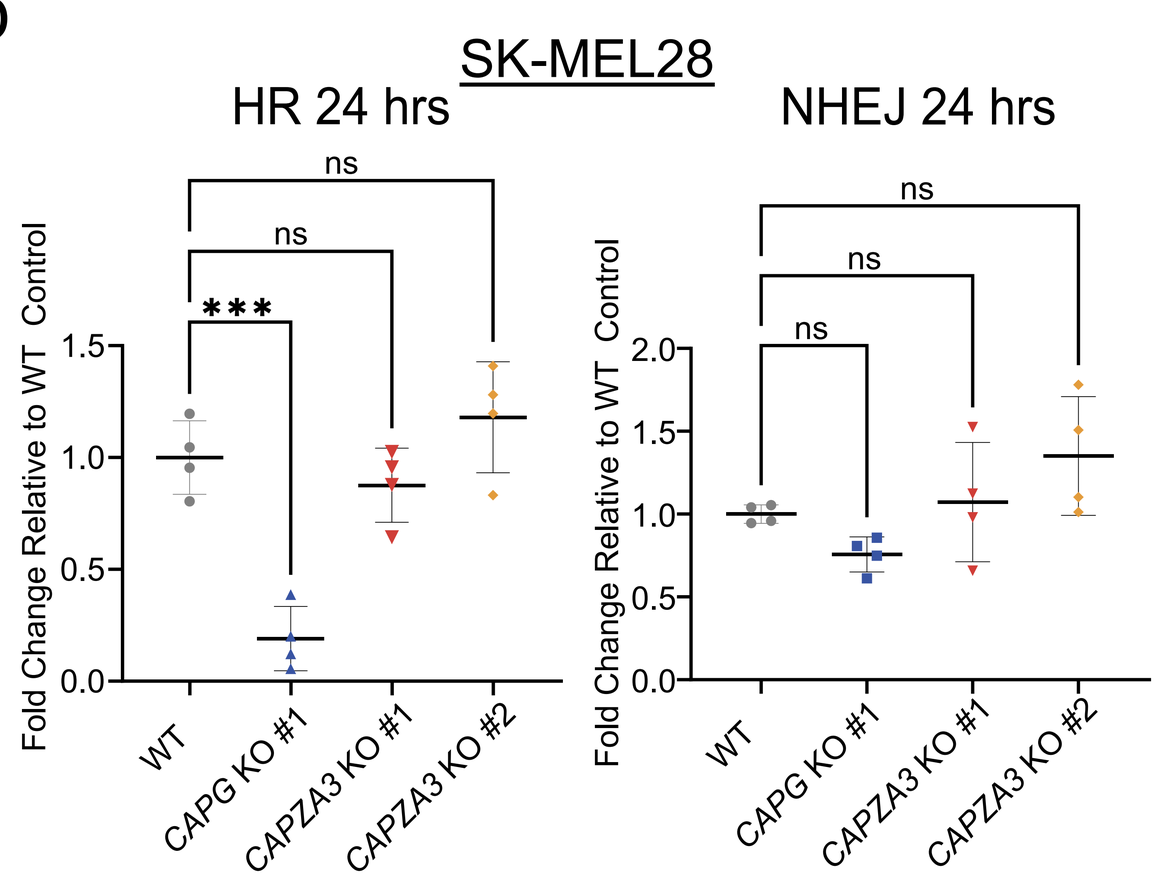

c

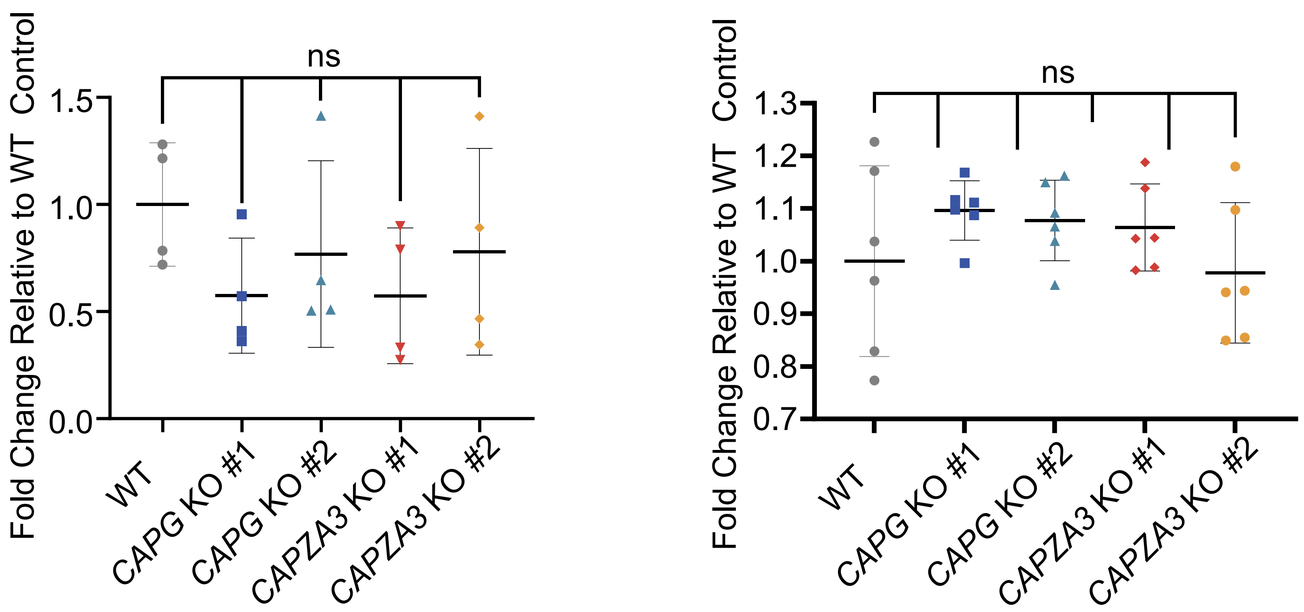

d

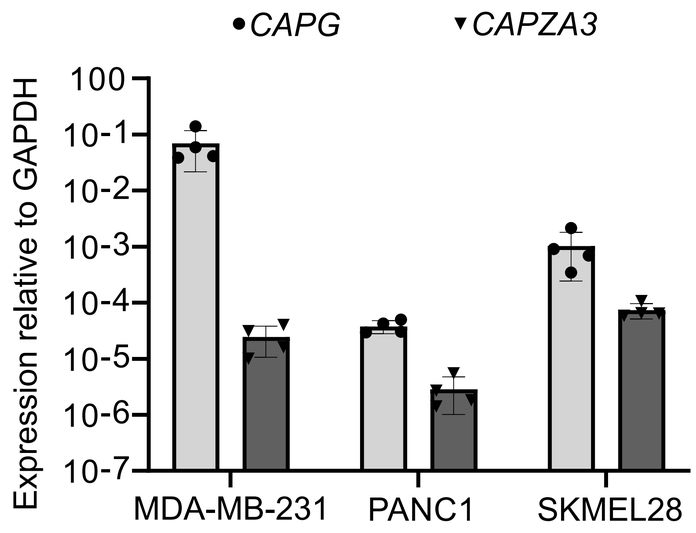

e

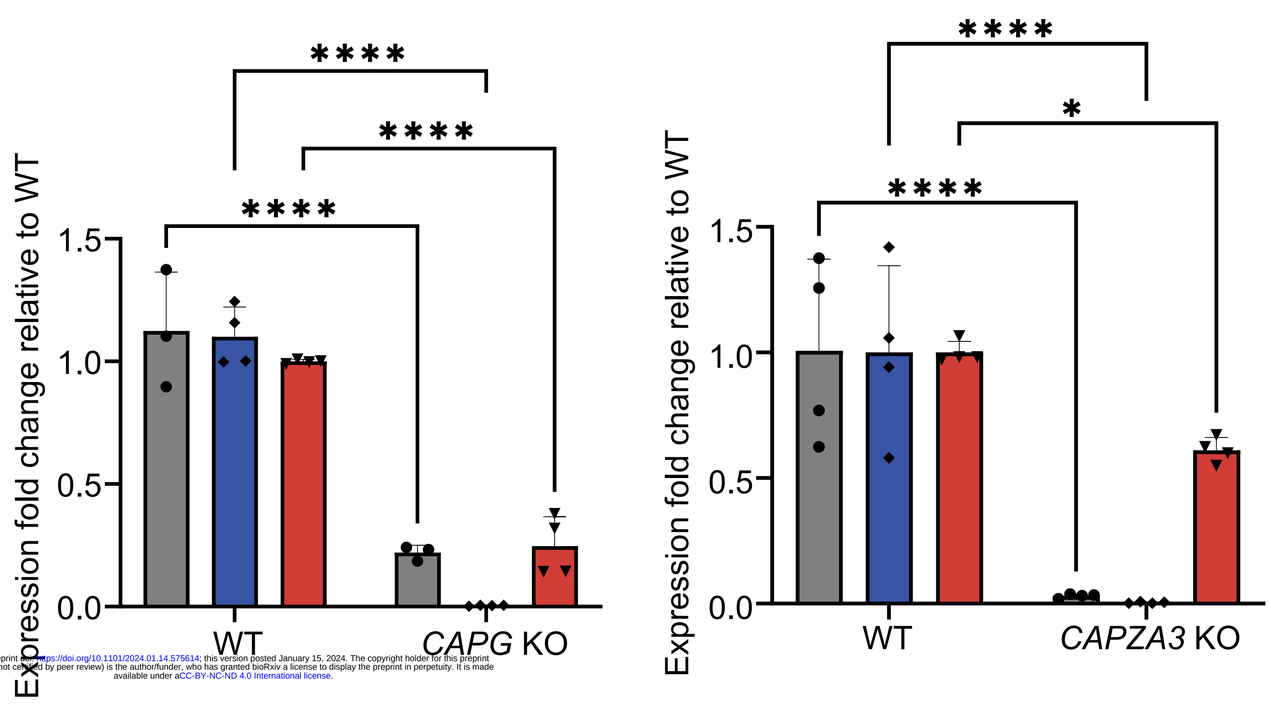

f

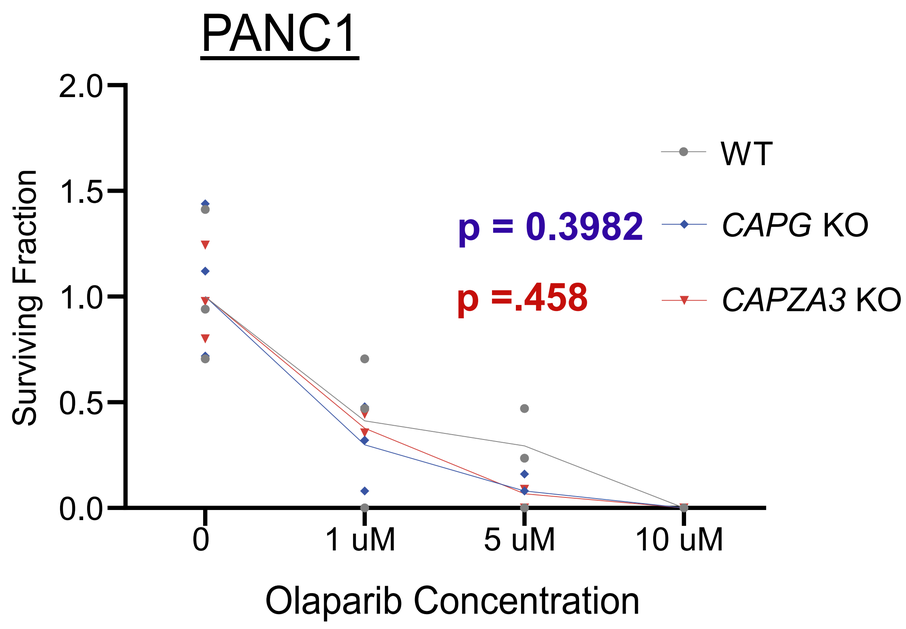

Supplementary Figure 8

a

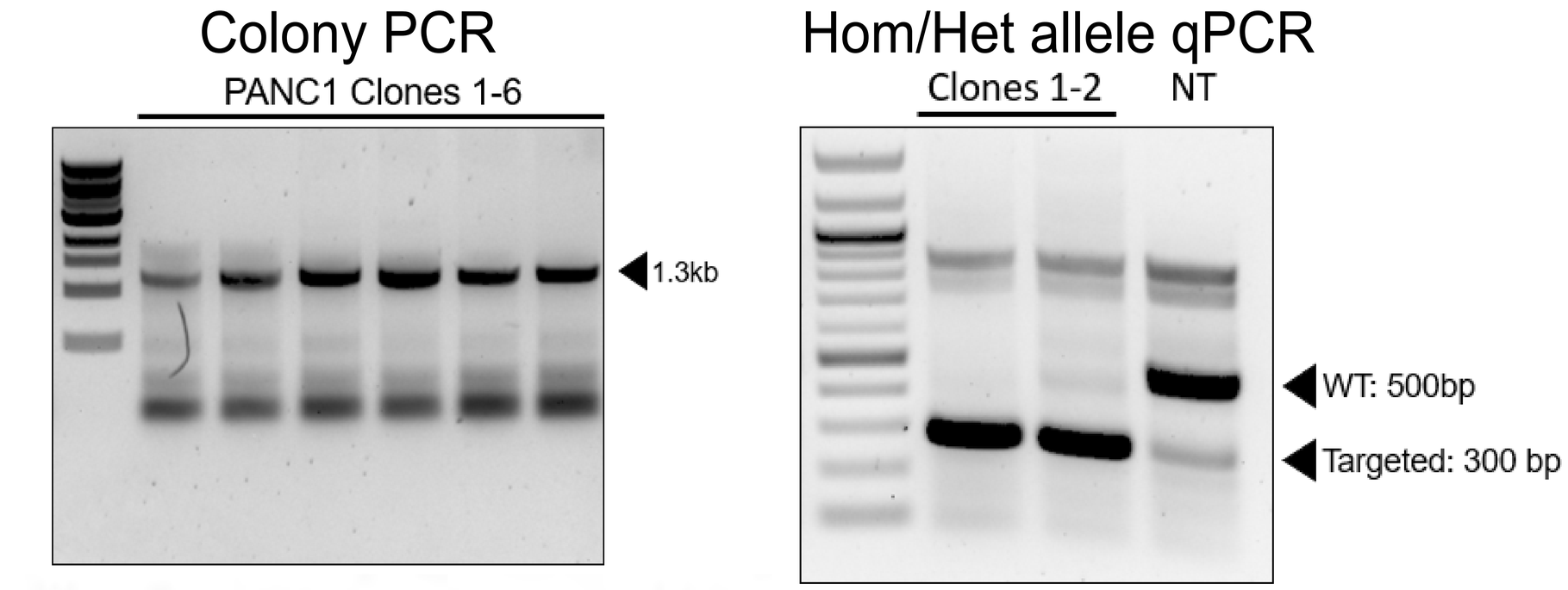

b

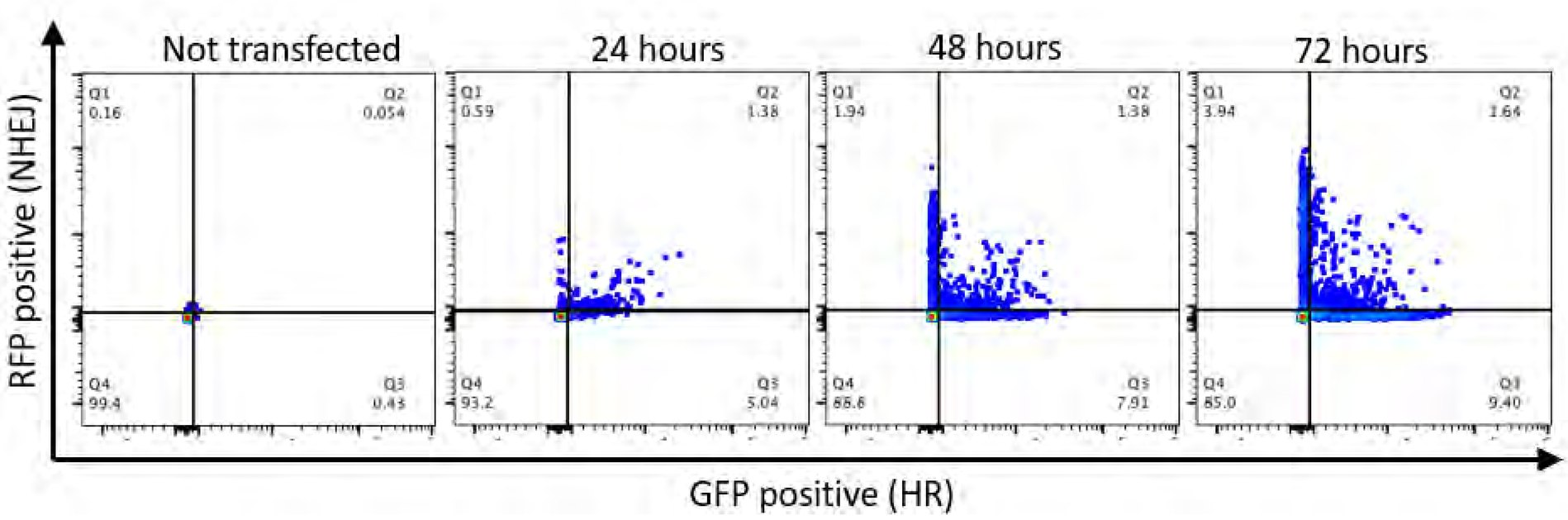

c

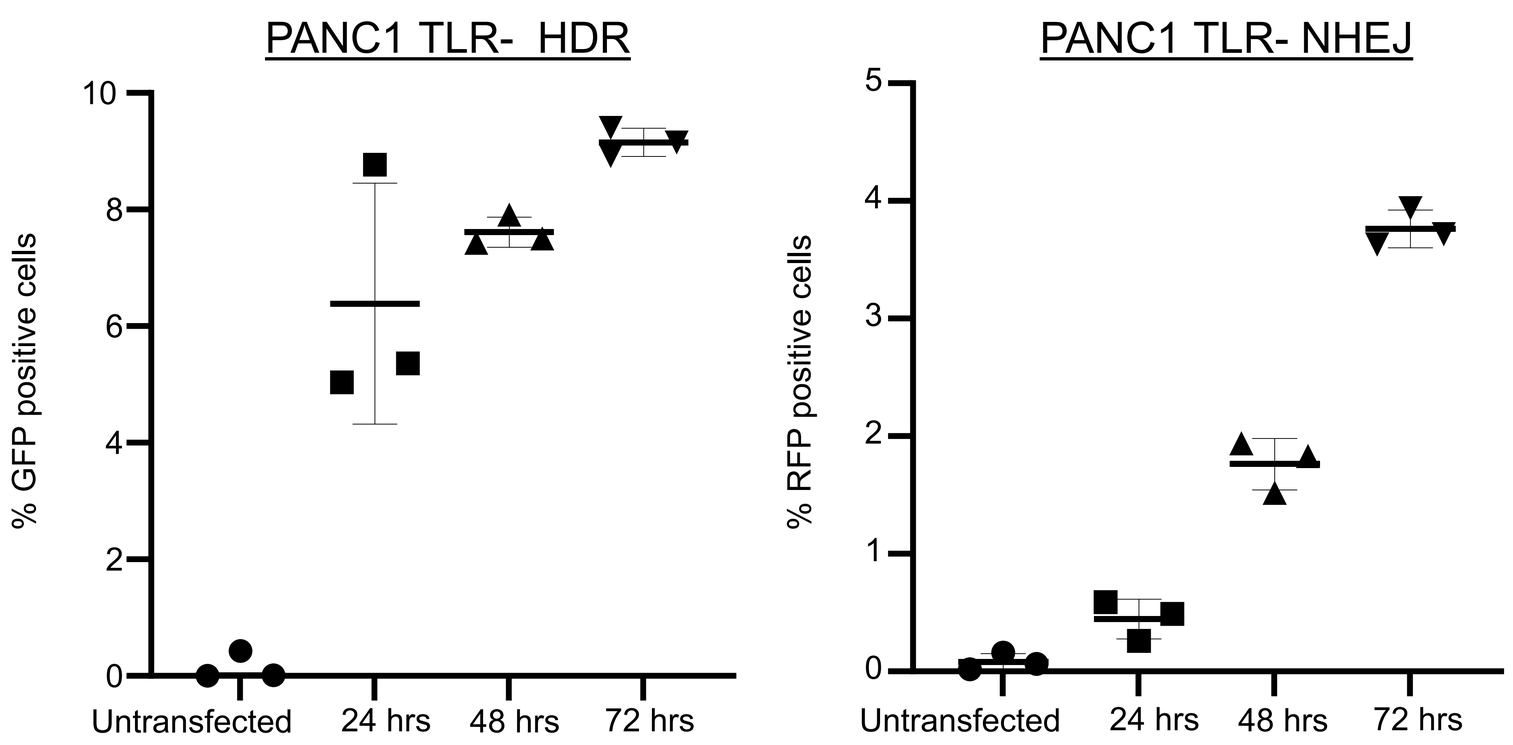

d

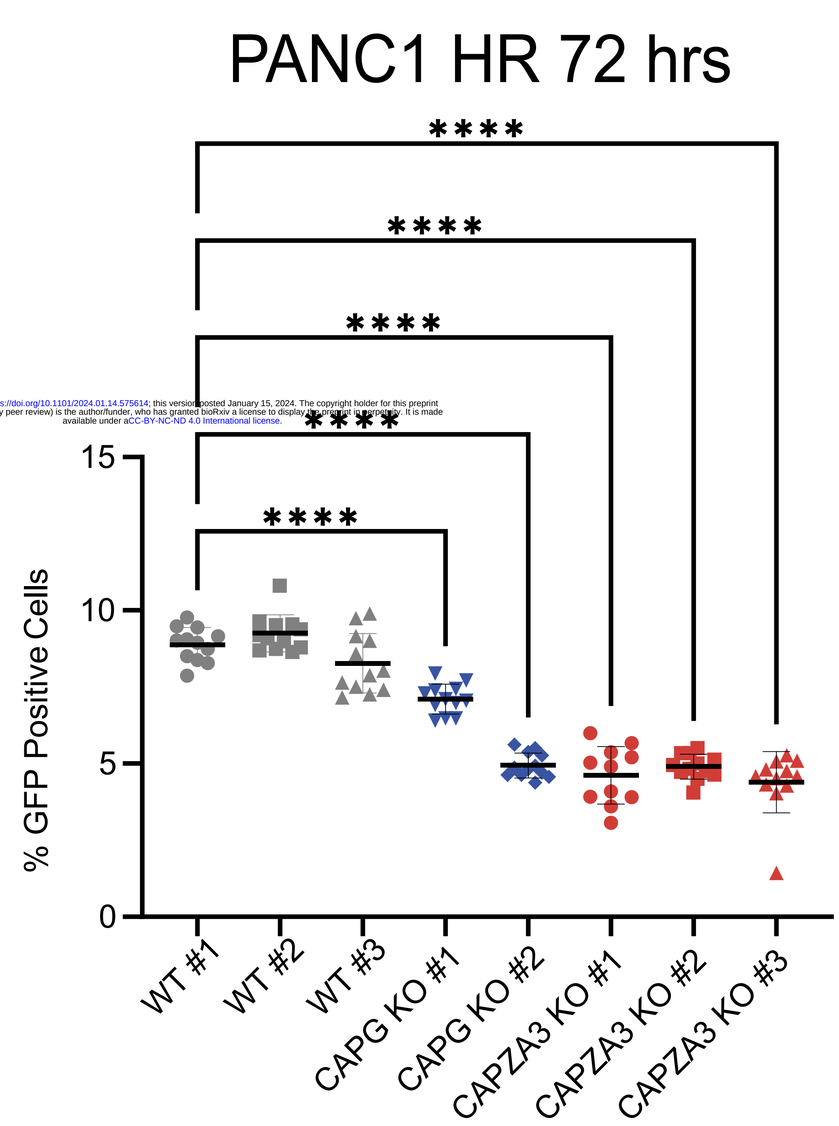

Supplementary Figure 9

a

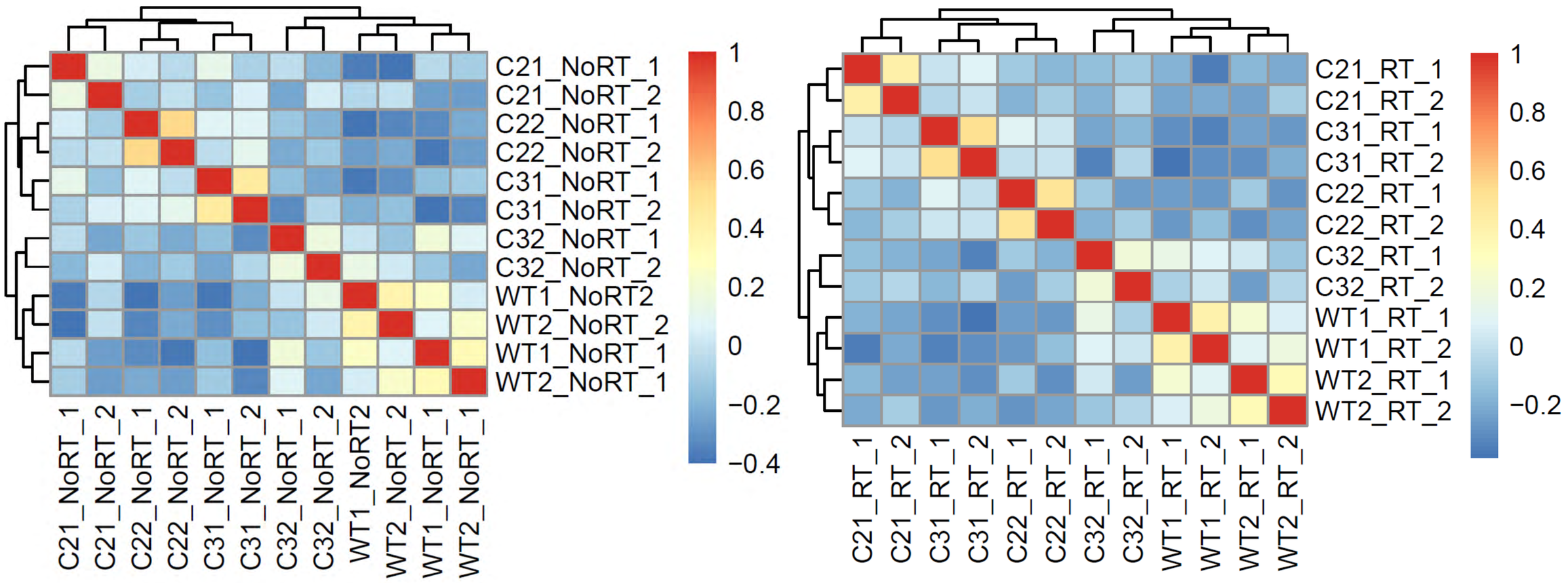

b

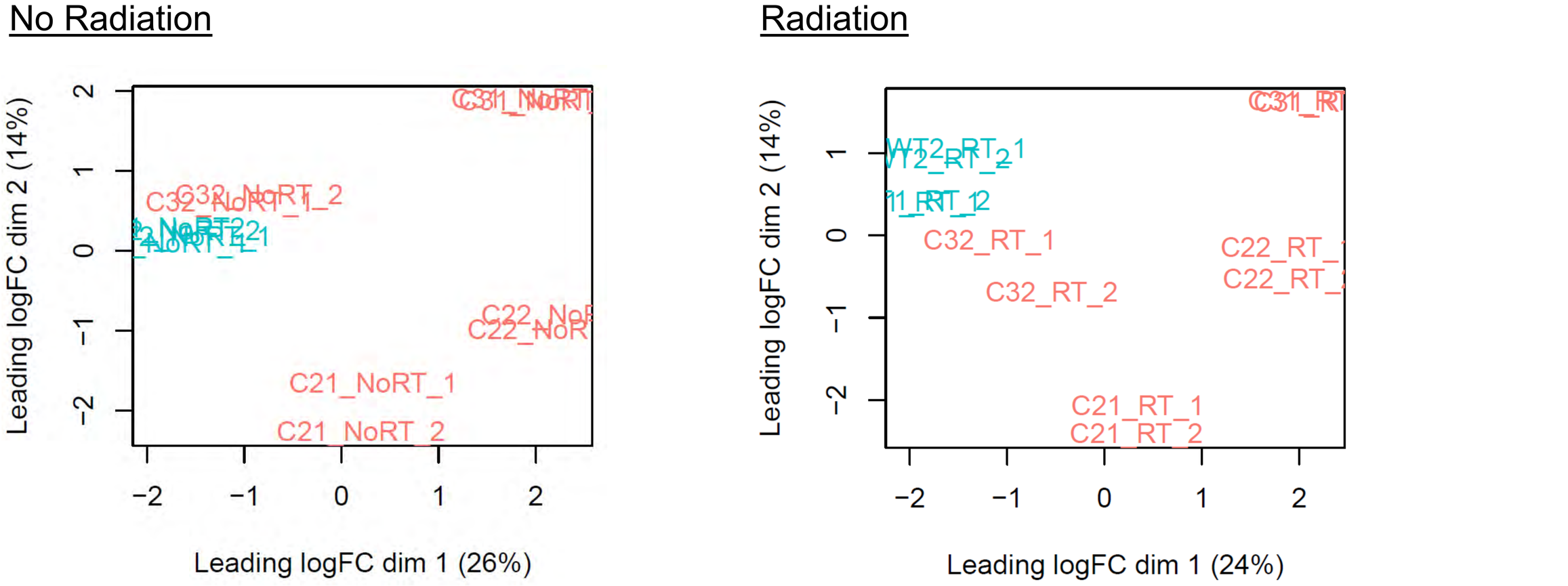

c

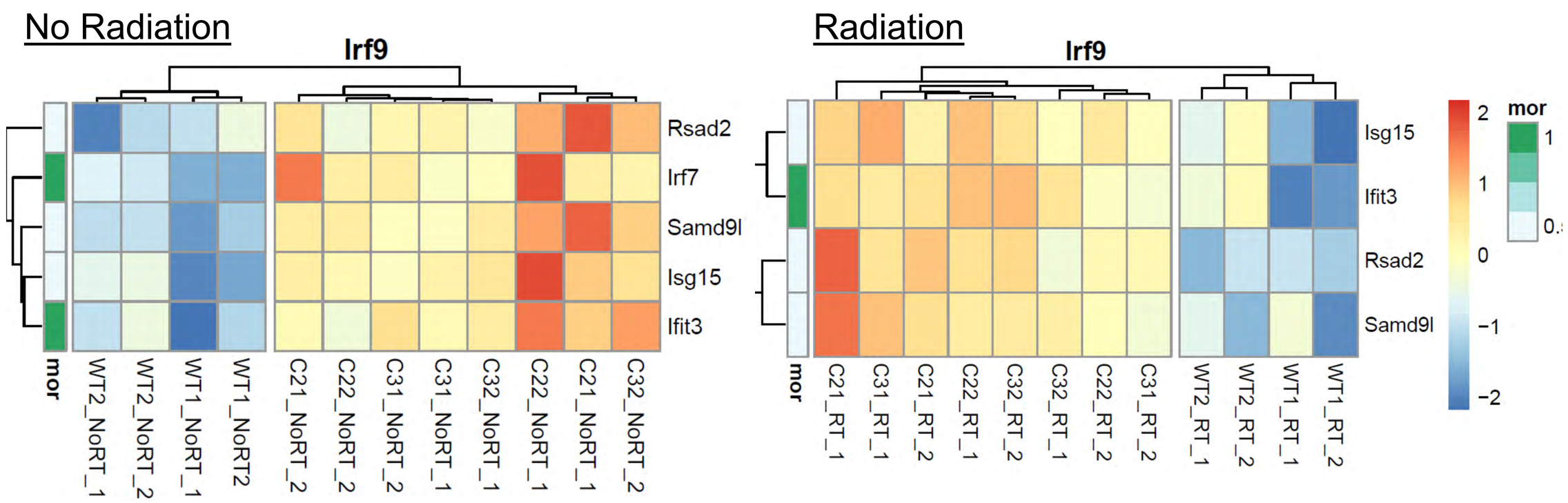

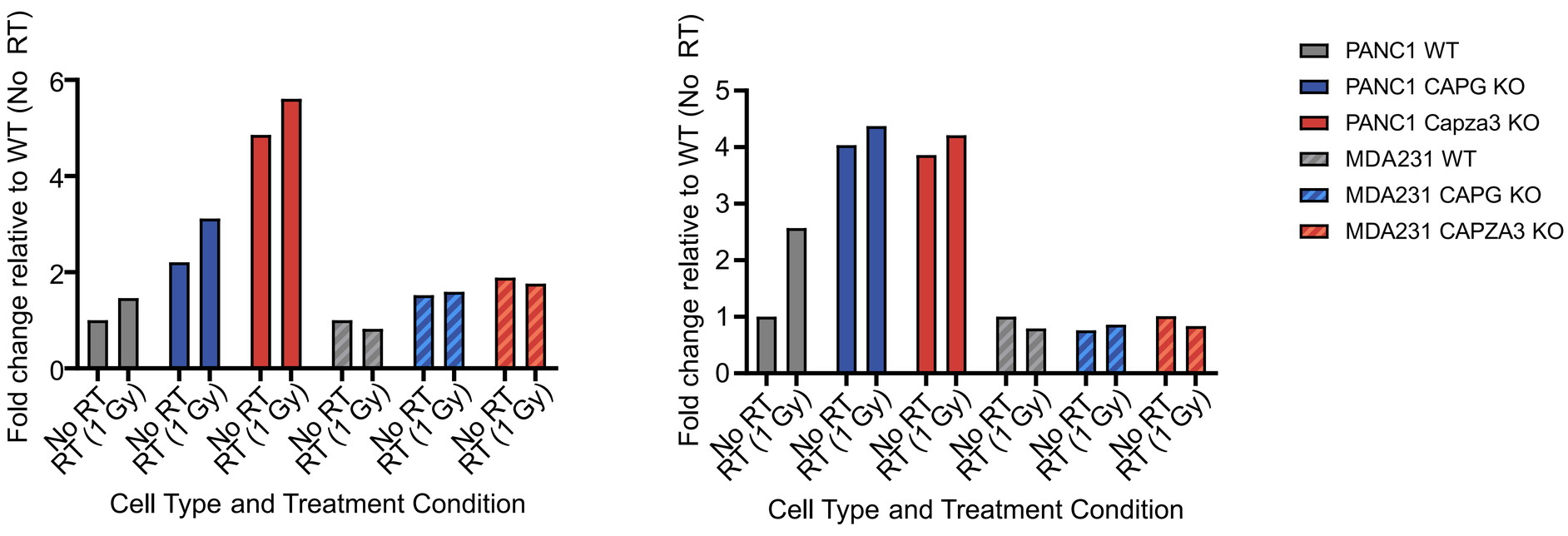

Supplementary Figure 10

a

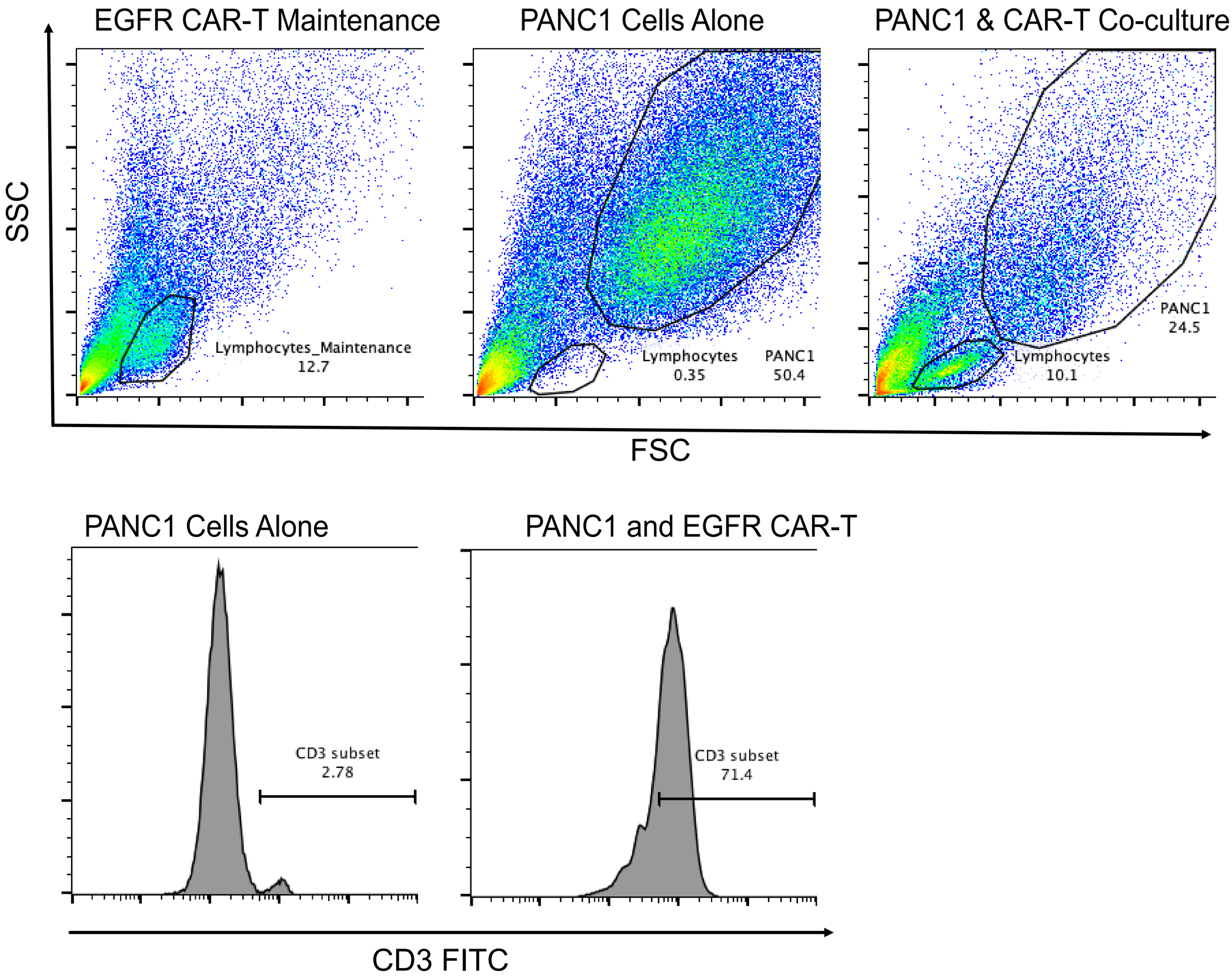

b

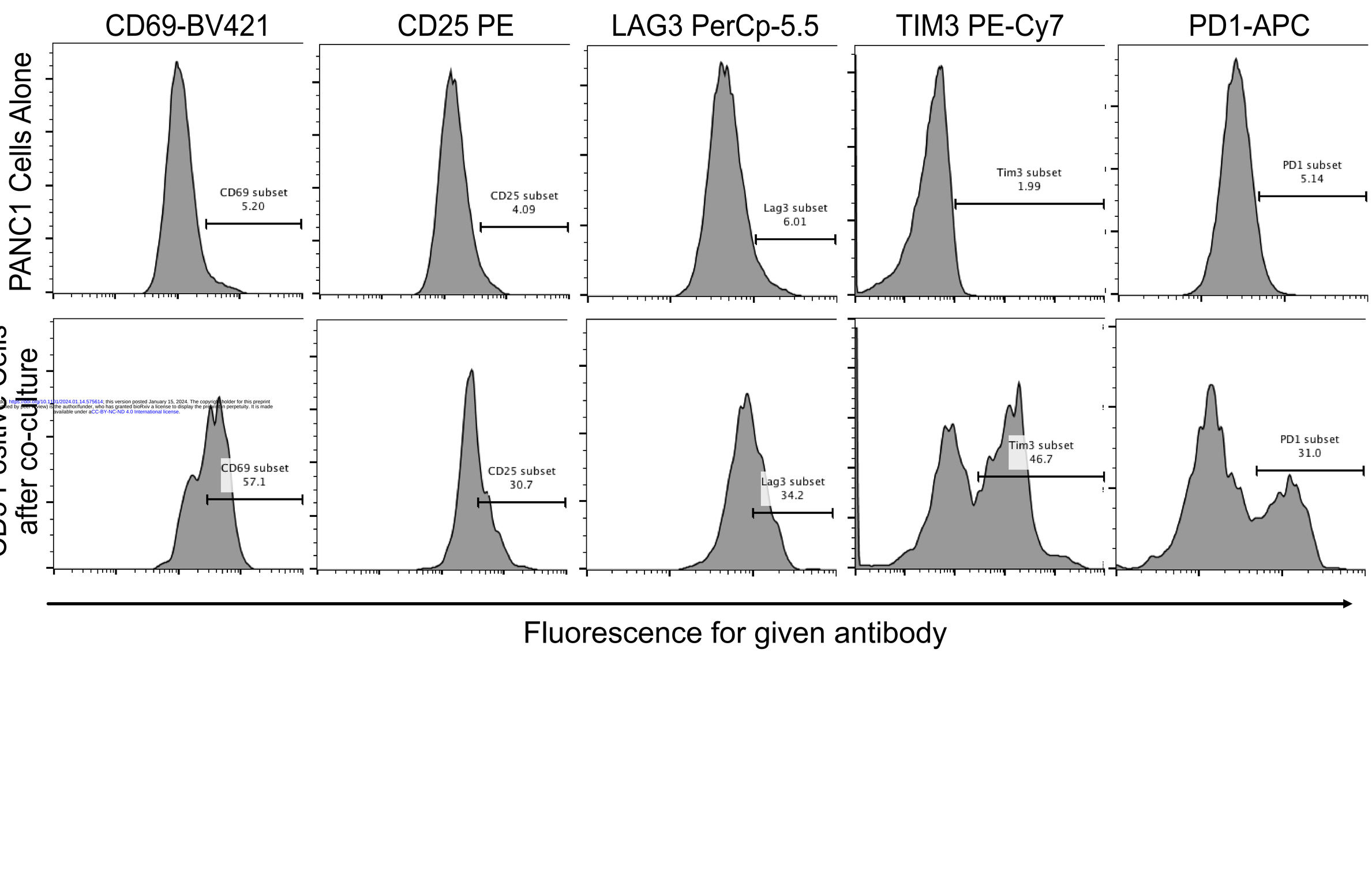

Supplementary Figure 11

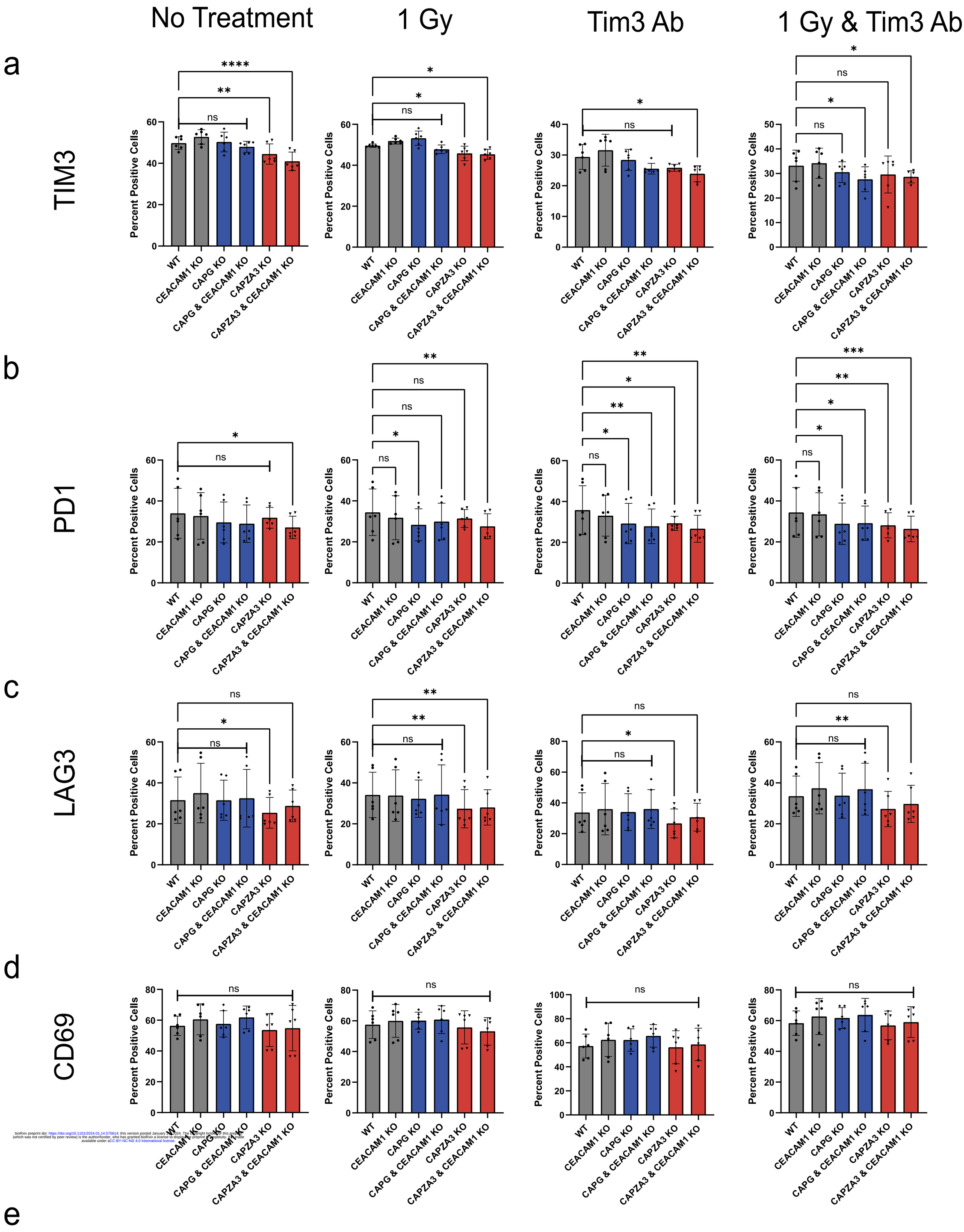

Supplementary Figure 12

a

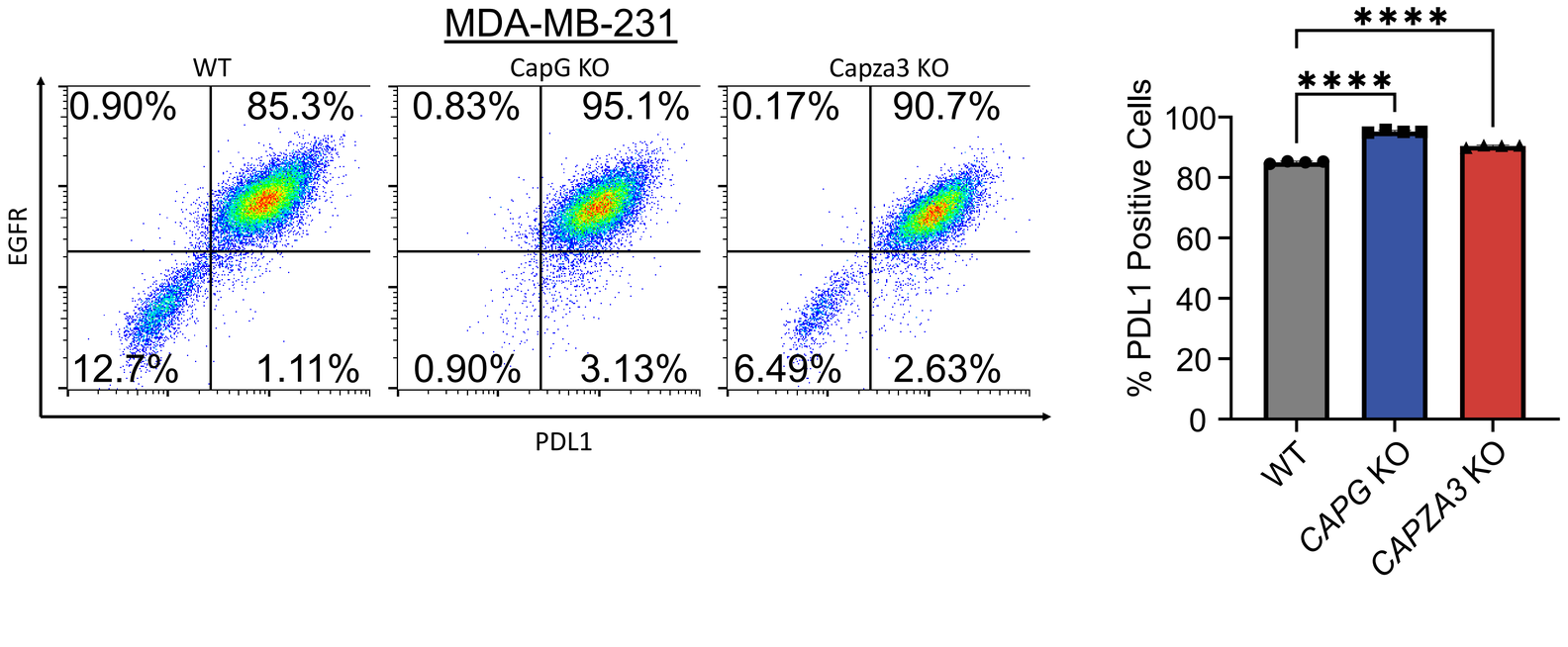

b

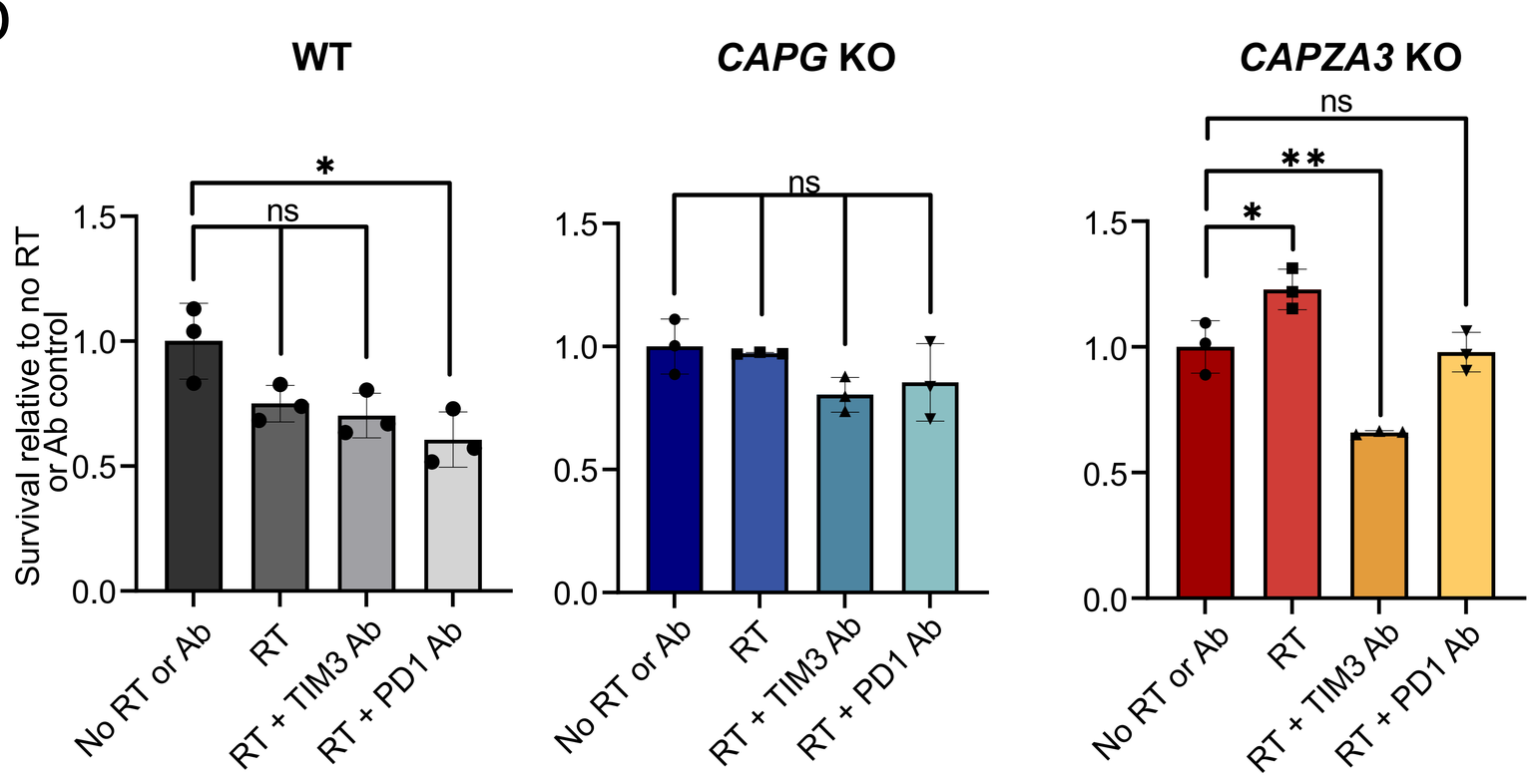

Supplementary Figure 13

a

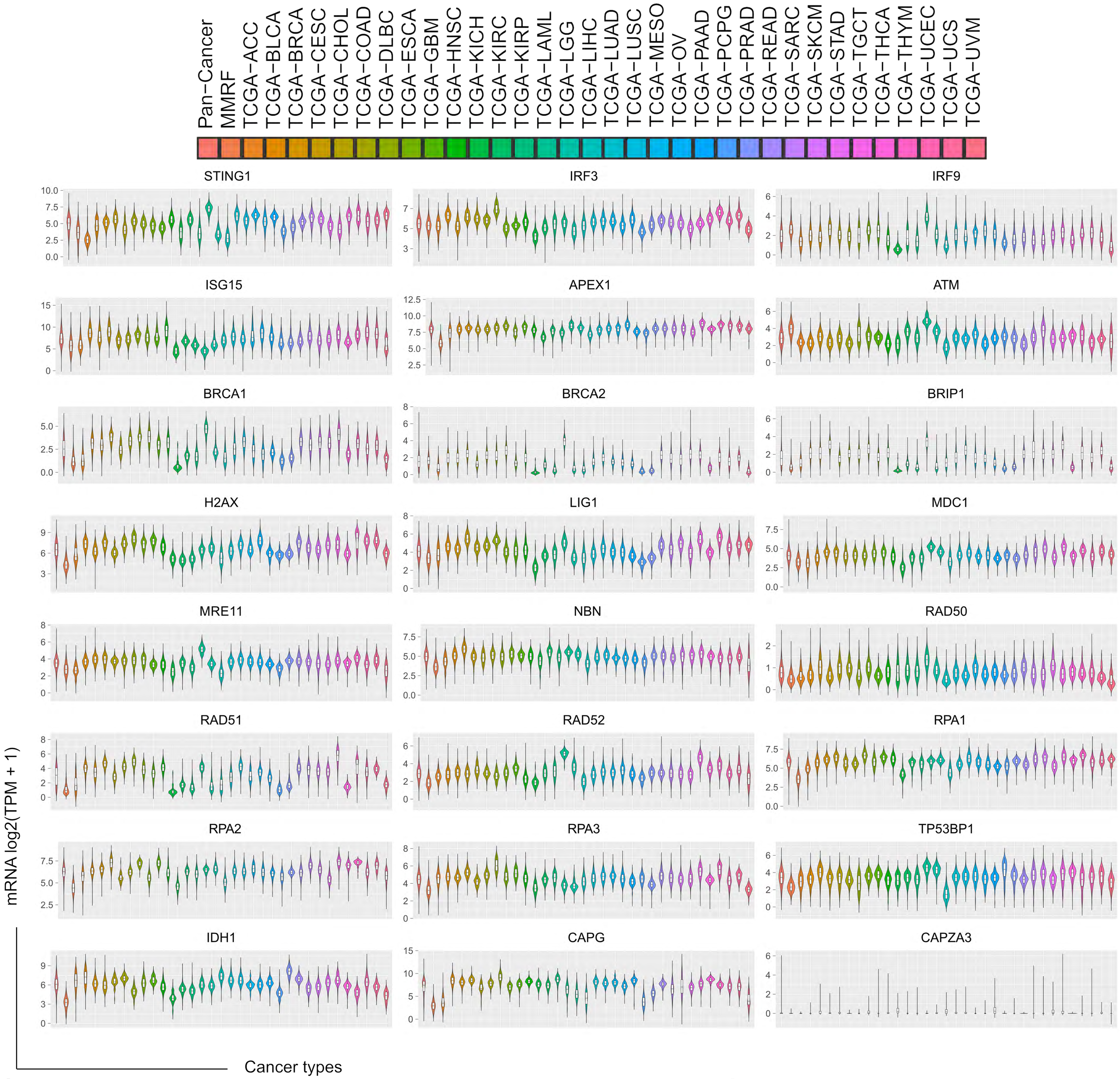

b

c

d

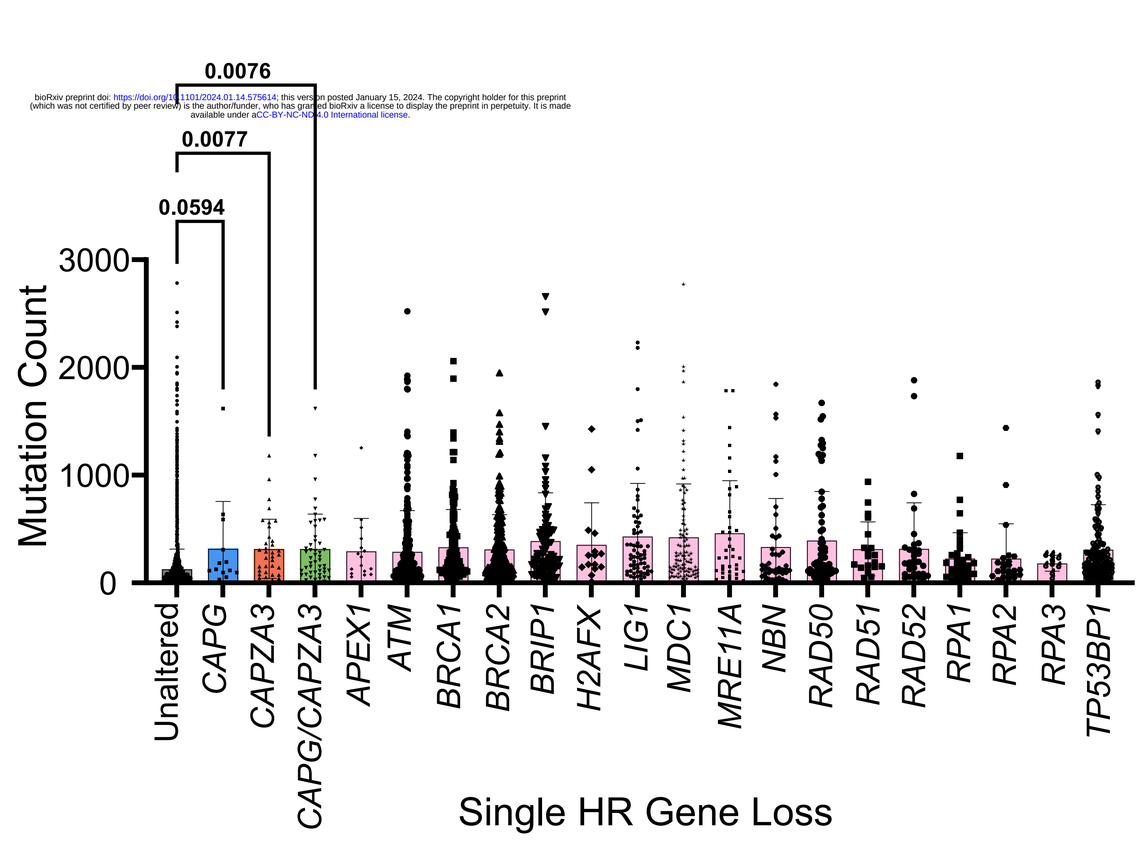

Gene	HR <1	HR >1
APEX1	1	6
BRCA1	2	5
BRCA2	2	8
BRIP1	3	5
CAPG	1	4
CAPZA3	2	4
H2AX	1	4
IDH1	0	4
LIG1	1	3
MDC1	0	6
MRE11	1	8
NBN	1	4
RAD50	1	5
RAD51	2	9
RAD52	0	4
RPA1	2	5
RPA2	2	6
RPA3	2	8
TP53	0	2

Cancer	HR <1	HR >1
MMRF	0	14
ACC	0	12
BLCA	0	1
BRCA	0	3
CESC	0	1
COAD	1	0
ESCA	1	0
GBM	0	1
HNSC	0	1
KICH	0	8
KIRC	5	1
KIRP	1	5
LAML	0	1
LGG	1	5
LIHC	0	11
LUAD	0	5
MESO	0	4

Cancer	HR <1	HR >1
OV	0	2
PAAD	0	7
PCPG	0	1
PRAD	0	1
READ	4	0
SARC	0	6
SKCM	0	4
STAD	1	0
THCA	1	0
THYM	8	1
UCEC	0	1
UVM	0	4

Supplementary Figure 14

a

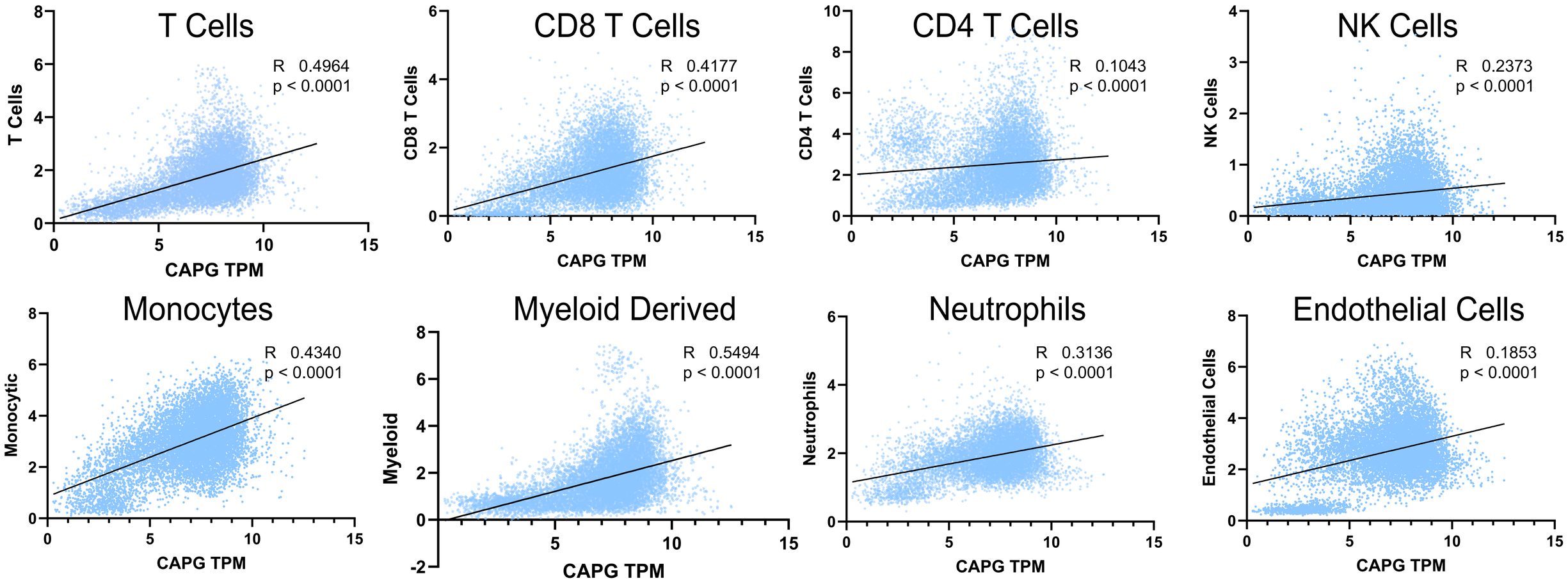

b

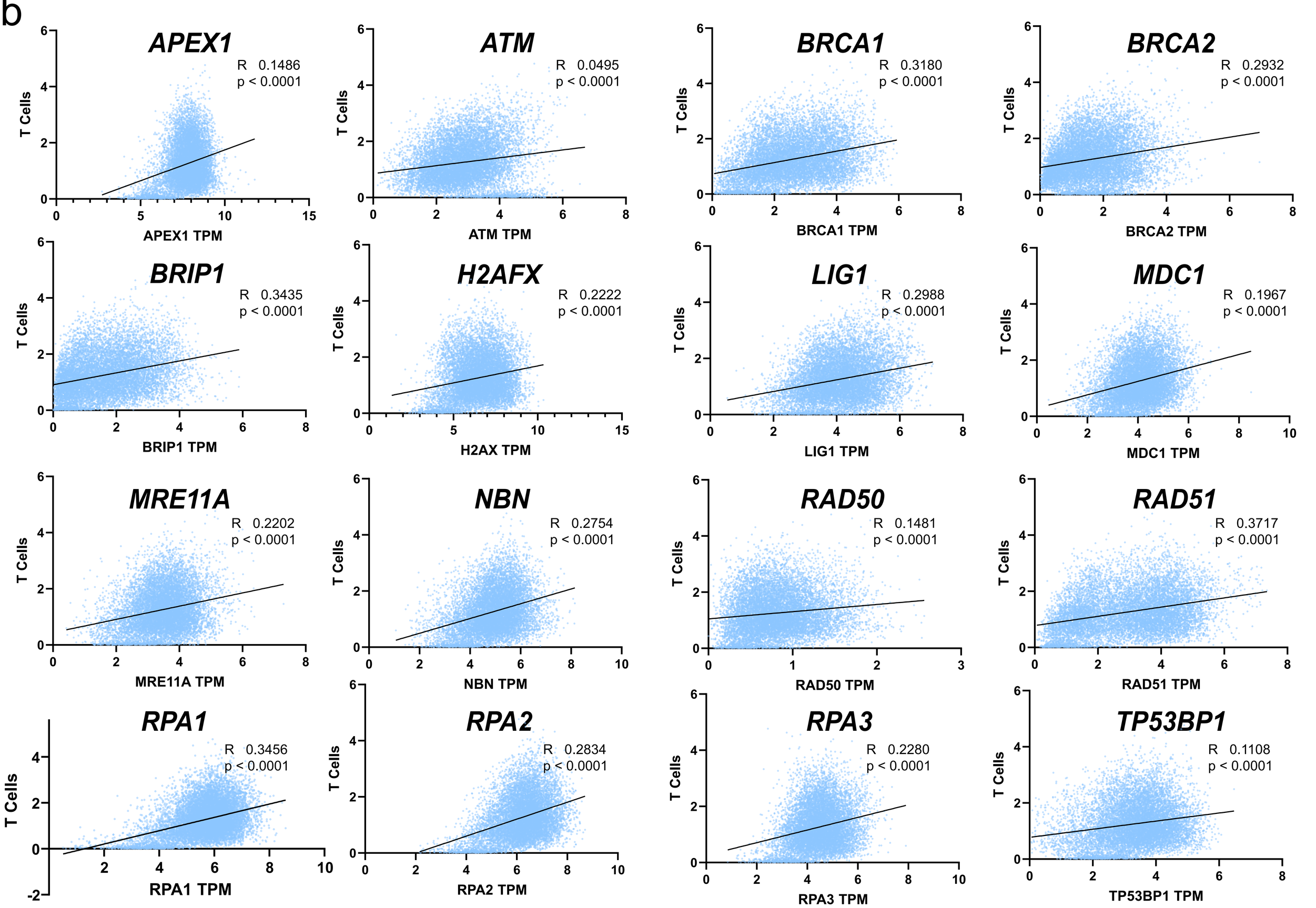

c

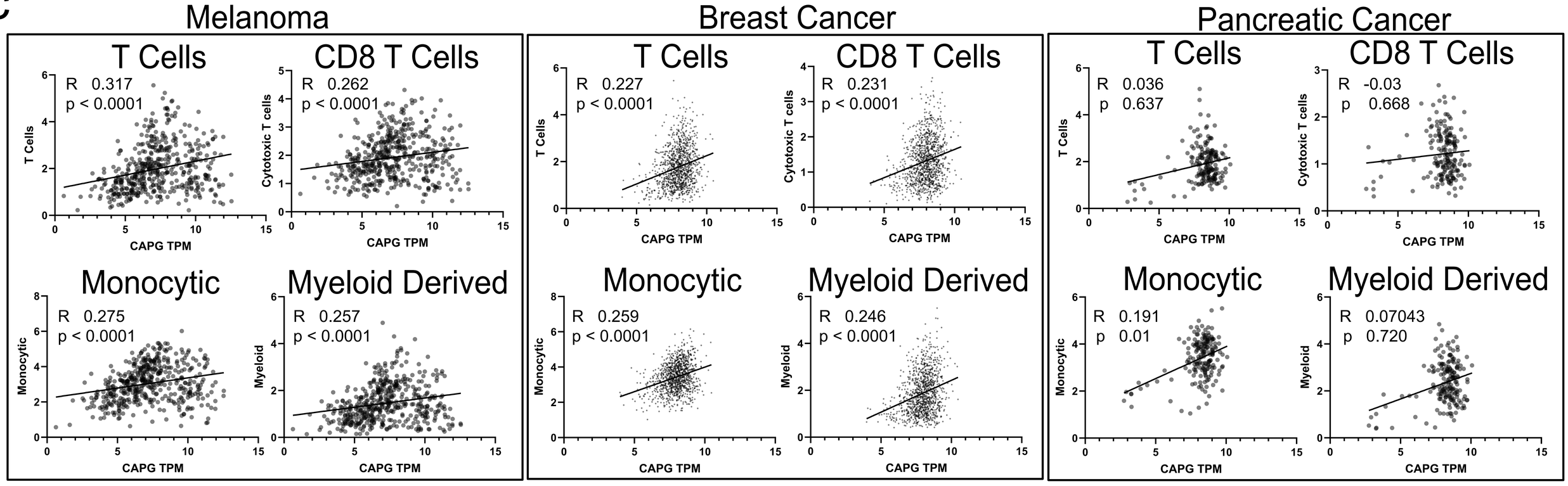

Supplementary Figure 15

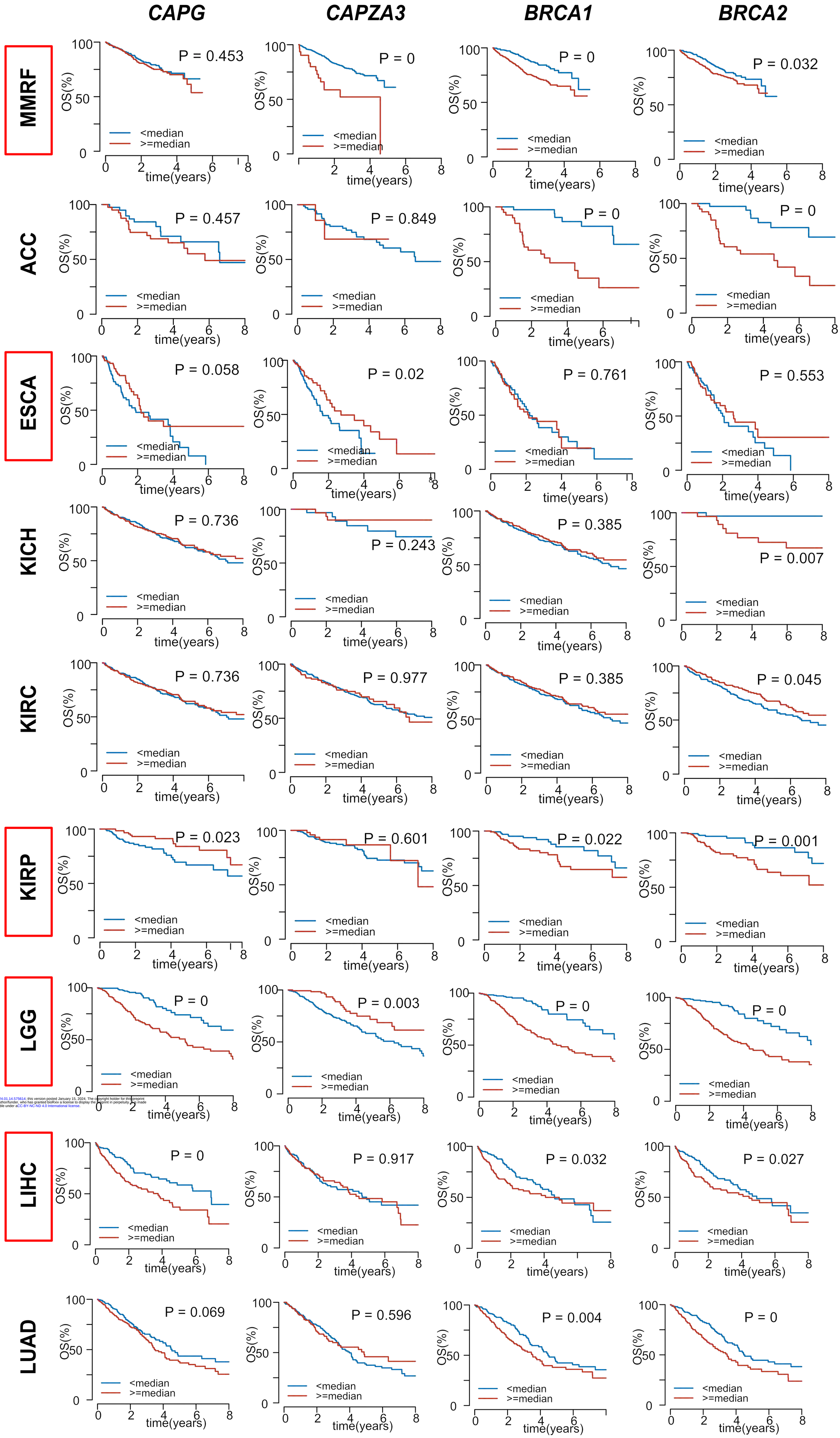

Supplementary Figure 16

a